# RESEARCH ACTIVITIES IN **OPTOELECTRONICS AND ELECTRONICS MANUFACTURING** 2004

PUBLISHER

VTT Electronics, Kaitoväylä 1, P.O.Box 1100, FI-90571 OULU, FINLAND
Tel. +358 20 722 111, Fax +358 20 722 2320
Electronic mail: ele.info@vtt.fi

VTT ELECTRONICS, OULU 2005

# PREFACE

VTT Electronics is one of the six operative units in VTT, the Technical Research Centre of Finland, an independent, multi-field contract research organisation. The main task of VTT Electronics is to work as a strategic R&D partner for electronics industry, thus for its part ensuring the prospected growth in this sector. At VTT Electronics, 70 of its 300 staff members are experts in optics and optoelectronics.

The main goal of Optoelectronics research area is to assist companies in utilizing advanced optical, photonic and optoelectronic technologies in their products. Our core competenceis are in the advanced technologies and integration methods of optoelectronic modules and instruments. This focus includes challenging research and development aims in modelling, simulation and design, new advanced materials, cost-effective fabrication, manufacturing and packaging applied for multi-technological solutions in optics, optical communication, optical measurements as well as sensors and instrumentation.

In this report you will find extended abstracts concerning some of the published research work carried out in 2004. The abstracts of the examination theses completed by our personnel and a list of publications are also included.

Oulu, April 6, 2005

Further information: www.vtt.fi/ele

Jouni Tornberg
Head of Optoelectronics research
*Jouni.Tornberg@vtt.fi*

Harri Kopola
Research professor
*Harri.Kopola@vtt.fi*

# TABLE OF CONTENTS

# Extended Scattered Field Technique for the FDTD Method


## ABSTRACT

An extension for the scattered field technique is proposed, which enables FDTD modelling of the scattering of single frequency light from objects having infinite lateral extent. The presented technique is directly applicable to the Lorentz or Debye medium.


## 1. INTRODUCTION

The Finite Difference Time Domain (FDTD) method is widely employed in solving electromagnetic scattering problems, where a spatially finite scatterer is illuminated by a single frequency plane wave. A plane wave having infinite lateral extent is generally excited in the FDTD method either by the total field scattered field (TF/SF) technique [1] or by the scattered field (SF) technique [2]. In the absence of a scatterer, both of these techniques produce a field that is called the incident field. In the presence of a scatterer, these techniques produce a field that is different than the incident field, called the total field. The difference between total field and incident field is referred to as the scattered field. The TF/SF technique divides the FDTD computation domain into a total field region and a scattered field region, which are separated by a virtual interface that is transparent for incoming waves. This virtual interface generates the incident field in the FDTD mesh and guides the incident field through the mesh. In the scattered field technique, the total field is expressed as a sum of incident and scattered field, and then Maxwell's equations are reformulated in such a manner that only scattered field components are solved by the FDTD method. Since the incident field is initially known, the total field is a superposition of the incident and the scattered field components.

The TF/SF and SF techniques are capable of modelling spatially finite scatterers residing in a homogeneous background medium, while they fail to model structures with infinite lateral extent. For example, neither of these techniques can be used to model light transmission through an aperture in a laterally infinite metal film. In 2002, Anantha et al. introduced a generalised TF/SF technique [3] (G-TF/SF), which can model infinite scatterers illuminated by arbitrarily-oriented plane waves. However, the G-TF/SF technique is rather complicated, and it requires preliminary calibration runs. The objective of this paper is to introduce a numerically simpler technique originating from the SF technique to excite a plane wave in electromagnetic problems including scatterers having infinite lateral extent.

## 2. EXTENDED SCATTERED FIELD TECHNIQUE

This section introduces the extended scattered field technique in detail. Our starting point is Maxwell's equations for a linear, non-magnetic ($\mu = \mu_0$) isotropic medium:

$$\nabla \times \mathbf{E} = -\mu_0 \frac{\partial \mathbf{H}}{\partial t}, \tag{2.1}$$

$$\nabla \times \mathbf{H} = \varepsilon \frac{\partial \mathbf{E}}{\partial t} + \sigma \mathbf{E}, \tag{2.2}$$

where E is the electric field intensity (V/m), H is the magnetic field intensity (A/m), $\mu_0$ is the permeability of free space, $\varepsilon$ is the dielectric permittivity, and $\sigma$ is the electric conductivity. Due to the linearity of Maxwell's equations, the total field quantities can be expressed as a sum of the incident and the scattered fields, i.e.

$$\mathbf{E} = \mathbf{E}^i + \mathbf{E}^s \tag{2.3}$$

$$\mathbf{H} = \mathbf{H}^i + \mathbf{H}^s \tag{2.4}$$

It is assumed that the incident field is Maxwellian obeying the following equations:

$$\nabla \times \mathbf{E}^i = -\mu_0 \frac{\partial \mathbf{H}^i}{\partial t} \tag{2.5}$$

$$\nabla \times \mathbf{H}^i = \varepsilon_i \frac{\partial \mathbf{E}^i}{\partial t} + \sigma_i \mathbf{E}^i, \tag{2.6}$$

where $\varepsilon_i$ and $\sigma_i$ and are the local permittivity and the electric conductivity of the structure for which the incident field is known. Substituting Eqs. (2.3)-(2.4) with Maxwell's equations (2.1)-(2.2), using (2.5)-(2.6), and rearranging terms, one obtains:

$$\nabla \times \mathbf{E}^s = -\mu_0 \frac{\partial \mathbf{H}^s}{\partial t} + \underbrace{\left(-\mu_0 \frac{\partial \mathbf{H}^i}{\partial t} - \nabla \times \mathbf{E}^i\right)}_{=0}, \tag{2.7}$$

$$\nabla \times \mathbf{H}^s = \varepsilon \frac{\partial \mathbf{E}^s}{\partial t} + \sigma \mathbf{E}^s + \mathbf{S}, \tag{2.8}$$

with:

$$\mathbf{S} = (\varepsilon - \varepsilon_i) \frac{\partial \mathbf{E}i}{\partial t} + (\sigma - \sigma_i)\mathbf{E}^i, \tag{2.9}$$

Traditional FDTD kernels [1] can directly be used to solve discretised versions of Eqs. (2.7)-(2.8), with the difference that only the scattered field components are solved instead of the total field components. Note that the source term S, which is the only quantity that depends on incident field $\mathbf{E}^i$, is non-zero only in regions where the material properties of the FDTD mesh ($\varepsilon$, $\sigma$) differ from the ($\varepsilon^i$, $\sigma^i$) structure.

The ESF technique differs from the traditional SF technique only in the incident structure. The SF technique employs a homogeneous medium for the incident structure. In the ESF technique, the incident structure is not

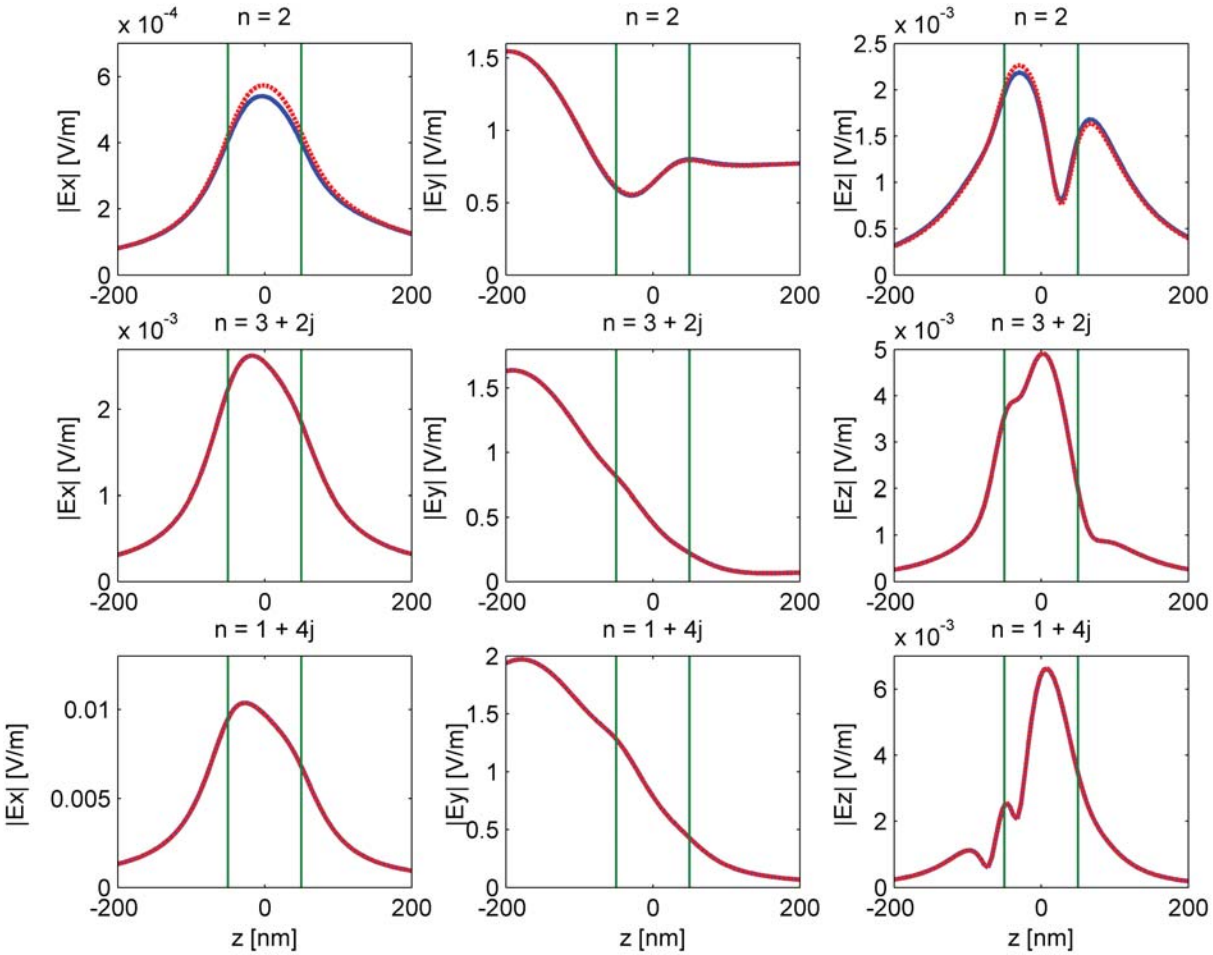


*Figure 1: Comparison between the ESF (red dashed line) and the TF/SF technique (blue solid line) in the transmission of a normally incident y-polarised plane wave through a 100 nm wide square aperture in a thin film having the refractive index of n. The film resides in the xy plane and the incident plane wave propagates in the z direction. The top row: n = 2, the middle row: n = 3 + 2j, and the bottom row: n = 1 + 4j. Electric field amplitudes for x, y, and z components are shown along the z axis through the central point of the aperture. The vertical solid green lines illustrate the boundaries of the thin film in the z direction.*

homogeneous. Instead, it is a structure in which interaction with the originally incident light can be solved analytically. The analytical solution is then used as an incident field for the scattered field technique. With this approach, the excitation area is limited to a finite region apart from the absorbing boundaries. If the excitation region was directly in contact with the absorbing boundaries, it would cause unphysical diffraction effects that lead to a significantly erroneous solution. To illustrate this ideology further, consider a multi-layer structure including an aperture in one of its layers. Assume that this multi-layer structure is illuminated by a plane wave having arbitrary incident angle and polarisation. When the ESF technique is applied to the problem, first the interaction of the single frequency plane wave and the multi-layer structure is solved without the aperture. Next, the solution is used in the FDTD simulation as the incident field term in Eq. (2.9). Finally, the total field solution is obtained as a sum of the incident and the scattered field solutions.

Equations (2.7)-(2.8) are used with the FDTD method only when $\varepsilon$ and $\sigma$ define a medium for which the real part of the refractive index is larger than the imaginary part. If the imaginary part of the refractive index is larger than the real part, as is the case with certain metals at optical frequencies, the medium must be modelled using an appropriate phenomenological relationship between the electric field and the polarisation. It has been noted that the single pole Lorentz dispersion relation is adequate for the modelling of such materials [4]. However, refractive indexes of the incident structure ($\varepsilon_i$, $\sigma_i$) are not limited in the ESF technique. For example, if the geometry is a dielectric ap-

erture in a silver film for which $n_{Ag} = n_{re} + jn_{im}$, where $n_{re} < n_{im}$, Eqs. (2.7)-(2.9) are valid in the aperture region, only the silver film must be treated with the Lorentz dispersion model.

### 3. VALIDITY OF THE ESF TECHNIQUE

In this section, the validity of the ESF technique is verified by comparing the ESF and the TF/SF techniques in the transmission of normally incident plane waves through an aperture in a thin film. It is assumed that the plane wave propagates in the *z* direction, and the thin film is invariant in the *x* and *y* directions. The TF/SF technique is modified in such a manner that it enables the modelling of this problem. Since the background structure, where the aperture resides, is invariant in the *x* and *y* directions, propagation of normally incident plane waves through the multilayer structure without the aperture are modelled using a one-dimensional FDTD simulation. This one-dimensional simulation, which is run simultaneously with the actual three-dimensional FDTD simulation, is then used as a look-up table to obtain the incident field for the TF/SF technique. The use of look-up tables with the TF/SF technique is described in detail in Ref. [1].

The modelled structure is a 100 nm wide square aperture in a 100 nm thick thin film with refractive index of *n*. The aperture is illuminated by a $E_y$-polarised, normally incident plane wave having free space wavelength of 650 nm and unit amplitude. The FDTD mesh is comprised of 5 nm x 5 nm x 5 nm Yee cells. To verify that the ESF technique works properly with all material types, three cases were investigated, where the free standing thin film was made of a dielectric($n = 2 + 0j$), a lossy ($n = 3 + 2j$), and a metallic ($n = 1 + 4j$) medium. Figure 1 shows the electric field amplitudes of *x, y, z* components along the *z* axis through the central point of the aperture for the ESF and the TF/SF techniques in all three cases. It is seen that the results are in agreement with each other. Small differences in the results between the techniques were observed in $E_x$ and $E_y$ components when the refractive index of the slit is 2.0. In other cases, the differences are imperceptible. The differences are due to the fact that it is almost impossible to determine the exact thickness of the thin film seen by the FDTD method. Therefore, the thickness of the thin film used in the analytical solution differs slightly from the thickness seen by the FDTD method.

### 4. DISCUSSION AND CONCLUSION

A novel method originating from the SF technique to propagate plane waves at oblique incidence through apertures in thin films having infinite lateral extent has been introduced. The introduced technique is verified by comparing the ESF and TF/SF techniques in the transmission of normally incident plane waves through a square aperture in a thin film. Excellent agreement between techniques is observed. The method can be used, e.g., for the analysis of light transmission through sub-wavelength apertures [5].

### REFERENCES


1. A. Taflove and S. C Hagness, “Computational Electrodynamics: The Finite-Difference Time Domain Method”, Artech House, Boston, 2000.
2. K. S. Kunz and R. J. Luebbers, “The Finite Difference Time Domain Method for Electromagnetics”, CRC Press, London, 1993.
3. V. Anantha and A. Taflove, “Efficient Modeling of Infinite Scatterers Using a Generalized Total-Field/Scattered-Field FDTD Boundary Partially Embedded Within PML”, IEEE Transactions on Antennas and Propagation, Vol. 50, pp. 1337 - 1349, 2002.
4. J. B. Judkins, C. W. Haggans and W. R. Ziolkowski, “Two-dimensional finite-difference time-domain simulation for rewritable optical disk surface design”, Applied Optics, Vol. 35, pp. 2477 - 2487, 1996.
5. J. T. Olkkonen, K. J. Kataja, J. Aikio, D. G. Howe and T. D. Milster, “Analysis of sub-wavelength apertures via the extended FDTD SF technique”, Proc. SPIE Vol. 5380, p. 653-662, 2004.



Juuso Olkkonen
*Juuso.Olkkonen@vtt.fi*



Kari Kataja
*Kari.Kataja@vtt.fi*



Janne Aikio
*Janne.Aikio@vtt.fi*

Dennis G. Howe and Tom D. Milster
*University of Arizona, Optical Sciences Center, Tucson, AZ 85721-0094, U.S.A*

# Readout Signal Simulation as a Function of Readout Power for Super Resolution Optical Disk

Particle effects to the readout signal in the in the bubble-pit configuration is studied using the 2D FDTD method as a function of the readout power.

## 1.INTRODUCTION

The Super Resolution (SR) technique[1,2] has been extensively studied in order to increase the data density of the optical disk. In the SR disk, an optically nonlinear material layer is deposited at the top of the data layer. This SR layer improves the quality of the readout signal from the data marks smaller than the resolution limit (RL) of the conventional optical pickup unit (OPU). In the recent experimental work with SR layers made of $AgO_x$ or $PtO_x$, it has been observed that the SR layer is permanently damaged in the writing process and the phase change data layer is found to be in a fully crystalline phase[3,4]. The data marks are formed via the deformation of the thin film layer structure. Oxygen bubbles form in the metal oxide layer and metallic particle aggregates are located inside these bubbles.

In the readout process, the signal-to-noise (SNR) ratio is nonlinearly related to the readout power (see e.g. ref. 5). However, the mechanism responsible for this behaviour is not clear. The localised surface plasmons have been thought to be the dominating mechanism[6]. The heating of the data layer has also been suggested to be the main mechanism[7]. This explanation is supported by research where no metallic particles exist in the bubble pits of the SR layer[8]. In this paper, we describe how the drift of the metallic particles can be responsible for the nonlinear behaviour of the SNR as a function of the readout power. It has been shown in several papers[9-11] that the Ag aggregates form a doughnut-shaped aperture centred on the focused laser spot. In our model we assume, similarly, that the Ag aggregates drift away from the center of the readout beam when the readout power (optical field intensity) inside the SR layer is high enough. The bubble pits give boundaries to the motion of the particles and therefore a doughnut-shaped aperture is formed only at a mark on the optical axis of the readout beam. In all of the other marks that are within the region affected by the readout beam, the Ag aggregates are located in the far edge of the bubble from the optical axis of the beam (crescent shaped structure). The area where the readout laser beam affects the Ag aggregates is inside the 'aperture radius' of the laser beam and, as a first approximation, we assume that this radius is linearly related to the readout power.

## 2. MODEL

We used a combination of the Finite Difference Time Domain (FDTD)[12] method and the Plane Wave Spectrum (PWS)[13] method to simulate the readout signal, i.e. the modulation of the reflected optical power from the SR disk structure. The readout performance of an optical disk was modelled by first calculating the reflected EM fields with the FDTD method in on-mark and off-mark situations, which are assumed to correspond with the minimum and maximum detected optical powers. The electric field components in the far field were computed with the PWS method. The far field intensity was obtained by summing these components in quadrature. The total optical power (I) received by the detector was calculated by integrating the far field intensity over the numerical ap-

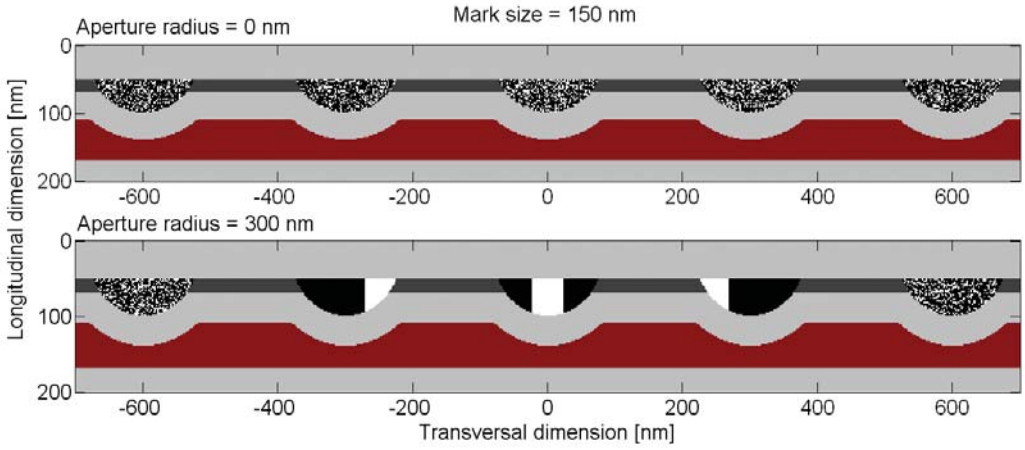


*Figure 1. Simulation geometry in the on-mark situation when the mark size is 150 nm and the aperture radius is 0 nm in upper image and 300 nm in the lower image. The layer structure is from top to bottom ZnS-$SiO_2$/$AgO_x$/ZnS-$SiO_2$/GST/ZnS-$SiO_2$. Layer thicknesses are 18, 40 and 60 nm for $AgO_x$, (Spacer) ZnS-$SiO_2$ and GST layers respectively. The Ag concentration in the bubbles is 70%.*

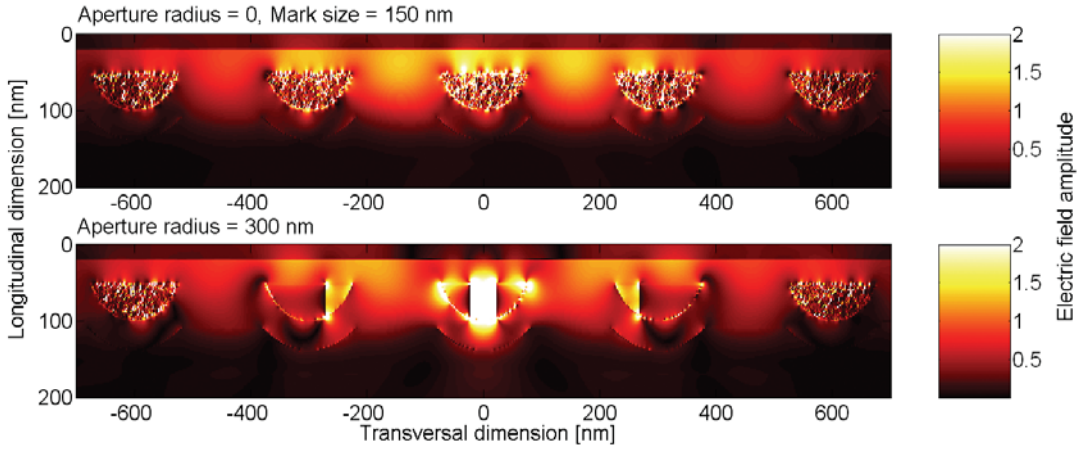


*Figure 2. The electric field amplitude in the on-mark situation when the mark size is 150 nm and the aperture radius is 0 nm in upper image and 300 nm in the lower image. The layer structure is from top to bottom ZnS-SiO2/AgOx/ZnS-SiO2/GST/ZnS-SiO2. Layer thicknesses are 18, 40 and 60 nm for AgOx, (Spacer) ZnS-SiO2 and GST layers respectively. The Ag concentration in the bubbles is 70%.*

erture (NA) of the objective lens of the OPU. The modulation of the reflected optical power is obtained from the equation $M = (I_{max} - I_{min}) / (I_{max} + I_{min})$, where $I_{min}$ and $I_{max}$ are the total optical powers impingent on the OPU's photodetector when the optical axis of the focused playback spot is located exactly in the center of the mark and between the marks, respectively. It is also noticed that the readout SNR is proportional to $M^2$ (see e.g. ref. 14).

Fig. 1 shows the geometry of the SR disk with the recorded data marks that we used in the FDTD simulations. The layer structure is ZnS-$SiO_2$/$AgO_x$/ZnS-$SiO_2$/GST/ZnS-$SiO_2$, where the layer thicknesses are 18, 40 and 60 nm for $AgO_x$, (Spacer) ZnS-$SiO_2$ and GST layers respectively. The GST layer is in a fully crystalline phase as in the experiments. At low readout power, all of the recorded bubble marks are assumed to be filled with randomly distributed Ag aggregates (aperture radius = 0 nm). Aperture radius, in this context, is the area, where the intensity of the readout spot is enough to affect the Ag aggregates as mentioned before. In our model, the size of the aggregates was not specified, but the bubble was filled with randomly distributed Ag particles. The size of an individual particle corresponded to the computational cell size, which was 2 nm x 2 nm. In Fig. 2 the electric field amplitude calculated with the geometry shown in Fig. 1 is shown. The amplitude is increased inside the central bubble and therefore the reflection is decreased from the structure, which therefore increases the modulation of the signal.

## 3. RESULTS

The simulated modulation of the detected optical power for three different mark sizes is shown as the function of the aperture radius (readout power) in Fig. 3. The Ag concentration in the bubbles in these simulations is 70%. For the mark sizes of 150 nm and 200 nm, a clear resolution threshold is seen around a 100 nm aperture radius and for the 100 nm mark size, the threshold is around a 50 nm aperture radius. The improved modulation in this case arises from the reduced reflected optical power impinged on the detector at the on-mark situation, while the reflected power at the off-mark situation is fairly constant as a function of the aperture radius. At the threshold, the random Ag aggregates at the on-mark bubble pit (the mark, which is at the optical axis of the readout spot) gets organised and a doughnut-shaped structure is formed inside the bubble pit. But in all of the other bubble pits, the

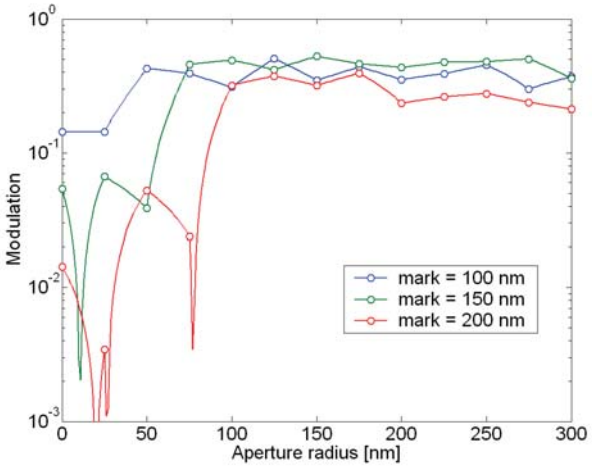


*Figure 3. The modulation of the reflected optical power as a function of the aperture radius for 100, 150 and 200 nm mark sizes. Aperture radius is assumed to be related to the readout power.*

Ag aggregates are still random in order. When the aperture radius is increased from the threshold and Ag aggregates also in other bubble pits are affected, the total reflected power at the detector in the on-mark and off-mark cases, however, do not change significantly from the threshold situation. Therefore, the doughnut-shaped structure in the on-mark bubble has a dominate effect in the improved modulation.

## 4. CONCLUSION

A new mechanism has been described that explains the nonlinear behaviour of the SNR as a function of the read-out power. This is achieved when the Ag aggregates drift away from the optical axis of the OPU with high read-out power and the low reflectivity region is formed in the central region of the focused laser spot.

## REFERENCES


1. J. Tominaga, T. Nakano, and N. Atoda: Appl. Phys. Lett. 73, (1998) 2078.
2. H. Fuji, J. Tominaga, L. Men, T. Nakano, H. Katayama and N. Atado: Jpn. J. Appl. Phys. 39 (2000) 980.
3. T. Kikukawa, A. Tachibana H. Fuji and J. Tominaga: Jpn. J. Appl. Phys. 42 (2003) 1038.
4. T. Kikukawa, T. Nakano, T. Shima, and J. Tominaga: Appl. Phys. Lett. 81 (2002) 4697.
5. W.C. Liu, C.Y. Wen, K.H. Chen, W.C. Lin and D.P. Tsai: Appl. Phys. Lett. 78 (2001) 685.
6. J. Tominaga, J. Kim, H. Fuji, D. Büchel, T. Kikukawa, L. Men, H. Fukuda, A. Sato, T. Nakano, A. Tachibana, Y. Yamakawa, M. Kumagai, T. Fukaya and N. Atoda: Jpn. J. Appl. Phys. 40 (2001) 1831.
7. T. Kikukawa, T. Kato, H. Shingai and H. Utsunomiya: Jpn. J. Appl. Phys. 40 (2001) 1624.
8. T. Shima, M. Kuwahara, T. Fukaya, T. Nakano and J. Tominaga: Tech. Dig. ISOM03 (2003) Fr-J-05.
9. F.H. Ho, H.H. Chang, Y.-H. Lin and D.P. Tsai: Jpn. J. Appl. Phys. 42 (2003) 1000.
10. Y.-C. Her, Y.-C. Lan, W.-C. Hsu and S.-Y. Tsai: Appl. Phys. Lett. 83, (2003) 2136.
11. B.S. Lin, D.P. Tsai and W.C. Lin: Tech. Dig. ISOM03 (2003) Th-H-02.
12. A. Taflove and S.C. Hagness, Computational Electrodynamics: The Finite-Difference Time-Domain Method (Artech House, Boston, 2000).
13. G. Bao, L. Cowsar, and W. Masters, Mathematical Modeling in Optical Sciences (SIAM, 2001).
14. C. Peng and M. Mansuripur: Appl. Opt. 37, (1998) 921.


Kari Kataja
*Kari.J.Kataja@vtt.fi*

Janne Aikio
*Janne.Aikio@vtt.fi*

Takashi Nakano and Junji Tominaga
*Center for Applied Near-Field Optics Research, National Institute of Advanced Industrial Science and Technology, C4, 1-1-1 Higashi, Tsukuba 305-8562, Japan*

# Porous Thin Films based on Phase Separation


## ABSTRACT

Porous thin films were fabricated using vinyltriethoxysilane and tetramethoxysilane as precursors. The phase separation method was employed to form porosity in hybrid organic/inorganic thin films.


## INTRODUCTION

Porous thin films based on sol-gel chemistry have been widely investigated during the last decade. These films are mostly pure metal oxide materials based on e.g. silicon-, zirconium- and titanium dioxide. Often, high temperatures are employed to fabricate porosity in thin films, where organic compounds are decomposed from the final thin film structure. There are also methods to fabricate porous organic/inorganic films in low temperatures, traditionally at +40-100 Celsius degrees, utilising the phase separation method.

The theory of phase separation from a single phase was given by Cahn and Charles[1]. There is a thermodynamic description for phase separation. A necessary condition for the stability of a phase with respect to infinitesimal composition or density fluctuations is that the chemical potential of each component increases with the increasing density of that component. This condition is not in conflict with the existence of a more stable phase, and thus metastability can and does occur more commonly. In some systems there exists a temperature, which is a function of composition, where this necessary criterion for stability breaks down. This limit to the metastability has been called the spinodal. Beyond the spinodal, a single phase is unstable with respect to infinitesimal composition fluctuation and begins to separate into two related phases differing only in composition. This occurs spontaneously, without the need for nucleation, since the phase is no longer metastable but unstable.

Usually, four reagents are necessary to form porous oxides: a source of the small metal-oxide ions, a surfactant, a solvent and a chemical to adjust the pH. If we consider silicon oxide source, the strong interaction between the silica species and the surfactants leads to the phase separation of the silica/surfactant arrays into microdomains that have an ordered liquid crystalline structure. The sur-

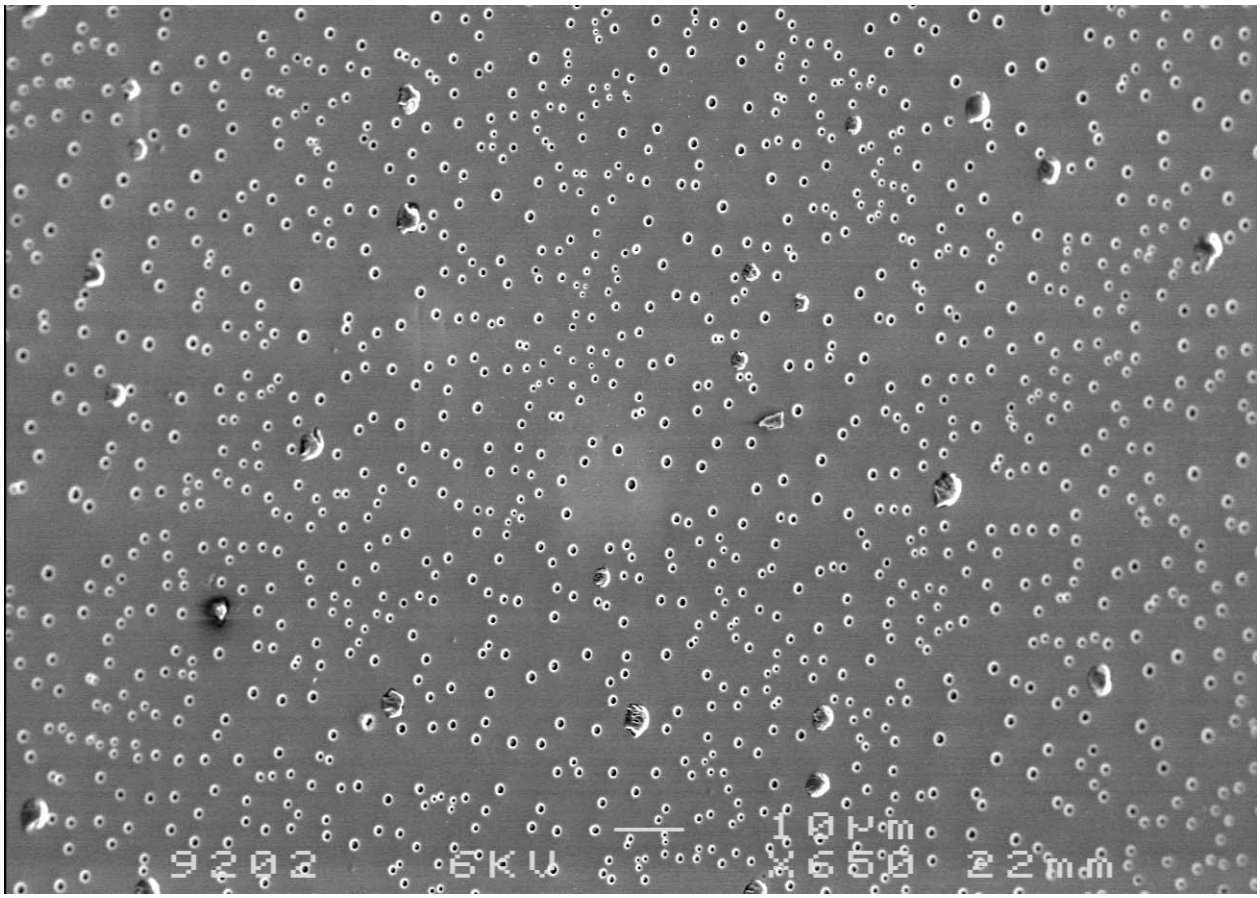


*Figure 1. SEM photograph from the surface of the porous material (view angle was 40° and operating voltage 6 kV).*

factants can be removed from the inorganic network by washing or calcination. Structural control of pores can be achieved e.g. using polar cosolvents. The organisation of molecular silica and surfactant precursors into an inorganic/organic array depends on a thermodynamic phase transition. By using cosolvents it is possible to alter the solution thermodynamics and exert a measure of control over the synthetic process. For example, cosolvents allow nonaqueous synthesis and enable the pore diameter to be tuned.[2]

## EXPERIMENTAL

Tetramethoxysilane and vinyltriethoxysilane precursors were stirred vigorously in a round bottom flask equipped with the reflux condenser to achieve a homogeneous solution. A solution containing formamide and methanol as solvents and nitric acid as a pH adjusting chemical was added dropwise to the flask and solution was cooled to 0 Celsius degrees and stirred for 5 minutes. Then, the formed sol-gel material was aged in an open container (gelation) for an additional hour.

Material was dip-coated on glass slides and thin films were baked in the oven (+ 40°C) overnight and additionally next day at +60°C for 5 hours. Thin films were characterised using Field Emission Scanning Electron Microscope (FESEM). In Figure 1, a dip-coated porous thin film can be seen.

## RESULTS

Hybrid organic/inorganic silane precursors were used to fabricate porous thin films in low temperatures (+40-60°C). The phase separation method was employed using polar solvent, formamide, to form pores in a liquid state. The pore size was approximately 1 µm. Porosity can be tuned to smaller ones using different molar ratios of silane precursors, solvents and amount of acid.

## ACKNOWLEDGEMENTS

The authors are grateful to National Technology Agency (TEKES) and VTT Electronics for financial support.

## REFERENCES

1. J.W. Cahn, R.J. Charles, The Initial Stages of Phase Separation in Glasses, Physics and Chemistry of Glasses 6 (5) (1965) pp. 181-191.

2. M.T Anderson, J.E. Martin, J. Odinek, P. Newcomer, Synthesis of Surfactant-Templated Mesoporous Materials from Homogeneous Solutions in the book Access in Nanoporous Materials (Fundamental Material Research), Edited by T.J. Pinnavaia and M.F. Thorpe, Plenum Press, New York, 1995, pp. 29-37.

Mikko Keränen
*Mikko.Keranen@vtt.fi*

Arto Maaninen
*Arto.Maaninen@vtt.fi*

Hanna Männikkö
*Hanna.Mannikko@vtt.fi*

Johanna Hiitola-Keinänen
*Johanna.Hiitola-Keinanen@vtt.fi*

# Near Field Holographic (NFH) Pattering of Sub-Micron Periodic Structures

## INTRODUCTION

Near field holography (NFH) is a technique for the manufacturing of planar grating structures with periods between 200 and 600 nm. Such structures are typical, for example, in devices used in guided wave optical communications, where very narrow optical bands are required. The method uses a mask and holographic exposure to transfer the grating period into photoresist on a substrate, as illustrated in Figure 1. The zeroth diffraction order passes through the phase mask plate whereas the first diffraction order is diffracted with an angle that has the same value as the impinging beam but is directed to the opposite side. When these diffraction orders have the same intensity, the resulting interference pattern has the same pitch as the original grating. The method is called near field lithography, because a conventional mercury lamp with a band narrowing filter is used in illumination having limited coherence and, thus, the interference pattern formation is limited to close to the mask [1]. VTT electronics' exposure and mask aligner unit (MA6 by Suss MicroTech) is equipped with NFH capabilities.

## EXAMPLE STRUCTURES

Because the NFH technique produces a regular wave pattern, it is possible to form gratings with higher order rotational symmetry by repeating the exposure phase several times and rotating the substrate between each step. Examples of NFH manufactured gratings are shown in Figures 2. and 3., where photoresists were patterned using NFH exposure and the development procedure. Figure 2. shows a 1-dimensional grating, which was manufactured with one exposure step. The 2-dimensional grating shown in Figure 3. was formed by rotating the substrate by 90° between two exposures. The period in both gratings is 400 nm, which is equal to the pattern in the holography mask.

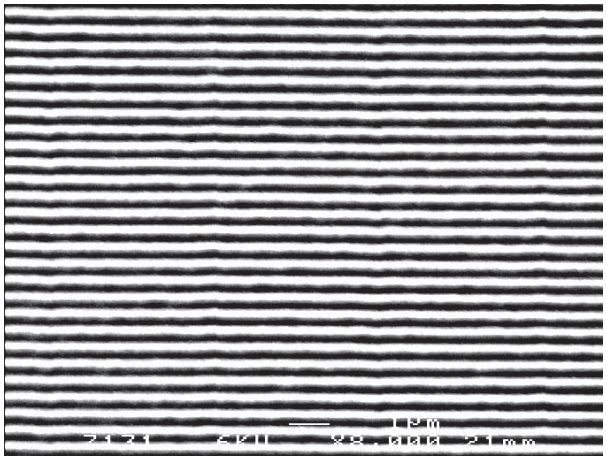

*Figure 2. 1-dimensional grating with 400 nm period.*

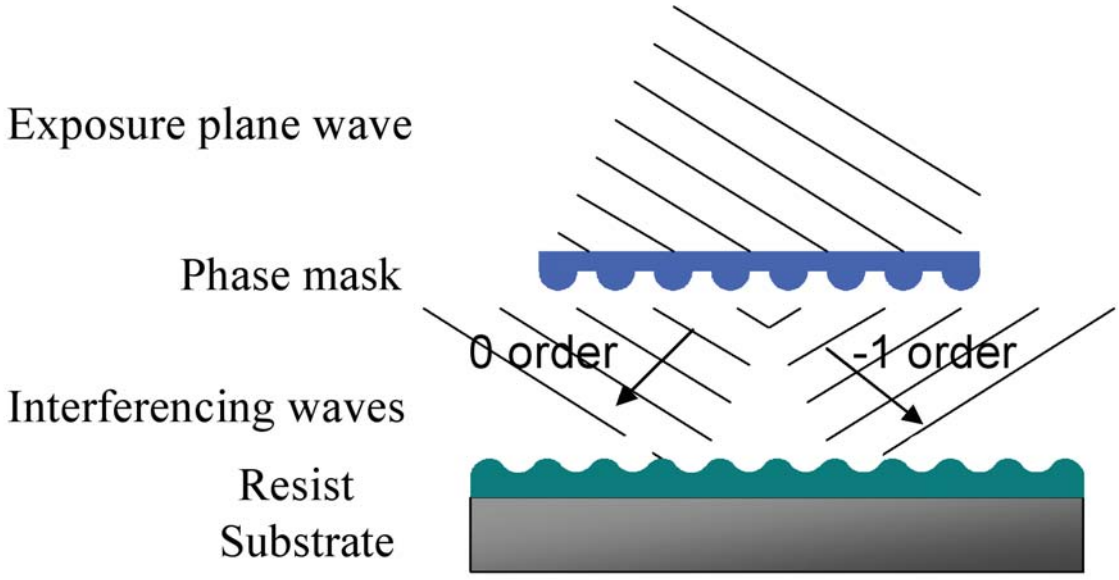


*Figure 1. Near field holographic patterning.*

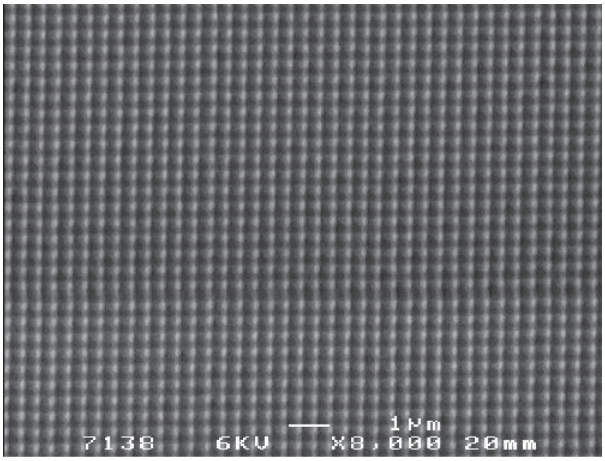


*Figure 3. 2-dimensional grating with 400 nm period.*

## REFERENCES

1. E. Cullmann, Photonics Spectra, April 2004, pp. 110-112

Jussi Hiltunen
*Jussi.Hiltunen@vtt.fi*

Sami Karjalainen
*Sami.Karjalainen@vtt.fi*

Mikko Karppinen
*Mikko.Karppinen@vtt.fi*

# Modelling and Fabrication of Ceramic Modules for Micro and Millimetre Waves

## INTRODUCTION

Low temperature co-fired ceramic (LTCC) technology offers a lot of benefits for micro and millimetre wave applications. These materials have stable dielectric properties with low losses and the conductors used, like Ag, Au and Cu, have low resistivity. The technology also offers an efficient way to integrate several different functions in one package. At this moment, one of the limiting factors is the lack of infrastructure for the design of multilayer structures for millimetre waves. In the Tekes-funded project "Advanced ceramic modules for RF and microwave applications", models for multilayer inductors and different vertical interconnections were developed. The models were verified by several test circuits. During the 2nd year, several demonstrators were designed and realised for both radio frequencies and microwaves. The research partners in the project coordinated by VTT Electronics were the University of Oulu and VTT Information Technology. This report presents some results from this project.

## MODELLING

The basic structures in LTCC technology are resistive, capacitive, inductive and transmission line structures. These components have different parasitic effects whose influence is emphasised when the operating frequency and integration level increases. Current circuit simulators do not take into account these high-frequency effects. For example, there is a model for a planar single-layer coil in an APLAC circuit simulator but the modelling of multilayer coils is not straightforward. Therefore, the multilayer coil was selected to be modelled in more detail. The modelling commenced by solving electromagnetic fields that were then utilised to define the capacitances and inductances. These were used to form an equivalent circuit which was then implemented into APLAC. Similar inductors were realised and the measured scattering parameters matched well with the simulated ones up to 1st resonant frequency at 2.5 GHz.

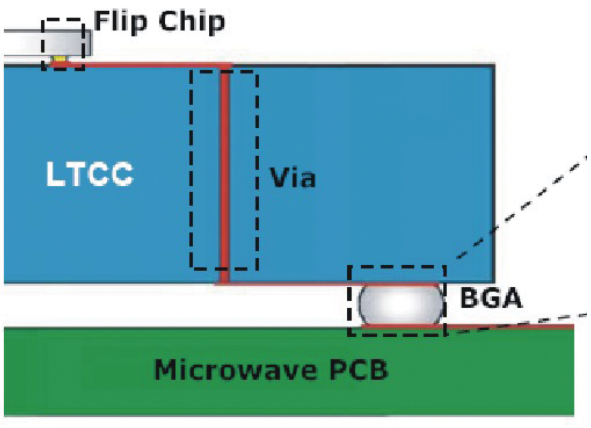


*Figure 1. Vertical interconnections needed for modelling.*

In addition to a multilayer coil, different transitions were also modelled. These transitions are needed inside or outside LTCC module as shown in Fig. 1. The main goal of this task was to develop geometrically accurate parameterised RF circuit models for these transitions. Distributed RLGC values were utilised in the realisation of circuit models. These values, on the other hand, depended on e.g. the size of vias, thickness of LTCC substrate and the pitch of signal and ground vias.

## LTCC MATERIALS AND PROCESSING

Higher operating frequencies set tighter requirements on LTCC materials and manufacturing techniques. The most commonly used LTCC system is Du Pont 951, which has also been used in RF applications. However, its properties are not necessarily adequate for millimetre waves. Therefore, several other material systems, such as Heralock, Ferro A6-S and Du Pont 943, were studied in this project.

Heralock offers the advantage to be an accurate interconnection board due to its non-shrinkage properties. The high-frequency properties of Heralock were characterised and it was found to be quite comparable with the conventional Heraeus CT2000 tape system; and being much better than Du Pont 951.

The Ferro tape system allows the use of buried and surface resistors. These were realised e.g. as attenuators and were characterised up for millimetre waves. Attenuators had attenuation values between 3 and 12 dB, and they were realised in both T- and Π types. T-type attenuator worked better and it had the measured insertion loss of about 3.5 dB at lower frequencies as designed. At 50 GHz the insertion loss increased slightly to 4.5 dB and the return losses were better than 17 dB along the whole frequency range as shown in Fig. 2.

For micro and millimetre waves, the accuracy of conductor lines becomes more important due to the current crowding effect. Conventional screen printing is not necessarily a good enough method. Therefore, alternative processing techniques, such as etching and photopatterning, have been developed. In the photopatterning technique, a uniform layer is first printed on the tape and dried. Then the mask is aligned and UV-exposure is made after which the non-exposed paste areas are removed in the development process. So far, the selection of avail-

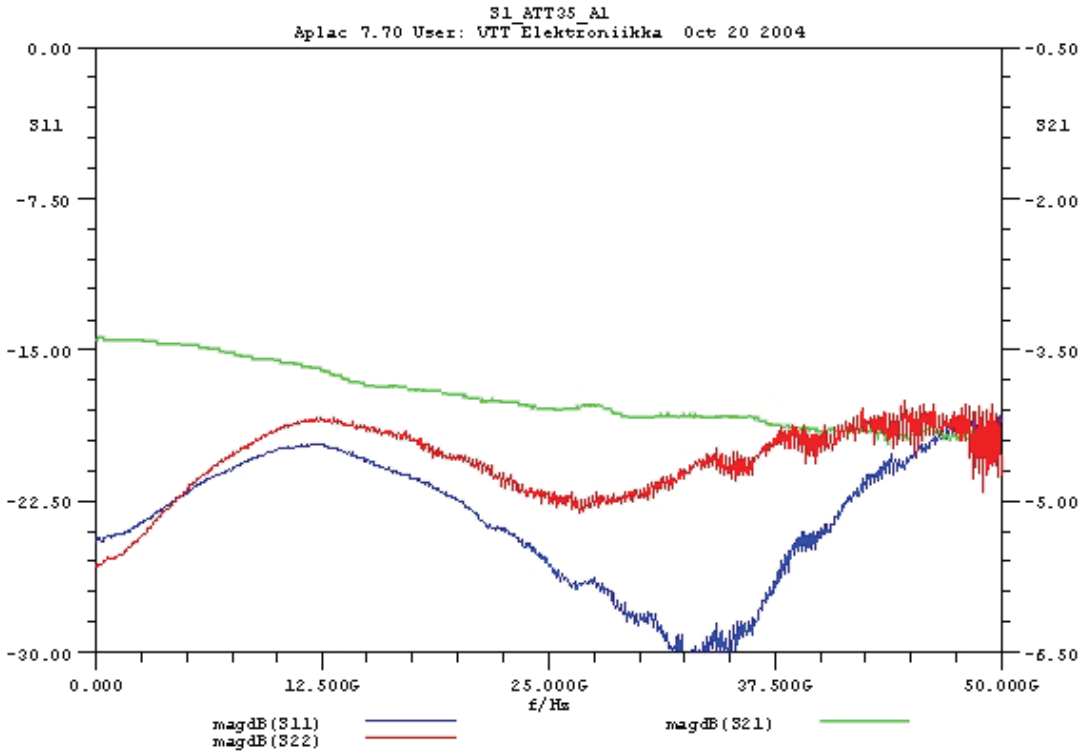


*Figure 2. Typical measurement results from 3.5 dB T-type attenuator realised on the surface of Ferro A6-S substrate.*

able photoimageable pastes has been quite limited. In addition to Fodel photoimageable pastes from Du Pont, at least Heraeus and Hibridas offer these kinds of pastes. In this project, two types of Hibridas conductor materials and one type of multilayer dielectric were tested. Hibridas delivered 1"x1" alumina substrates with the photoimaged material printed and dried on it to be exposed, developed and fired at VTT. The purpose of this test was to evaluate the feasibility of Hibridas materials for fine-line applications. The exposure at VTT was achieved using a screen exposure unit with UV intensity of 40 mW/cm$^2$ through a chromium glass mask. The development was performed with a spray developer using 0.8% sodium carbonate solution. The firing was performed using a conventional 850 °C / 10 min profile. The line quality was quite similar in comparison to the reference samples received from Hibridas. The narrowest line widths in these tests were about 35 µm as shown in Fig. 3.

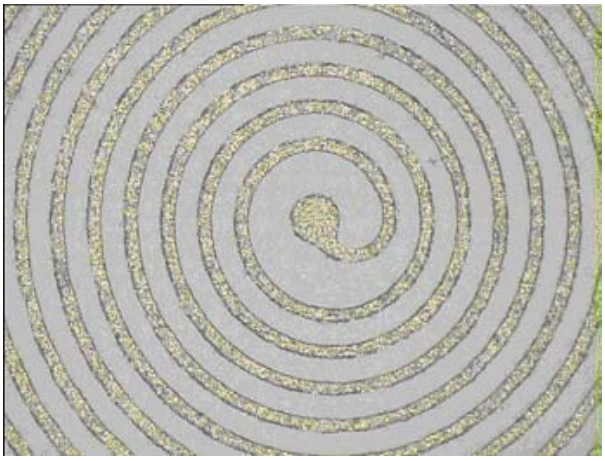

*Figure 3. 35 µm wide fired photopatterned Ag lines.*

## PROTOTYPE MODULES

Several demonstrator modules were fabricated in the project. The specifications were defined together with industrial partners. The first demonstrator was a high-power bias-T structure for radio frequencies. Different transmission line topologies and LTCC substrate material options were studied by modelling, and the test circuit was fabricated on a Ferro A6-S tape system. The second demonstrator was a low-noise amplifier module also for radio frequencies. This module consisted of 6 tape layers and contained a mixed Au and Ag conductor system. It contained several bare dies and their assembly in cavities proved to be a challenging task due to high temperature required by SnAu solder. The conventional Du Pont 951 tape system was utilised in this demonstrator. The characterisation of these two demonstrators is currently under way. The third demonstrator was mm-wave bandpass filter module at the centre frequency of 22.5 GHz. It utilised an edge-coupled stripline structure where the narrowest

designed line gaps were about 100 µm. The insertion losses were less than 2 dB including transitions to the surface of the LTCC substrate. The insertion losses were better than specified. Also the repeatability between samples was good. The measured centre frequency was 23.3 GHz and this small shift in comparison with the designed one was due to the variation of line widths in the fabricated modules. This filter was realised in the A6-S tape system due to its low losses for millimetre waves in comparison with other tape systems.

## CONCLUSIONS

Both modelling and manufacturing issues for micro and millimetre waves were studied in this project. In the modelling, some specific components and structures were selected to be focused on. The model for multilayer coil was developed starting from electromagnetic calculations and the developed model was then implemented in an APLAC circuit simulator. Internal and external vertical interconnections were modelled by 3D electromagnetic simulation tools. From the manufacturing point of view, the high-frequency properties of different LTCC systems were studied. The know-how from different partners was combined by developing several demonstrator modules from RFs to microwaves.

Markku Lahti
*Markku.Lahti@vtt.fi*

Antti Vimpari
*Antti.Vimpari@vtt.fi*

Tero Kangasvieri
*University of Oulu, Microelectronics Laboratory*
Juha Volotinen
*VTT Information technology*

Kari Kautio
*Kari.Kautio@vtt.fi*

# Microwave Stubs in LTCC Technology

## INTRODUCTION

This article presents some results from a collaboration programme between VTT and CRC. The programme focuses on the application and fabrication of LTCC technology for mm-wave frequency communications. The multi-level stubs presented in this paper have been designed by the Communications Research Centre (CRC) and manufactured by VTT Electronics. A very low-loss tape system is desired for millimetre-wave applications. DuPont 943, which is one of such systems, was used in this work.

CRC is the Government of Canada's primary laboratory for research and development in advanced communications technologies. Its R&D addresses rural and remote broadband access, spectrum issues, wireless and satellite communications, radio fundamentals, broadcast and multimedia technologies, broadband networks and photonics. CRC (http://www.crc.ca/) is located in the western end of Ottawa, Ontario, and has a technical staff of 220.

VTT Electronics has the experience of processing many of the commercially available LTCC material systems, such as DuPont 951 and 943, Ferro A6S, Heraeus CT 2000 and Heralock. Some advanced LTCC material systems, such as high-K, mixed-K and ferrite systems have also been evaluated. The characterisation of integrated passive components for microwave and mm-wave frequencies, as well as the development of fine-line technologies, have been an important part of LTCC research work at VTT.

## LTCC STUBS

To realise the benefits of a highly dense packaging technology like LTCC, designers would like to be able to integrate the passive components into the substrate, to lower costs as well as overall circuit size. An important component for microwave circuit designers is the stub. Stubs are used for filtering and impedance matching. Stubs can be arranged in series or in parallel, and by adjusting the stub termination, can be used to present specific impedances for a microwave circuit. Typically shunt, or parallel, stubs are used due to the difficulty involved in building series stubs. One way of building a series stub is to use uniplanar technology like coplanar waveguide (CPW), and to locate the series stub inside the centre conductor of the transmission line. Unfortunately, this technique is not suited to the LTCC environment, since the minimum line and gap spacing required in LTCC make these structures too wide, and therefore prone to spurious resonances. A way to avoid this width problem is to use the multi-layer nature of LTCC to build the stub above the signal line, as shown in Figures 1 and 2.

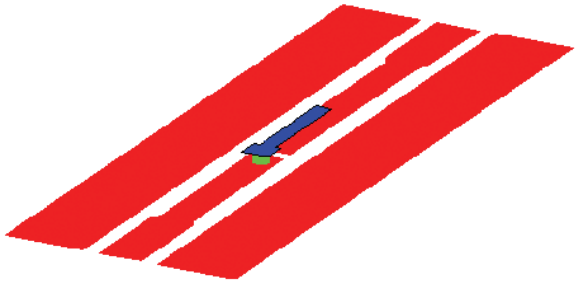

*Figure 1. Isometric view of an open-circuit series stub used with a CPW transmission line.*

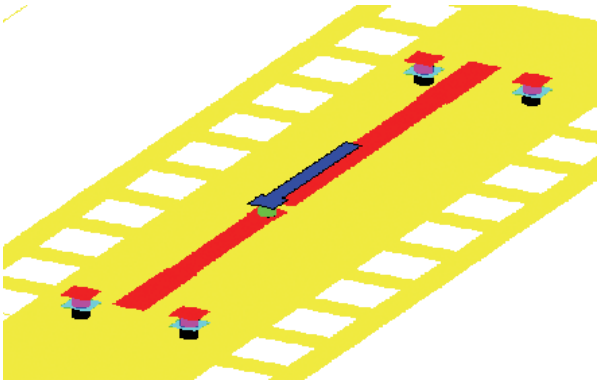

*Figure 2. Isometric view of an open-circuit series stub used with a microstrip transmission line.*

In the circuits of Figures 1 and 2, the stub section can be considered a microstrip transmission line, with the signal line below it acting as its "ground." In this way, the circuit can be modelled as a series stub followed by a section of transmission line, as in Figure 3.

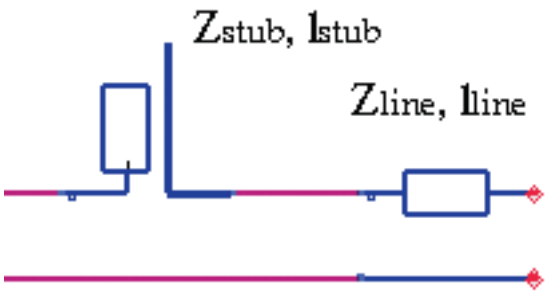


*Figure 3. Circuit model of multi-layer open-circuit stub.*

The stub impedance, Zstub, is determined by the width of the stub section as well as its height above the signal line. The impedance of the following transmission line Zline is determined by the height and width of the signal line but is lowered due to the capacitive effect of the gap in the signal line.

It was found that the simple circuit model of Figure 3 gives quite good agreement with the measured results. The circuit of Figure 1 is well approximated by the circuit model of Figure 3 with Zstub = 46 Ω and Zline = 44 Ω.

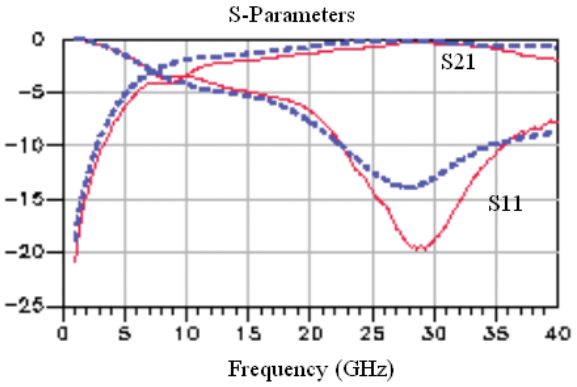


*Figure 4: S-Parameter comparison between circuit model of Figure 3 (dotted) and measured results of structure of Figure 1 (solid).*

Since the stub sections of Figures 1 and 2 have the same geometry (same width, same height over the signal line) they should have the same impedance. The circuit model confirms this, and gives a good agreement for the circuit of Figure 2 with Zstub = 46 Ω and Zline = 36 Ω.

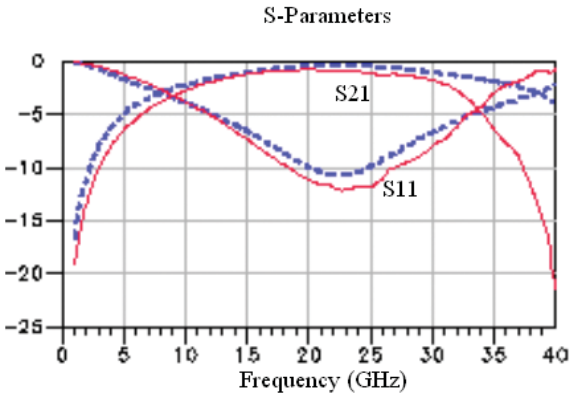


*Figure 5: S-Parameter comparison between circuit model of Figure 3 (dotted) and measured results of structure of Figure 2 (solid).*

The reason that the Zline impedance is lower in the case of a microstrip environment compared to a CPW environment is because a gap in the signal line has a greater capacitive effect on a microstrip line than on a coplanar line. This capacitive effect acts to lower the Zline impedance.

## BANDSTOP FILTER APPLICATION

Since the circuit model seemed to give good agreement, the principle was tested by building a bandstop filter. This filter was built by connecting two series short circuit stubs on either side of a shunt open-circuit stub, as shown in Figure 6. The series stubs were implemented as in Figure 2.

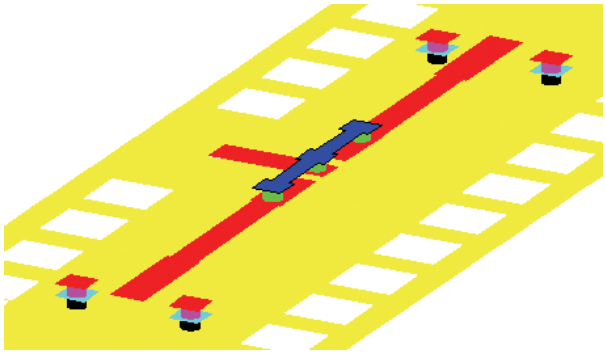

*Figure 6: Isometric view of bandstop filter.*

The circuit was designed using the previously developed multi-layer circuit model of Figure 3, and then simulated using the commercial electromagnetic simulator Momentum.

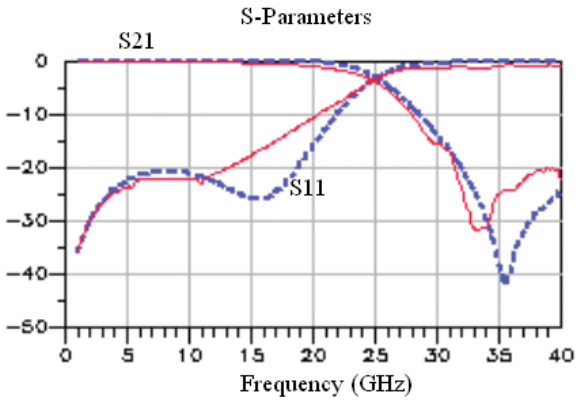


*Figure 7: Comparison of Momentum simulation (dotted) and measured results (solid) for the bandstop filter of Figure 6.*

The filter works well as a bandstop filter, and has good agreement with the Momentum simulation.

## CONCLUSION

Multi-layer stubs for LTCC packages have been developed, and proof-of-concept has been shown with a bandstop filter centred at 44 GHz.

## REFERENCES

Panther, A.; Stubbs, M.G.; Kautio, K.; Multi-Layer Stubs in LTCC Technology. 2004 European Microwave Conference Digest, 617-620.

Antti Vimpari
*Antti.Vimpari@vtt.fi*

Kari Kautio
*Kari.Kautio@vtt.fi*

Alex Panther, Malcolm Stubbs
*Communications Research Centre, Ottawa, Canada*

# Passive Alignment of Devices on LTCC Substrates in Photonics Modules

A concept that utilizes structured planar substrates based on low temperature co-fired ceramics (LTCC) as a precision platform for miniature passive alignment multimode laser module is studied. The 3-dimensional shape of the laminated and fired ceramic substrate provides the necessary alignment structures including holes, grooves and cavities for the laser to fiber coupling. The developed technology can be utilized in the passive alignment of devices in photonics modules. Optical coupling efficiency of the multi-mode laser system was simulated using optical systems simulation software. The nominal coupling efficiency between 100 µm x 1 µm stripe laser and 62.5/125 µm graded index fiber (NA=0.275) was 0.37. Prototype realizations and characterizations of the two systems (AT and A2) verified the simulated coupling efficiency and alignment tolerances. The measured alignment tolerance values between laser and fiber in AT prototype series were $\Delta x$=7.7 µm, $\Delta y$=7.6 µm and $\Delta z$=10.8 µm (SD values). The corresponding values in A2 prototype series were $\Delta x$=3.1 µm, $\Delta y$=9.1 µm and $\Delta z$=10.2 µm. The measured average coupling efficiency was 0.28 in AT series and 0.31 in A2 series. The coupling efficiencies of all operational prototypes varied from 0.05 to 0.43.

## I. INTRODUCTION

Photonic module manufacturers pursue miniature, long term stable and precise module realization and assembly technologies in order to achieve cost-effective solutions for market demands. Integration of photonic, electrical and mechanical functionalities into a one system can improve the cost-efficiency of systems greatly. Monolithic integration is seen as most cost effective method to produce photonic modules due to the fact that packaging costs, which normally is the largest part of photonic module production cost, is minimized [1]. The cost-effective monolithic integration of photonic systems still meets an extensive challenge [2]. Hybrid integration of InGaAsP/InP sources and silica fibers using passive alignment silicon waferboard is suggested and demonstrated for producing optical communication modules [3]. Research work has lead to the demonstration and utilization of planar lightwave circuits (PLCs) [4]. Hybrid integration, however, seems to offer a very competitive solution for optical communication modules, also [5]. In some applications, such as in the realization of high power optical transmitter modules needed in sensor and tooling applications, the hybrid integration seems to be the only practical method [6].

The use of passive alignment in the production of hybrid integrated modules is advantageous especially in volume production, due to the fact that method is simple and fast [7]. Silicon micro-machining technologies that are used in the microelectronics industry are widely applied to tool silicon precision substrates for the passive alignment fiber optic subassemblies. The accuracy of processed silicon substrates is adequate for passive alignment of single mode photonic devices and components [8]. High mask production and processing costs, however, typically limits the use of silicon processing technology in devices, which are not cost sensitive or are produced in very large volume. Medium and low volume production pursues methods with high flexibility and low processing costs. In order to meet the processing cost requirements of medium and low volume production of alignment substrates, a concept in which alignment grooves are embossed into metallic substrates, has been suggested [9].

We have studied the possibility of creating passive alignment substrates for the hybrid integration of high power laser diodes with micro-optical components and silica fibers using low temperature co-fired ceramic (LTCC) technology. LTCC and thick film materials have a long history of meeting the most demanding electronic packaging and interconnect material requirements [10]. Low conductor resistance and dielectric loss, multi-layer structures with fine-line capability, compatibility with hermetic sealing and the ability to integrate passive electrical components into the substrate make LTCC a useful technology for optical MEMS and communication applications [11]. The cost efficiency of the LTCC technology -based photonic transmitter module in volume production is advantageous due the fact that, LTCC panel manufacture and component assembly are realized using standard high volume applicable production methods, such as, screen printing, flip-chip assembly of devices and surface mount assembly and reflow soldering of components. The cost efficiency of LTCC technology, however, is not limited to high volume applications, but it is also applicable to low and medium volume applications because process related initial and mask costs are typically moderate compared to silicon and LIGA processes.

## II. LASER TO FIBER COUPLING SIMULATIONS

The simulation of the passive laser-to-fiber coupling utilizing LTCC test substrates commenced by performing optical coupling efficiency analysis between 1x100 µm emitting area laser and 62.5/125 µm fiber, NA=0.275. The laser beam full width divergence 10 x 56 degrees, when the 1/e2 intensity values were applied. The emitted power center wavelength was 808 nm. The coupling simulation and tolerance analysis systems were built using ASAP™

(Breault Research Organization) optical design and simulation software. The multi-mode laser model used in the simulations obeyed Gaussian intensity angular distribution in the far-field Y-direction and top hat in the X-direction. The laser model had top hat spatial irradiance distribution in both directions. The simulation model was fitted to the manufacturer's data. An example of the modeling of an edge-emitting stripe laser optical power coupling to a multi-mode fiber using a ball lens is shown in Fig 1.

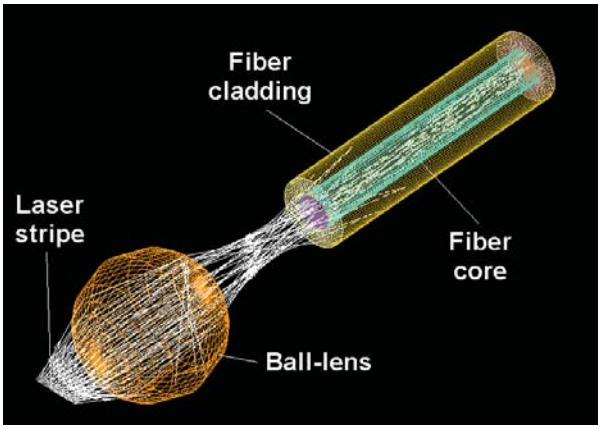


*Fig. 1. An example modeling laser-to-multi-mode fiber coupling utilizing a ball lens*

The nominal coupling efficiency in butt coupling achieved in the simulation was 0.37, when a nominal distance of 30 µm between laser and fiber was used. The tolerance analysis of the coupling system was performed in two steps. Firstly, the sensitivity analysis of the system was performed. In the sensitivity analysis each tolerance variable using $3\sigma$ value is simulated separately and the most critical tolerance variables are found, which enables system optimization. The fiber decenter along the Y-axis is the most significant tolerance variable with the used tolerance values.

Secondly, optical system Monte-Carlo tolerancing was performed, Fig.2. In Monte-Carlo tolerancing, all tolerance variables are simulated simultaneously and statistical information of system performance is obtained. Variables are represented as distributions in the simulations. Only two variable distributions had non-Gaussian distribution, namely source tilt y and fiber tilt y. All of the other variable distributions had Gaussian distribution.

As we can see from Fig 2. the maximum coupling efficiency peak is around 0.37 and the maximum value is about 0.4, when using 10.000 MC systems in the simulation.

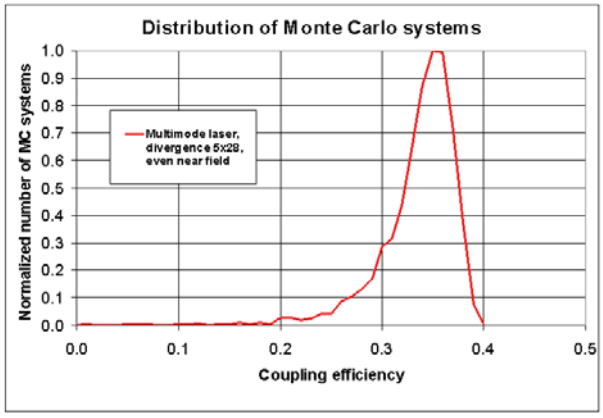


*Fig 2. Relative coupled power of systems by Monte-Carlo tolerance analysis*

## III. LTCC PROCESSING OF HYBRID INTEGRATION SUBSTRATES

The fabrication of a multilayer ceramic substrate using LTCC technology is shown in Fig. 3. First, glass ceramic sheets are blanked to the specified panel size. Secondly, the sheets are punched in order to form via holes. Via holes are metallized to create electrical interconnections between layers. The next step is the patterning of electrical conductors and passive circuits onto each layer using screen-printing or photo imaging. The final steps are layer lamination, firing below 980 °C temperatures and circuit dicing. Relatively low sintering temperature allows the use of metal conductor materials, such as, silver and gold. Assembling discrete devices into the substrate finishes the system on chip (SOC).

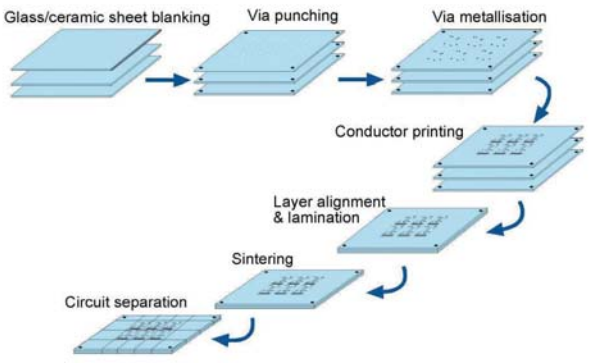


*Fig 3. Standard LTCC process*

The passive alignment of edge emitting laser-to-multimode fiber alignment was studied using LTCC substrates. The purpose of these experiments was mainly to evaluate the passively aligned fiber position and its accuracy. Two methods of manufacturing fiber grooves were tested, namely, punching and photo-imaging.

The shape of the alignment groove was affected using different combinations of lamination foils, e.g. Tedlar film (25µm), polyethylene foil (60µm), latex rubber foil (300µm) and steel foil (50µm). By using flexible foils, a V-shaped groove can be laminated, see Fig. 4a. Steel, being a rigid material, reduces the lamination force to the cavity edges and, therefore, produces a fairly orthogonal shape for the groove, as seen in Fig. 4b. To evaluate the fiber passive alignment accuracy to the manufactured grooves, a 10/125 µm single-mode fiber without jacket was pressed against the groove and attached to the substrate using a UV-curable epoxy.

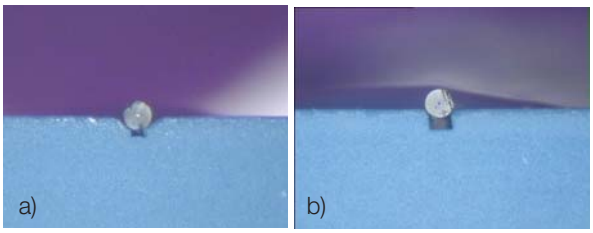


*Fig.4. Punched and laminated fiber grooves on LTCC, a) flexible foil, b) rigid foil*

Photo-imageable thick film conductor materials have been previously demonstrated to produce very accurate features and only a few micron edge resolution. The processing steps include the screen-printing of UV-sensitive paste on a fired substrate, exposure through a photo-mask, spray development and finally firing at about 850°C. Similarly, photo-imageable glass paste can be used to manufacture alignment structures on a fired substrate. The benefit of using glass instead of conductive paste is that a thicker layer can be exposed and imaged using only a minimal amount of UV energy. The cost of glass material is lower than conductive paste, also [12].

To manufacture the experimental fiber grooves, either three or four layers of photo-imageable glass were screen printed and dried on alumina or LTCC substrates. The exposure was performed on a regular screen exposure unit. The exposure intensity was 1mW/cm$^2$ and exposure time 10 seconds. The used chromium glass mask had a track width of 70 µm and a track spacing of 80 µm. The exposed pattern was spray developed using 0.8 % sodium carbonate, followed by water rinsing and spin drying. The patterned glass tracks were fired in a belt furnace, using a standard 850°C thick film profile. The firing shrinkage typically reduced the track width a 50 µm, corresponding to a groove width of 100 µm. The fired thickness of the glass track for three and four printed layers was 40 µm and 48 µm, respectively. Pieces of 62.5/125-micron multimode fiber were attached to the grooves using UV-curable epoxy. The typical shape of the photo-imaged groove pattern and the assembled fibers are shown in Fig.5.

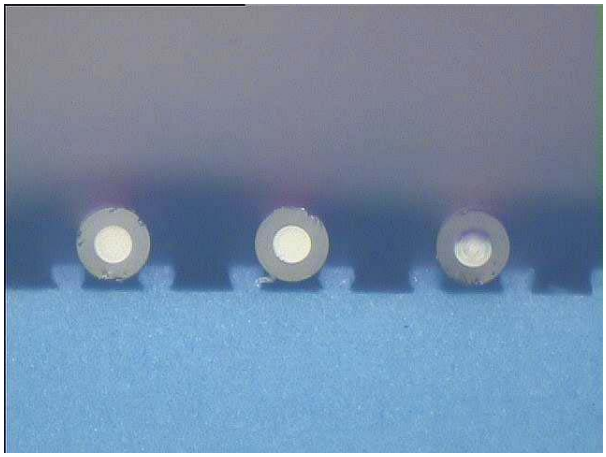

*Fig. 5. Photo-imaged fiber grooves on LTCC*

## IV. MODULE PACKAGING

A laser fiber pigtailed module series consisting of 40 modules in two different series, namely AT and A2, were realized using a six layer LTCC substrate, sized 22mm x 25mm, to evaluate the multimode fiber-to-edge emitting laser passive alignment accuracy and the thermal characteristics of LTCC for the packaging of high power lasers.

The demonstrator assembly started with laser chip alignment and attachment to the LTCC substrate gold metallization. The laser chip dimensions were 117 µm (H) x 200 µm (W) x 1000 µm (L). The laser diode was aligned with a Fineplacer flip-chip bonder and attached by a 50%In/50%Pb solder preform to the LTCC substrate. Solder preform of size 200 µm x 200 µm and thickness 20 µm was used for the attachment. The laser diode was placed on the preform and heated to 280°C during 90 seconds and cooled freely after solder wetting. The upper contact was wire-bonded with a wedge-bonder using 25 µm diameter gold wire.

A 62.5/125 µm multi-mode graded-index NA=0.275 fiber (Spectran) was aligned manually to the LTCC groove under a microscope. The separation between the laser and the fiber was adjusted to about 40 um. The fiber was pressed to the groove using a small weight at the fiber center and epoxy bonded using three separate drops of Loctite 3525 UV-epoxy. The strain relief was realized by bonding the fiber buffer to the widened groove using the same epoxy. The epoxy was hardened using a Novacure UV-source and a dose of 1000 mW/cm2 for 10 seconds. A close up of the laser to fiber coupling can be seen in Fig. 6.

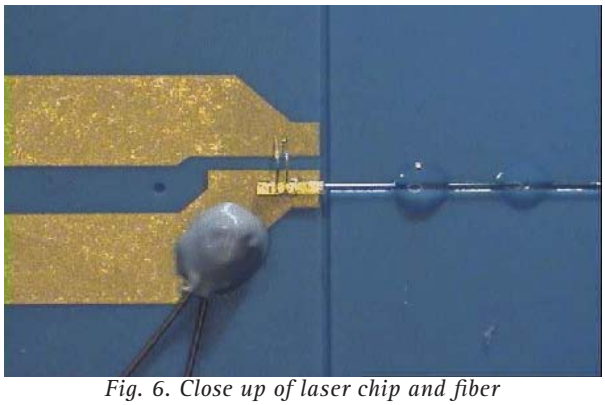

*Fig. 6. Close up of laser chip and fiber*

## V. MODULE CHARACTERIZATIONS

The realized accuracy of laser diode and fiber alignment on the LTCC substrate was characterized by measuring alignment errors of assembled components from the realized modules. Veeco white light interferometer, model Wyko NT-3300, and optical 3D coordinate measurement system, model Smartscope 200, were used in the measurements. The used coordination in the tolerance measurements is shown in Fig. 7.

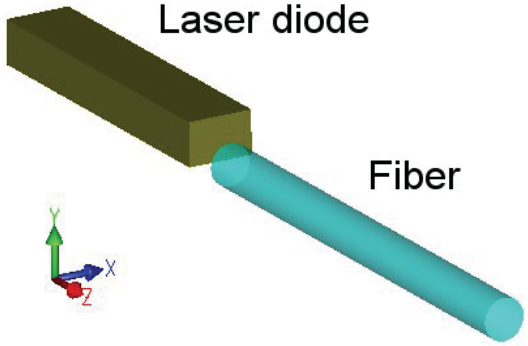


*Fig. 7. Coordination in laser-to-fiber coupling*

In Table 1 the measured alignment tolerances are shown.

*Table 1. Measured laser-to-fiber alignment errors*

| Serie | LD heigth [µm] | Groove width [µm] | LD/fiber dz [µm] | LD/fiber dx [µm] | LD/fiber dy [ µm] |
|---|---|---|---|---|---|
| AT Serie Mean | 124.7 | 111.1 | 42.8 | NA | 17.1 |
| A2 Serie Mean | 127.2 | 109.8 | 39.5 | NA | 10.4 |
| AT Serie SD | 2.2 | 3.5 | 14.2 | 7.7 | 7.6 |
| A2 Serie SD | 3.8 | 5.1 | 10.2 | 3.1 | 9.1 |

LTCC substrate surface was used as a reference surface, when measuring laser diode and fiber with absolutely assembly accuracy in the Y-axis direction, which was seen as the most critical tolerance in the sensitivity analysis. The fiber Y-axis average offset was +17.1 µm in the AT series and +10.4 µm in the A2 series. The laser diode Y-axis average offset was -0.3 µm in the AT series and +2.2 µm in A2 series. We could not measure, however, absolute assembly accuracy in X and Z directions due to the lack of proper reference surfaces/marks. Due to the same reason we could not also define the offset of components along the X-axis. The assembly accuracy in X- and Z-axis directions was characterized by measuring the relative alignment error between laser and fiber. The difference between the series was that AT series precision structure tape thickness after sintering was 90 µm and A2 series tape thickness was 130 µm.

As one can see from Table 1, the transverse alignment errors in both series are under 9.1 µm, which suggests good coupling efficiency between laser diode and fiber.

The coupling efficiency of the modules were measured so that the laser power was first measured after assembly with an optical power meter applying a 10 mm square silicon detector. Due to the fact that total power could not be measured with the set-up, a correction factor applied by system optical simulation was used to define the total optical power emitted by the laser diode. Secondly, the fiber-coupled power was measured. The coupling efficiency is achieved simply by dividing fiber-coupled power by total power. The average coupling efficiency and distributions are shown in Table 2.

*Table 2. Average coupling efficiencys and distributions*

| | |
|---|---|
| AT Mean | 0.39 |
| A2 Mean | 0.43 |
| AT SD | 0.14 |
| A2 SD | 0.18 |

The total number of operational modules was 13 in the AT series and 16 in the A2 series. The total number of modules was 40. The laser output was found to be poor in the pre-study with 11 modules and fibers were not assembled on those modules.

As one can see from Table 2, the average coupling efficiency in A2 series is better than in AT series. This is well consistent with the fact that the measured alignment errors are smaller in A2 series than in AT series. The distri-

bution of coupling efficiencys in both series in much wider than expected from the simulations. Laser near- and far-field intensity distributions were measured in order to see the accuracy of the used laser model. Near-field intensity distribution was measured by imaging laser facet to a CCD camera detector using microscope objective. In Fig. 8, an example of measured spatial intensity distribution is shown.

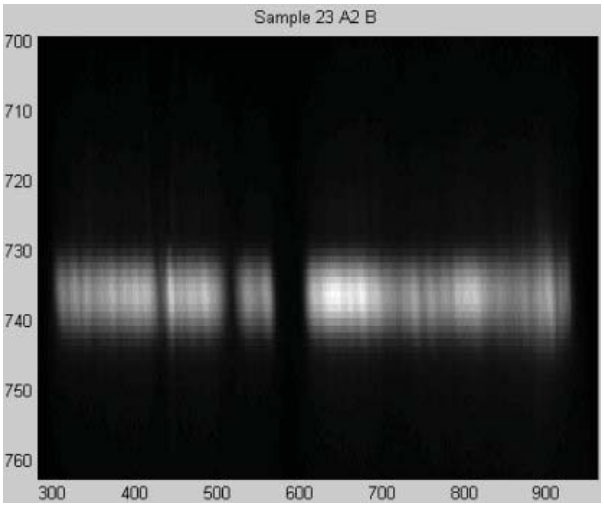


*Fig. 8. Example of measured laser spatial near-field intensity*

We can see from Fig. 8 that the laser near-field intensity distribution is clearly multi-mode and not continuous top-hat Gaussian as used in the initial simulations. There is a black region at the laser facet hitting just in the fiber core in butt coupling with zero alignment tolerances. This causes a clear reduction in coupling efficiency. In the opposite case coupling efficiency would be higher than nominally possible with continuous top hat Gaussian laser. A more accurate laser model is needed in order to achieve truly predictive simulations.

## VI. CONCLUSION

Manufactured module serie coupling efficiency has been pre-studied through simulations performing tolerance analysis in two steps. Sensitivity analysis informed that the most significant variable in optical coupling was fiber decenter along the Y-axis. Monte-Carlo tolerancing revealed the expected performance distribution with the presumable manufacturing tolerances and showed quite narrow performance distribution. The measured alignment tolerance values between laser and fiber were in AT prototype series were $\Delta x$=7.7 µm, $\Delta y$=7.6 µm and $\Delta z$=10.8 µm (SD values). The corresponding values in A2 prototype series were $\Delta x$=3.1 µm, $\Delta y$=9.1 µm and $\Delta z$=10.2 µm. The measured average coupling efficiency was 0.28 in AT series and 0.31 in A2 series. The coupling efficiencies of all operational prototypes varied from 0.05 to 0.43. The characterizations showed that the achieved alignment tolerances are adequate for high efficiency coupling between the used multimode laser and fiber and narrow performance distribution should be achieved. The performance distribution of the modules, however, was clearly wider than the simulations suggested, although the amount of modules was too small for defining the performance distribution accurately. The measured spatial near-field intensity distributions of lasers suggested that the large variations between individual lasers actually cause the widening of module performance distribution. A more accurate laser model is needed in order to improve the accuracy of performance distribution simulation.

## REFERENCES

[1] T. Koch and U. Koren, “Semiconductor photonic integrated circuits,” IEEE J. of Quantum Electron., vol 27, pp. 641-653, Mar. 1991.

[2] R. Kaiser, M. Hamacher, H. Heidrich, P. Albrecht, W. Ebert, R. Gibis, H. Kunzel, R. Löffler, S. Malchow, M. Möhrle, W. Rehbein and H. Schroeter-Jansen, “Monolithically integrated Transceivers on InP: The development nad generic integration concept and its technological challenges,” in 10th Intern. conf. of Indium Phosphide and related materials, May 1998, pp. 431-434.

[3] C. Armiento, M. Tabasky, C. Jagannath, T. Fitzgerald, C. Shieh, V. Barry, M Rothmann, A .Negri, P. Haugsjaa and H. Lockwood, “Passive coupling of InGaAsP/InP laser array and singlemode fibres using silicon waferrboard”, Electronics Letters, vol 27, pp. 1109-1110, June 1991.

[4] S. Mino, K. Yoshino, Y. Yamada, T. Terui, M. Yasu and K. Moriwaki, “Planar lightwave circuit platform with coplanar waveguide for opto-electronic hybrid-integration” J. of Lightwave Tech., vol 13, pp.2320-2326, Dec. 1995.

[5] T. Hashimoto, Y. Nakasuga, Y. Yamada, H. Terui, M Yanagisawa, K. Moriwaki, Y. Susaki, Y. Tohmori, Y. Sakai and H. Okamoto, “Hybrid-integration of spot-size converted laser diode on planar lightwave circuit platform by passive alignment technique”, IEEE Photon.. Tech. Lett., vol 8, pp. 1504- 1506, Nov. 1996.

[6] W. Pittroff, G. Erbert, G. Beister, F. Bugge, A. Klein, A Knauer, J, Maege, P. Ressel, J. Sebastian, R. Staske and G. Traenkle, “Mounting of high power laser diodes on boron nitride heat sinks using optimized Au/Sn metallurgy,” in Proc. of ECTC conf., May 2000, pp. 119-124.

[7] W. Hunziker, W. Vogt, H. Melchior, P. Buchmann and P. Vettiger, “Passive self-aligned low-cost packaging of semiconductor laser arrays on Si motherboard,” IEEE Photon. Tech. Lett., vol 7, pp.1324-1326, Nov. 1995.

[8] J. Goodrich, “A silicon optical bench for approach to low-cost high speed tranceivers,” in Proc. of ECTC conf., May-June 2001., pp. 238-241.

[9] C. Malek and V. Saile,” Applications of LIGA technology to precision manufacturing of high-aspect-ratio micro-components and systems: a review,” Microelectronics Journal, vol 24, pp. 131-143, 2004.

[10] E. Rich, A. Martin, T. Lengel, J. Stewart and S. Gallo, “Low temperature co-fired glass ceramic high density interconnect substrate with improved thermal management”, IEEE Trans. on Comp., Hybr. and Manufact. Tech.., vol 13, pp.639-646, Dec. 1990.

[11] R. Keyssean, J. Sosnowski, M. Doyle, D. Amey and S. Horowitz, “A new approach to opto-electronic/MEMS packaging”, in Proc. of ECTC conf., May 2002, pp. 259-262.

[12] K. Kautio, “Properties of High Definition Photoimaged Conductors in LTCC”, in Proc. of the IMAPS Nordic Conf., Sept.-Oct.2002, pp 227-232.

Jyrki Ollila
*Jyrki.Ollila@vtt.fi*

Kimmo Keränen
*Kimmo.Keranen@vtt.fi*

Jarno Petäjä
*Jarno.Petaja@vtt.fi*

Jukka-Tapani Mäkinen
*Jukka-Tapani.Makinen@vtt.fi*

Veli Heikkinen
*Veli.Heikkinen@vtt.fi*

Kari Kautio
*Kari.Kautio@vtt.fi*

Pentti Karioja
*Pentti.Karioja@vtt.fi*

# Tunable Laser Module for Fibre Optic Communications

## 1 INTRODUCTION

Wavelength-tunable laser diodes [1] are advantageous in optical networks, such as wavelength division multiplexing (WDM) systems [2], where they can save money by simplifying the spare part inventory while making optical networks more flexible [3], [4]. In WDM applications, the tunable sources need to be assembled in a compact and reliable package and possess superior spectral purity, excellent wavelength stability, high output power, and wide tuning range.

Because compact and robust sources with simple handling are preferred, tunable lasers that can be produced as monolithically integrated devices are favoured. Three types of monolithic devices exist, namely, distributed feedback (DFB), distributed Bragg reflector (DBR), and vertical cavity surface emitting lasers (VCSEL). Although these devices have developed rapidly in recent years, they still have some weaknesses - such as the narrow tuning range of the DFB lasers and the low output power of the DBR and vertical cavity lasers.

Hybrid integration of tunable lasers makes it possible to use standard laser chips at potentially low cost. Lasers with a long external cavity produce high output power, have narrow line width, and are tunable over the gain spectrum of the active material. The combination of a movable external reflector and an edge-emitting Fabry-Perot laser diode in a short external cavity configuration allows the realisation of miniaturised tunable lasers.

Reliable, reproducible and high-yield packaging technologies are crucial for meeting the price and performance objectives set for the low-cost photonic modules that are used, for example, in optical access networks. Photonic modules consist of optical, electrical and mechanical parts with different packaging levels, including glass elements, passive and active chip components, submounts and packaged components. Typically, device alignment and attachment is critical. Therefore, for cost-effective packaging, the alignment should be achieved passively using precision-machined parts and material systems that will fulfil the demanding dimensional stability requirement of the assembly. The use of ceramic substrates with integrated alignment structures is one way to implement low cost passive assembly.

Here we present the use of multilayer ceramic substrates as a wiring board and mounting structure when packaging wavelength-tunable fibre-coupled laser modules. The substrates with precision cavities make it possible to passively assemble most of the photonic components so that active alignment is only used in the attachment of the single-mode fibre.

## 2 PRINCIPLE OF OPERATION

The tunable laser system schematically shown in Figure 1 consists of an edge-emitting laser diode (LD), an electrostatically tunable Fabry-Perot interferometer (FPI) device, and a single-mode optical fibre. The FPI is brought within close proximity of the low-reflectance laser facet, whereas the fibre is butt-coupled to the high-reflectance laser surface.

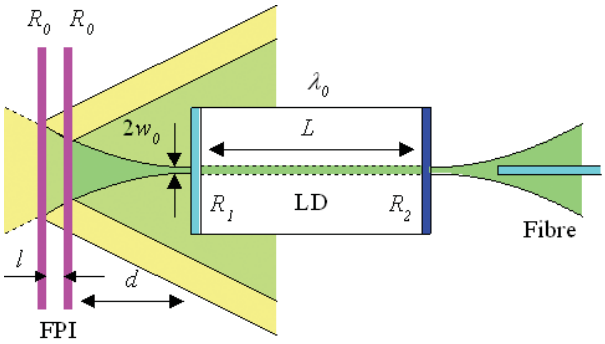


*Figure 1. Schematic of the FPI-tuned laser.*

The surface micromachined FPI device consists of movable top and stationary bottom mirrors [5]. By applying voltage between the mirrors, the top mirror is moved toward the bottom mirror and the spectral transmission band of the FPI is tuned to shorter wavelengths. Laser tuning mechanisms are explained in [5].

## 3 MODULE PACKAGING

Figure 2 shows the functional model of the tunable laser. The module packaging is based on the use of precision ceramic substrates. Low temperature co-fired ceramic (LTCC) technology is an extension of thick film technology, using the conventional screen printing technique for conductor patterning on unfired glass-ceramic tape sheets, which are further laminated and co-fired to make a high-density multilayer structure.

Low conductor resistance, low dielectric loss and the ability to integrate passive electrical components (resistors, capacitors, and inductors) into the substrate make LTCC a useful technology for telecommunication applications. The multilayer structure and fine-line capability allow the realisation of complex substrates with three-dimensional electrical interconnects and offer the possibility to miniaturise electronic and optoelectronic products.

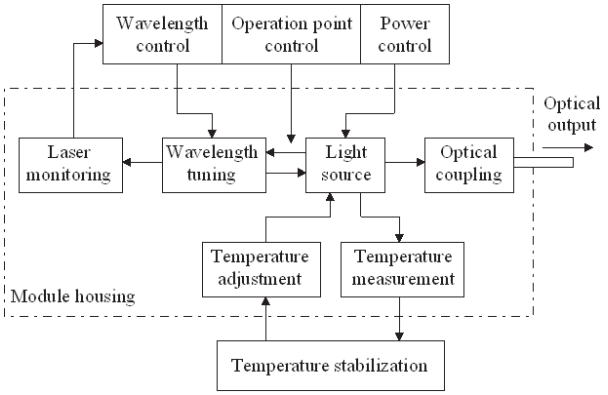


*Figure 2. Functional model of the module.*

The possibility to form stable three-dimensional structures, such as cavities, holes and channels, and the compatibility with hermetic sealing, are very useful for optopackaging. In addition, the fair match of the thermal expansion coefficient to optoelectronic chips reduces packaging-induced thermomechanical stresses. Today, electronic LTCC modules are employed in automotive and telecommunication applications such as Bluetooth and mobile phone modules, but they have been little used in optoelectronic applications.

The base plate manufactured using the LTCC process serves as the mounting platform for the subassemblies and as the wiring board for the electrical connections inside the module, Figure 3. Photodiodes, the monitoring subassembly and the FPI chip, use LTCC substrates, whereas other mechanical parts are made from aluminium alloy.

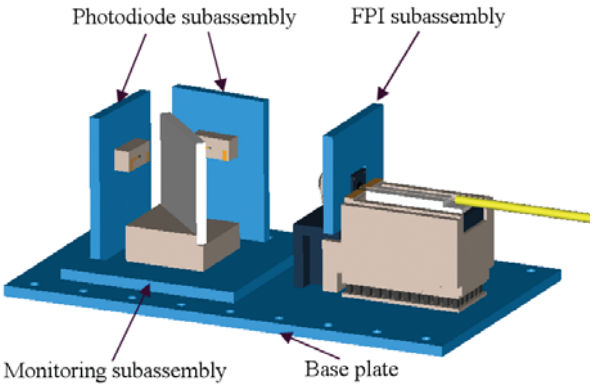


*Figure 3. Schematic assembly of the module.*

The LTCC substrates contain precision cavities that help in the positioning of the components. In an accurately controlled process, the dimensions of fairly large cavities, such as those used in our module substrates, possess a horizontal and vertical inaccuracy of ± 20 µm and ± 10 µm, respectively. When the substrates are diced by sawing, the LTCC part dimensions have a lateral inaccuracy of ± 10 µm. The perpendicularity error of the sawn surfaces to the other surfaces is under ± 0.5°.

The thermoelectric cooler attached to the LTCC base plate stabilises the temperature of the laser and the laser-to-fibre coupling optomechanics. This minimises the component misalignments caused by varying ambient temperature. The laser chip lies on an aluminium nitride substrate that has high thermal conductivity. The thermistor is placed near the laser to monitor its temperature.

The FPI attached to the LTCC substrate stands near the low reflectance laser facet. A piezoelectric actuator fine-tunes the separation between the FPI and laser. The cavities of the LTCC substrates serve as reference marks during the assembly and also enable passive alignment of the FPI chip and the monitor lens. Because FPI devices are sensitive to stress-induced degradation, low-stress die-attach techniques are necessary.

The monitor lens collimates the divergent laser beam transmitted through the FPI and directs it to the laser-monitoring subassembly. This consists of a wavelength-selective beam splitter and two photodiodes. The high-reflectance facet laser beam is butt coupled to the output fibre. Figure 4 shows the realised module before the fibre feed-through and the cover was assembled.

*Figure 4. Tunable laser module before the fibre feed-through and cover was assembled.*

## 4 MODULE PERFORMANCE

The tunable laser is able to produce either a multimode or single-mode output spectrum depending on the control parameters. When simultaneously optimising both the

piezo and the FPI control voltages we obtained a 13-nm single-mode tuning range, Figure 5.

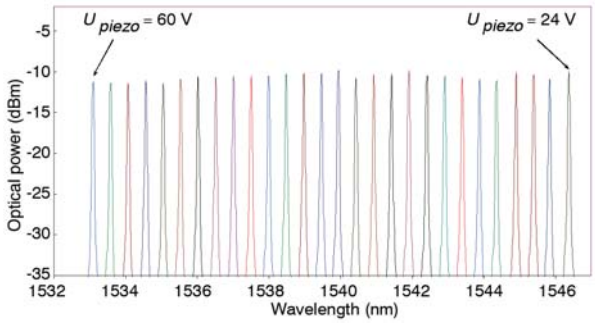


*Figure 5. Superimposed spectra in the single-mode tuning.*

The output spectrum consisted of the principal mode and relatively weak side modes. The side mode suppression ratio was better than 25 dB and the single-mode fibre-coupled output power 100 µW [5]. In multimode operation, the maximum wavelength tuning range was 19 nm and fibre-coupled output power 0.7 mW.

One advantage of the short external cavity configuration is the possibility to modulate the output power by laser current. The measured 3 dB cut-off frequency of 600 MHz is the widest reported direct modulation bandwidth of the external cavity tunable laser [6].

In conclusion, we realised a prototype series of 1550 nm-band FPI-tuned external cavity laser modules that used LTCC substrates. The precision cavities of the LTCC parts eased the module assembly by enabling the passive alignment of the photonic components. The hybrid arrangement used standard laser chips and thus provides a potentially cost-effective and easily configurable solution for last-mile fibre optic communications.

## REFERENCES

1 M.-C. Amann and J. Buus, “Tunable laser diodes,” Norwood, MA: Artech House, 1998.

2 J.-P. Laude, “DWDM fundamentals, components, and applications,” Norwood, MA: Artech House, 2002.

3 E. Bruce, “Tunable lasers,” IEEE Spectrum, Vol. 39, pp. 35–39, Feb. 2002.

4 T. Day, C. Thompson, and J. Lee, “Widely tunable laser technologies: meeting the need of tomorrow’s networks,” in Proc. SPIE, vol. 4652, 2002, pp. 186–196.

5 V. Heikkinen, J. Aikio, T. Alajoki, J. Hiltunen, A-J. Mattila, J. Ollila, P. Karioja, “Single-mode tuning of a 1540-nm diode laser using a Fabry Pérot interferometer,” IEEE Photonics Technology Letters, Vol. 16, pp. 1164–1166, Apr. 2004.

6 V. Heikkinen, J. Ollila, T. Rantanen, K. Vanhatalo, P. Karioja, “600 MHz direct modulation of short external cavity wavelength-tunable diode laser,” Electronics Letters, Vol. 40, pp. 871–872, July 2004.

Veli Heikkinen
*Veli.Heikkinen@vtt.fi*

Kari Kautio
*Kari.Kautio@vtt.fi*

Janne Aikio
*Janne.Aikio@vtt.fi*

Teemu Alajoki
*Teemu.Alajoki@vtt.fi*

Jyrki Ollila
*Jyrki.Ollila@vtt.fi*

Pentti Karioja
*Pentti.Karioja@vtt.fi*

# Spectral Radiant Flux Measurements for Infrared Light Emitting Diodes and Halogen Lamps

## 1 INTRODUCTION

Light emitting diodes (LEDs) and arrays may be used as radiation sources for optical instruments and spectrometers. A majority of LED applications to date have been in high volume consumer products, such as car and instrument indicators, displays, car brake lights, transmitters for optical telecommunications and even room illumination. The availability of LED wavelengths reflects this market demand, in which case most standard devices emit at visible wavelengths, with only a few wavelengths available for UV and infrared applications. Recently, the situation has improved, and LEDs for instrumentation applications at intermediate and extended wavelengths have become available. The Hungarian MFA institute has developed a set of LEDs covering wavelengths from 1000 to 1700 nm [1], which are packaged and offered for instrumentation applications by VTT's spin-off company Rikola Ltd [2]. Furthermore, The Ioffe institute in St.Petersburg has an extensive background in even longer wavelength LEDs, such as those for 1940nm [3] and for mid infrared wavelengths of up to about 7000nm [4].

Radiometric measurements were arranged for the selected infrared LEDs and typical halogen incandescent lamps during the VTT-funded research project "Optical Techniques for On-line Instrumentation". The light emitting diodes and halogen lamps, chosen for the study, are components with potential to serve as light sources in near infrared instrumentation. The goal of the measurements was to study the spectral radiant flux emitted into the hemisphere at near infrared wavelengths. This report provides a summary of the measurements made as well as discusses the results obtained.

## 2 EXPERIMENTAL

The LED and lamp devices chosen for the study are summarised in Table 1.

The setup for the measurements is illustrated in Figures 1 and 2. An integrating sphere with diffuse gold coating (Labsphere IS-010-IG) was used to collect radiation from the LED or lamp under study. A small sized sphere was used, with a diameter of 1 inch, in order to minimise optical losses and obtain acceptable signal-to-noise characteristics. The light source under study was brought as close as possible to an input port, with a diameter of 6.15 mm, aiming to practically collect the whole beam emitted by the source into the hemisphere. For all LEDs this was not possible, in which case a small gap, in the order of 1 mm was present between the LED and the input port. The tested lamps were equipped with an ellipsoid reflector, in which case the focal spot was aligned with the input port of the sphere. Radiation from the integrating sphere was transmitted by fibre optics into a FTIR spectrometer (Bomem MB 155) to record the spectral response. A low OH quartz fibre bundle was used for the LED measurements. For lamp measurements there was interest to obtain results reaching longer wavelengths, in which case infrared fibre optics of fluoride material was used instead (La Verre Fluore IRguide-1). Furthermore, different detector and preamplifier units were also mounted for LED and lamp measurements. Extended InGaAs photodiode (Hamamatsu G5853-11) was used for LED measurements and a PbS photoconductor for lamp measurements, accordingly. The spectral response for the equipment was calibrated by recording spectra from a blackbody source (Electro-Optical Industries, Control unit 215B, Radiator unit WS143), and repeating the calibration for each LED or lamp experiment. The blackbody temperatures used were 1058K and 1283K for LED and lamp measurements, correspondingly. The blackbody aperture diameter and the distance from the sphere were adjusted and observed, for use in the calibration formula.

| Type | Manufacturer | Wavelength [nm] | Measuring conditions | Quantity [pcs] |
|---|---|---|---|---|
| Custom device with 3 LED chips | Rikola | 1280<br>1490<br>1580 | 40 mA dc | 1 |
| LED 1.2 | Physimpex | 1200 | 40 mA dc | 3 |
| LED 1.3 | Physimpex | 1300 | 40 mA dc | 3 |
| LED 1.4 | Physimpex | 1400 | 40 mA dc | 2 |
| LED 1.9 | Physimpex | 1940 | 40 mA dc | 2 |
| 8211-09 (20W) | Welch Allyn | | 90 % of nominal voltage | 1 |
| L6408-G (75W) | Gilway | | 90 % of nominal voltage | 1 |

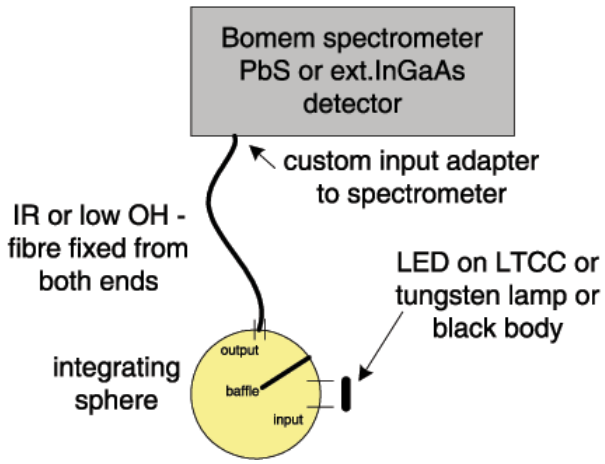


*Figure 1. Schematic diagram of measuring equipment.*

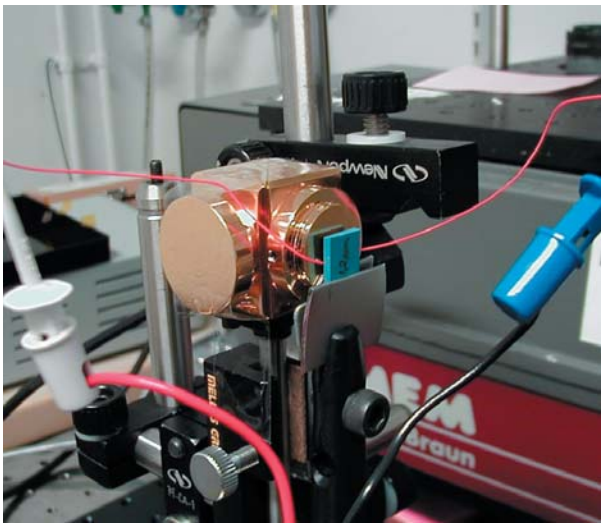

*Figure 2. Illustration of an LED device facing the input port of the integrating sphere.*

Spectral radiant flux $\Phi_\lambda$ for each lamp and LED was estimated using the following mathematics,

$$\Phi_\lambda = K_\lambda \times S_\lambda \quad (1)$$

$$K_\lambda = \frac{L_\lambda A_i \Omega_{bb}}{S_{bb,\lambda}} \quad (2)$$

$$L_\lambda = \frac{2hc^2}{\lambda^5 \left(e^{\frac{hc}{\lambda kT}} - 1\right)} \quad (3)$$

where

$K_\lambda$ = calibration vector
$S_\lambda$ = response spectrum
$L_\lambda$ = blackbody radiance
$A_i$ = area of input port
$\Omega_{bb}$ = solid angle of blackbody illumination
$S_{bb,\lambda}$ = response spectrum for blackbody measurement
$T$ = blackbody temperature.

## 3 RESULTS

Results for all tested LEDs and halogen lamps, calculated to spectral radiant flux [W $\mu$m$^{-1}$], are shown in figure 3 for comparison purposes. The spectral flux of the halogen lamps can be seen as being much higher than that of any of the tested LEDs, for the whole wavelength range. This will be true when operating LEDs using small direct current activation, likewise the current measurements (40mA). It is known that the peak output from LEDs may be significantly increased using high drive currents in pulsed, low duty cycle operation [5]. According to product information from Rikola Ltd [2], the improvement possibility for their device, with optimum pulsing conditions, will be by approximately the factor of 20. Therefore, the situation will be more favourable for LEDs in pulsed operation.

It is worth remembering, that the tested lamps were special halogen lamps with fitted ellipsoid reflectors for infrared applications. The spectral flux obtained here is not the total flux from the lamp, but corresponds to the flux delivered to an aperture with diameter of 6.15 mm, located at the focal point of the reflector. The result was measured using 90% of nominal voltage, which is common practice in instrument applications to extend the operating life of halogen lamps.

## 4 CONCLUSIONS

The results obtained in the current study may be useful for radiometric power budget calculations in the development of near infrared instrumentation.

For future research it will be useful to continue studies to 1) evaluate LEDs and lamps in pulsed operation, and 2) examine spectral radiance on the emitter surface, available from LEDs and thermal sources. Information about radiance will be useful for estimating coupling efficiency of optical fibre, which is of interest for many applications.

## REFERENCES

1. V. Rakovics et al, Spectral characteristics of InGaAsP /InP infrared emitting diodes grown by LPE, Materials Science and Engineering B91-92 (2002) pp. 491-494.

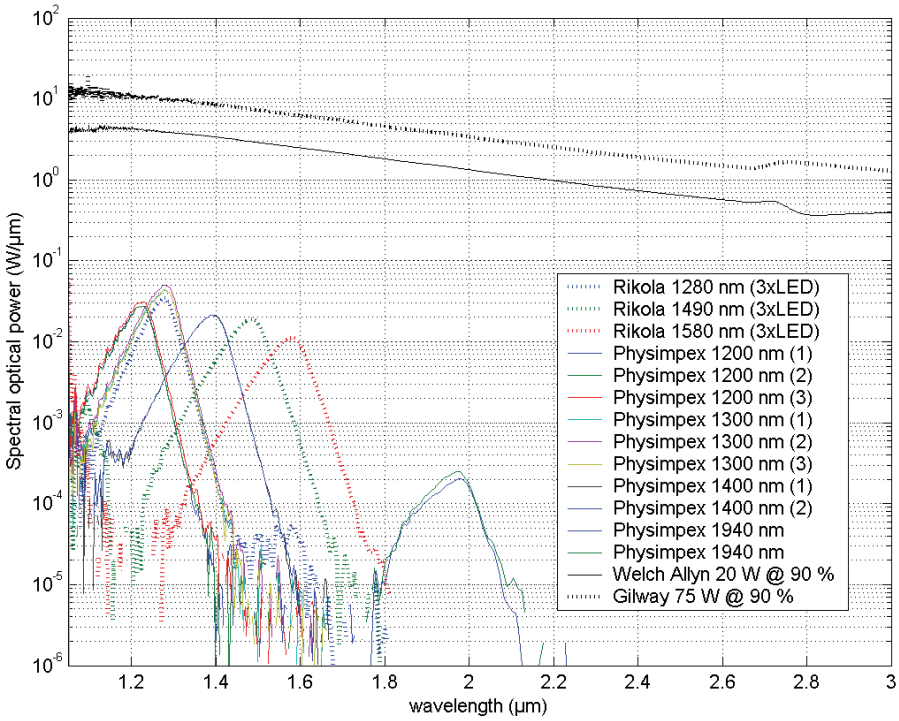


*Figure 3. Results of the study presented as calibrated spectral radiant flux for tested LEDs and halogen lamps.*


2. Rikola Ltd Oy. Spectro LEDs, product information. URL: http://www.rikola.fi/
3. T.N. Danilova et al, High-power light-emitting diodes operating in the 1.9 to 2.1- um spectral range. Semiconductors Vol 33 No 2, (1999).
4. Mid-IR Diode Optopair Group, Ioffe Physico-Technical Institute. URL: http://www.mirdog.spb.ru/index.htm
5. P. Chambers et al, Investigation of the peak power enhancement available from a surface emitting GaAlAs near-infrared light emitting diode by cooling and pulsing. Meas. Sci. and Technol. 14 (2003) pp. 2006-2014.


Jouko Malinen
*Jouko.Malinen@vtt.fi*

Hannu Lindström
*Hannu.Lindstrom@vtt.fi*

# Printable Optics and Electronics: A Short Summary from the Printo-project 2002-2004


## ABSTRACT

The embedding of electrical, optical and optoelectronic functionalities into low-end products like packages and printed matter can be used for the realisation of active and intelligent packages and printed matter. These functionalities can be used to produce simple entertaining and impressive effects or they can be integrated into the package in order to help logistics, monitor the quality of the product, and even to produce interactive packages. For these purposes, components like displays, photodetectors, light sources, solar cells, battery elements, diffractive optical elements, light guides, electrical conductors, resistors, transistors, switching elements, etc., and their integration techniques to create functional modules are required. Additionally, the price of the integrated components and modules cannot considerably increase the price of the product package or printed matter.


## INTRODUCTION

Conventional and advanced printing methods are well established techniques and are nowadays routine tools for the packaging and printed matter industry. From the packaging and printing industry point of view, the roll-to-roll (R2R) technique is the only method of choice capable of fulfilling the demanded production volume and integration of the existing production process with a low cost level. Moreover, conventional printing techniques are additive techniques reducing the amount of waste during the fabrication. When simple electrical and optical components can be fabricated using conventional printing techniques, their integration into the low-end products will be possible.

'Printable optics and electronics' –project (PRINTO) has been one of the biggest research projects in the 'Electronics miniaturisation programme' (ELMO) of the National Technology Agency (TEKES) in Finland. PRINTO has been a consortia project of 7 research groups from the Technical Research Centre of Finland (VTT) and Finnish Universities and 7 industrial partners from the paper and pulp, printing and electronics industries. PRINTO has focussed on the continuous R2R fabrication of active and passive optical, electronic and optoelectronic components and circuits on web (paper or plastic). R2R fabrication enables the volume-scale and cost-effective fabrication of printed electronics, and its integration into tomorrow's low-end products such as product packages, printed matter, disposable sensors and low-end electronic products.

VTT Electronics was the coordinator of the Printo-project. VTT Electronics' main research areas in this project were optical light guides, organic light emitting diodes (OLED), organic solar cells (OSC) and the R2R fabrication of passive electronic components and diffractive optics including optical read-only memories and decorative elements. VTT Information Technology's microelectronics group investigated components and demonstrators based on the conductive polymers. Investigation of the ink-jet printing for the individualisation of the active packages was carried out by the VTT Information Technology's media group. The University of Joensuu designed diffractive optical elements and also fabricated the required tools for the R2R fabrication of these elements. Printable dye-sensitised solar cells were investigated at the University of Jyväskylä, Department of Chemistry, and passive electronic components based on particulate conductors at the University of Oulu, Microelectronics Laboratory. Functional demonstrator concepts, showing the capability of these techniques in terms of active and intelligent package, have been designed according to consumer interests. Research work was carried out by the University of Lapland, Faculty of Arts and Design. From the designed concepts, the most suitable ones were chosen for demonstrators' realisation

## TECHNIQUES

During the Printo-project, conventional roll-to-roll printing technologies such as gravure-, off-set-, ink-jet, hot-embossing, and flexographic printing were evaluated for the fabrication of electrical, optical and optoelectronic components. From those techniques, most of the attention was paid to the gravure printing of passive and active electrical, optical and optoelectrical components, whereas diffractive optics have been produced using the roll-to-roll hot-embossing technique. Some efforts were also


*Figure 1. Tabletop gravure printability tester for material modification and first printing trials.*

paid to the flexographic-, off-set-, and screen-printing techniques in order to obtain an understanding of the technological benefits and drawbacks of the different printing techniques, and also for the ink-jet printing of the individualisation of the packages and printed matter.

The first printing trials, as well as the material modification, were carried out using table scale printing machines, see Figure 1. For the pilot production trials, VTT Electronics' PICO facility was used. This facility includes two gravure (UV-, thermal- or IR-curing possibilities), hot-embossing and laminating units. The facility is capable of printing max. 25 cm width web at the speed of max 100 m/min and is shown in Figure 2.

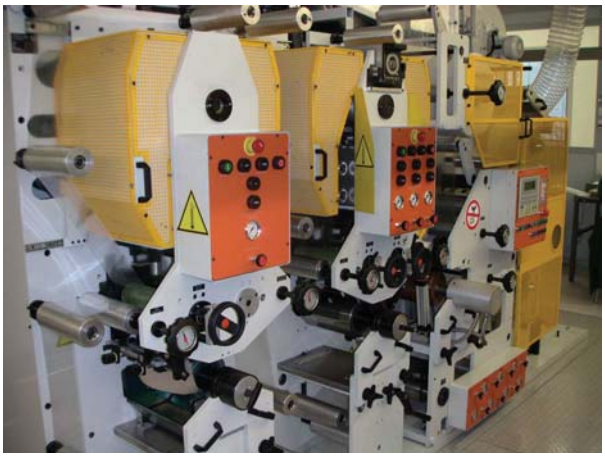

*Figure 2. PICO pilot production facility installed in VTT Electronics' clean room environment.*

## REALISATION OF LIGHT AND POWER SOURCES USING OPTOELECTRONIC COMPONENTS

From the active package point of view, the most critical component is the display element. During the Printo-project, R2R manufacturing technologies for the organic light emitting diodes (OLED) using the gravure printing of organic layers on commercial ITO-PET substrate was investigated. The R2R fabrication of OLED was started by the gravure printing of modified PEDOT-PSS ink, which enhances the performance of the final device. On top of the PEDOT-PSS layer, emitting polymers such as MEH-PPV (orange) and PFO (blue), or small molecules doped in a suitable host were also printed by using the gravure technique. For the fabrication of cathode, the evaporation (Mg-Al) technique was used, even though screen-printed cathodes (Ag) have also been successfully used. In Figure 3, printed blue-orange OLED behaving as a "temperature indicator" in a medicine package is shown.

*Figure 3. OLED (blue and orange) -based temperature indicator on active package.*

Emitting devices also require energy. For the Printo-project, dye-sensitised or organic solar cells (DSSC and OSC, respectively) were chosen as the energy source.

The conventional fabrication method of the DSSC cells requires high temperatures and long processing steps, which are not suitable during R2R fabrication. These steps include the high temperature fabrication of nano-crystalline TiO2 on ITO-coated substrate, dye-sensitisation of the TiO2-layer, and the encapsulation of liquid electrolyte between sensitised TiO2-layer and platinised (vacuum process) counter electrode. During the Printo-project, DSSC fabrication techniques suitable for R2R manufacturing were investigated and developed: 1) the fabrication of nano-crystalline TiO2 can be achieved using different R2R suitable coating methods and R2R calandering, 2) liquid phase electrolyte can be converted with gel electrolyte, and 3) counter electrode can be fabricated with the gravure technique using pre-platinised, gravure printable materials, such as ATO. With these, R2R capable technique cells with solar conversion efficiency of 3.2% (1/10 suns) has been achieved.

The device structure of the organic solar cell (OSC) is very similar to OLED; only the materials are different. For the R2R fabrication of OSC inks containing P3HT and fullerene, the blend was gravure printed on commercial ITO-PET. Evaporated Al was used as a cathode. With these structures, a relative solar conversion efficiency of 0.1% was achieved.

## ELECTRICAL MATERIALS AND COMPONENTS

For the realisation of active and intelligent packages, simple electrical components such as resistors and conductors are required. For these purposes, the fabrication of such components using conductive polymers and particulate inks were used.

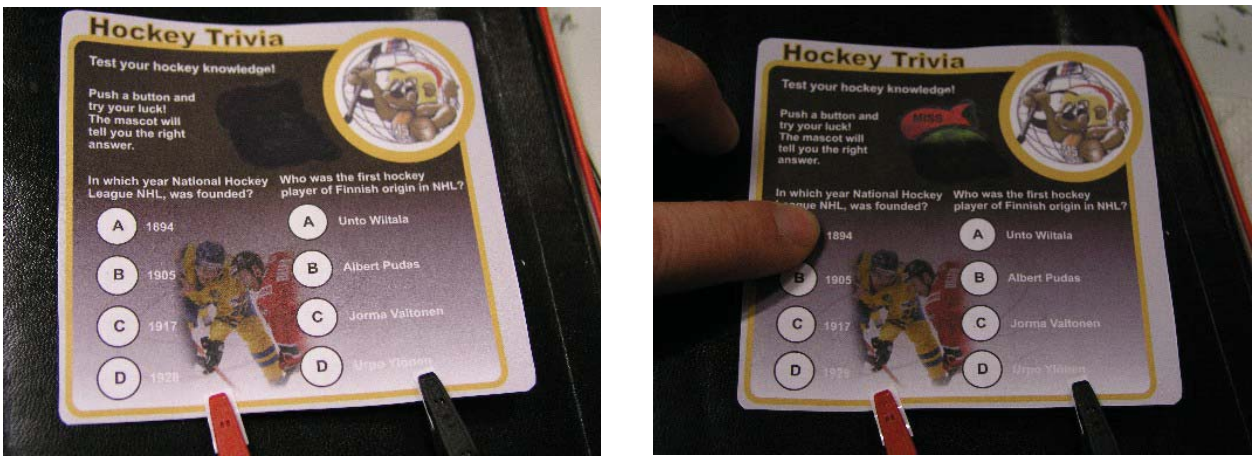


*Figure 4. The appearance of the ice-hockey demonstrator operating with 5 volts. (Tapio Mäkelä VTT TTE/microelectronics).*

The high speed roll-to-roll manufacturing process of polyaniline (PANI) and polytiophene (PEDOT-PSS) patterns directly onto paper have already been demonstrated with table-top and pilot machines. VTT Information technology's microelectronics group has investigated the possibilities of modifying polyaniline materials to be suitable for flexo and gravure printing methods. As a result, conductivity, spreading, optical quality and thickness can be controlled. This can be used for the realisation of both passive and active circuit components e.g. resistors, capacitors, diodes and even the parts of the transistors using roll-to-roll techniques. In Figure 4, a thermochromic display element is used for the realisation of a simple hockey trivia game. For the realisation of the demonstrator, thermochromic ink was printed using flexographic printing. Conducting materials, which behave as a heating element, were processed on the other side of the paper. When the operating voltage was 5 volts, the colour change took less than 3 seconds.

The main advantage of particulate conductors over polymeric conductors is their higher conductivity levels in comparison to polymeric conductors. The conductivity level of a typical silver-based particulate conductor material suitable for printing purposes is in the scale of 103 S/cm.

By using commercially available silver-based conductive inks, gravure printed test structures have been realised by the "PICO" pilot production facility on paper and plastic substrates as shown in Figure 5. Obtained sheet resistance was 200 mΩ/sq on plastic. The sheet resistance of the corresponding structures on paper was a little higher but still below 1 Ω/sq. The lower conductivity level of paper is a result of the porosity of the paper reducing the amount of the contacts between the silver particles with the same amount of ink.

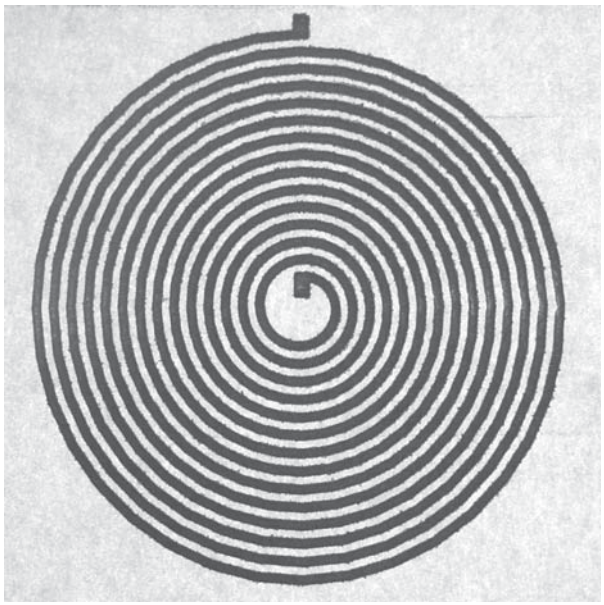

*Figure 5. Gravure printed coil-antenna test structure (Marko Pudas, University of Oulu).*

## DIFFRACTIVE OPTICS AND LIGHT GUIDED FOR DECORATION AND OPTICAL DATA STORAGE

Different type of optical elements can be used in packages to produce different types of entertaining or impressive effects. In some cases, the information content of the packages can be also increased by using properly designed and fabricated optical elements. During the Printo-project, we have investigated the roll-to-roll fabrication of optical light guides and diffractive optical elements in order to utilise the potential of optics in active and intelligent packages.

In packages, light guides can be used for decorative purposes. In such cases, light from the integrated light source can be coupled into the light guide, which delivers light to the destination area of the package where it can be coupled out with the desired shape producing shining figures. Three different types of approach to the fabrication of light guides were used: combined technique where embossed grooves on substrate are fulfilled with optical core material, and direct write using gravure or ink-jet techniques. The best results were obtained using the gravure printing technique. In Figure 6, Veeco picture from the optical light guide and light propagation in the light guide can be seen. The minimum optical attenuation obtained so far is 1.8 dB/cm.

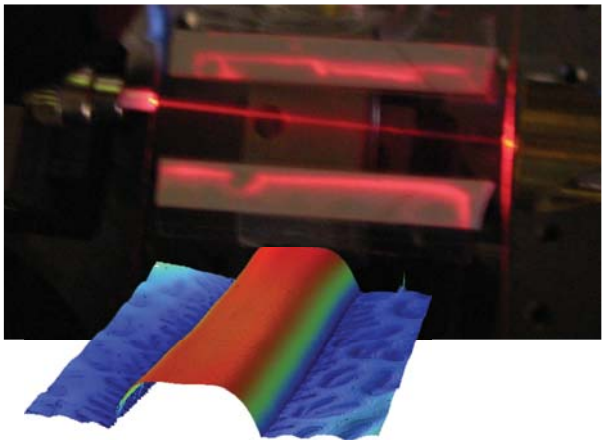

*Figure 6. Gravure printed optical light guide.*

Diffractive optics are based on microstructured surfaces and can be used to realise optical functions that are exceedingly difficult or expensive to achieve by conventional optics. Sometimes a single diffractive element can replace a complicated refractive system. Nowadays there are number of effective methods for mass producing diffractive optics. Roll-to-roll embossing is one of the most suitable techniques for that purpose and it is already widely used for security purposes.

In this project, several types of diffractive optical elements and microstructures for decorative and informative purposes have been realised and demonstrated by using the roll-to-roll hot-embossing technique with the pilot production facility. The designing of such multi-informative elements requires novel types of design methods and equipment that make this technique suitable also for security applications. As an example from the fabricated structures, Figure 7 shows a decorative and informative element, namely kinegram, producing different kinds of visual information depending on the viewing angle. In such a role, the same amount of information in three languages can be integrated into the area required by only one language. Different languages become visible when looking at the element from different angles. R2R fabrication of kinegrams using the "PICO" pilot production facility was realised during the Printo-project.


*Figure 7. Three images of kinegram (Tomi Haring, University of Joensuu).*

By using microstructures, it is also possible to generate read-only types of optical memories that are producible by different kinds of embossing techniques. In this project, a read-only optical memory was designed and established. The basic idea of the memory is based on the diffractive microstructure that will produce a data matrix pattern when illuminated by laser. This pattern information can be read and analysed by a mobile terminal in order to decode the pattern containing information. In Figure 8, the principle of optical read-only memory is shown.

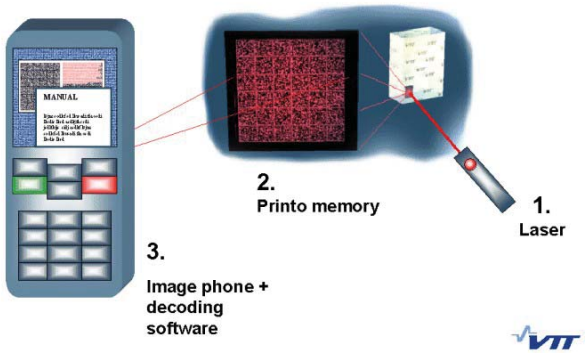


*Figure 8. Principle of read-only memory based on the usage of the diffractive optics.*

When the R2R hot-embossed diffractive element is illuminated with a laser it produces a data matrix pattern containing information in a manner similar to that of a standard bar code but with much higher data density (up to 250 000 bytes/cm$^2$). The pattern is read with a camera phone and the information is decoded. In this concept, the product package can carry a huge capacity of information instead of obtaining the data from the web.

During the Printo-project, transmission and reflection types of optical read-only memories were fabricated using static- and R2R hot-embossing techniques. In Figure 9, an image from a transmission type optical read-only memory can be seen (static hot-embossing was used at the University of Joensuu). The processed data showed an amazing bit-error-ratio (BER) of 0.2%, including the central peak. For R2R fabricated reflection type of optical read-only memories the minimum BER was 1.33 %.

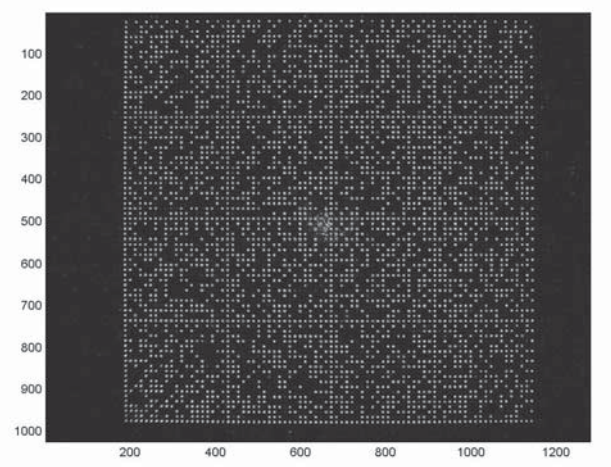


*Figure 9. (Left) Image of the transmission element on CCD camera (static embossing).*

## SUMMARY

Roll-to-roll techniques for the fabrication of simple passive and active electrical, optical and optoelectrical components have been evaluated. By using these methods, it has been possible to fabricate several different types of elements suitable for use in active and intelligent packages. For the realisation of simple electrical components such as conductors, resistors and coils, conductive polymers and particulate conducting materials together with gravure-, flexo-, ink-jet and screen-printing methods have been used. The active optoelectrical components including organic light emitting diodes and solar cells have been fabricated with high-volume capable methods. Diffractive optical elements that can be used for decorative, entertaining and information increasing components have been fabricated with the roll-to-roll hot-embossing technique. The realisation of all of these single components followed by the future integration of them into functional modules will make it possible for the revolution of roll-to-roll manufactured active and intelligent packages.

## ACKNOWLEDGEMENTS

Authors are grateful to National Technology Agency (TEKES) and Printo-project's industrial members (Asperation, Avantone, Electroplast, Hansaprint, Metso, M-real, Ciba (former Raisio-Chemicals) and UPM-Kymmene) for their financial support and enthusiastic contribution to the project. The help from Professors Ghassan Jabbour (Univerity of Arizona, Optical Sciences Centre) and Vivek Subramanian (University of California, Berkeley) are also greatly acknowledged.

Tapio Mäkelä
*VTT Information Technology, microelectronics*
Jali Heilmann
*VTT Information Technology, media*
Tomi Haring
*University of Joensuu, Department of Physics*
Jani Kallioinen
*University of Jyväskylä, Department of Chemistry*
Marko Pudas
*University of Oulu, Microelectronics Laboratory*
Ismo Alakärppä
*University of Lapland, Faculty of Art and Design*

Terho Kololuoma
*Terho.Kololuoma@vtt.fi*

Markus Tuomikoski
*Markus.Tuomikoski@vtt.fi*

Harri Kopola
*Harri.Kopola@vtt.fi*

# Gravure Printed Thin Films for Polymer Leds

## INTRODUCTION

$\pi$-conjugated polymers are very promising and attractive materials for use in electroluminescent displays , photovoltaics, transistors, and sensors, because they combine the optoelectronic properties of semiconductors with the processing advantages and mechanical properties of plastics. Currently, processing and fabrication of thin films for polymeric electronics is carried out using traditional techniques such as spin coating. However, this technique has several disadvantages, e.g. material wastage and time consuming, and therefore, tremendous benefits are gained by incorporating printing technique in the deposition of polymer thin films.

Gravure printing has introduced one of the fast and cost effective roll-to-roll techniques with adequate resolution and low process temperature. In this technique the pattern to be printed is engraved into the rotational printing cylinder. The engraved cells are filled with ink that is transferred to the foil when the cylinder is brought into contact with the surface of foil. During printing excess ink is removed from the cylinder by use of the flexible doctor blade. This ensures that the cells are filled with exact volume of ink. In this study, our interest is to print light-emitting thin films for the flexible polymer light-emitting device (PLED) using semiautomatic table-top size gravure printer. It is known that the electroluminescence performance of the device is highly sensitive to the film morphology. Therefore, the quality of printed film must be flat and uniform without any pinholes.

## EXPERIMENT

The PLED structure studied consisted of ITO/PEDOT/MEH-PPV/Ca/Al. For the hole injection layer the conductive polymer, poly(3,4-ethylenedioxythiophene) doped in poly(styrenesulfonate) (PEDOT:PSS) was spin coated resulting 70-nm thick film onto precleaned poly(ethylene telephtalate) (PET) substrate coated with indium-tin-oxide (ITO, 50 ohms$\cdot$sq$^{-1}$) anode. The film was subsequently dried at 60°C for over night in $N_2$ atmosphere. Poly[2-methoxy-5-(2-ethylhexyloxy)-1,4-phenylenevinylene] (MEH-PPV, Mw ~280'000 g/mol) was utilized as an active luminescent material. The polymer solution was gravure printed at the speed of 1 m/s and followed by drying at 60°C for 2 hours in $N_2$ atmosphere. The Ca/Al cathode was prepared by vacuum evaporation at the base pressure of $10^{-6}$ mbar. The emitting area was 16 mm$^2$. Current density-luminance-voltage measurements were carried out in room ambient condition with epoxy encapsulation.

## RESULTS

The mesh sizes of 70 lines/cm and 40 lines/cm with the 40 µm and 70 µm cell depths were used to gravure print polymer films, respectively. The film morphology is represented using the histogram plot showing the distribution of individual film thickness over 100 mm$^2$ size area, and the surface profile indicating film roughness and waviness from the scan length of 10 mm.

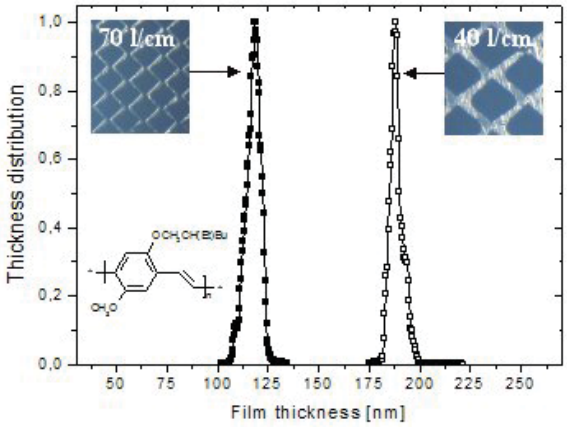


*Figure 1. Film thickness histograms plotted from 100 mm$^2$ size area. Photographs of engravings in 70 l/cm (filled squares) and 40 l/cm (open squares) are represented in insets, and the structure of MEH-PPV polymer is also shown.*

The narrow peaks, which correlate Gaussian function, in the histograms (Figure 1) resulted low film waviness and roughness. It is noticed that increasing the cell depth in the engravings, thicker films can be achieved. Film thicknesses of 117.7 nm and 188.7 nm were obtained with low calculated standard deviation of <4 nm in both films. Figure 2 shows cross sections of printed surfaces. The profiles are being measured along lines (see inset) not showing any significant holes or bumps in the printed film.

Same gravure printed light-emitting films, as above, were used to fabricate separate PLEDs. The current density-luminance-voltage (*I-L-V*) characteristics are shown in Figure 3. Here, the device with thicker polymer layer results three times lower current density at the forward bias of 6V than thinner layer, as predicted.

The turn-on voltage for current injection of the PLED is almost independent of the thickness of the polymer layer. However, the turn-on voltage for light emission is strongly dependent on the thickness of the polymer layer. It can be easily seen in the *L-V* curves (Figure 3, inset), where the turn-on voltage for light emission is shifted from the bias of 3.5 V to 4.2 V.

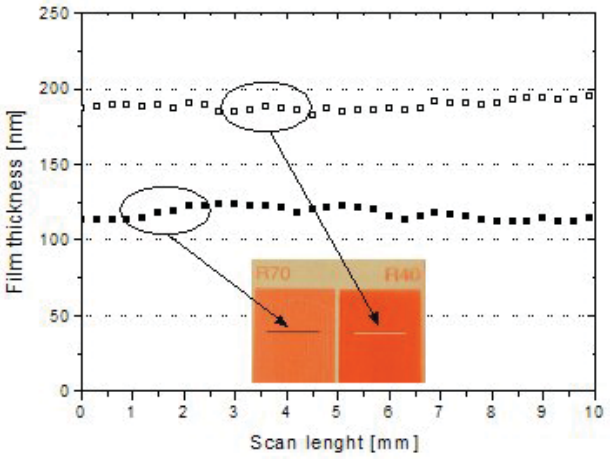


*Figure 2. Surface profiles from the cross section (inset) of two printed films.*

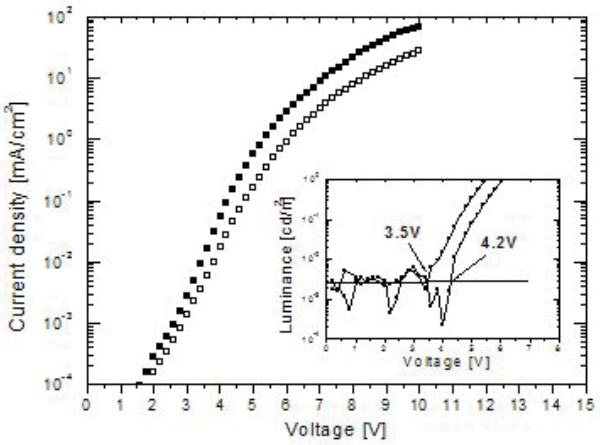


*Figure 3. I-L-V characteristics of printed PLEDs.*

## CONCLUSION

PLEDs based on gravure printed light-emitting polymer film were investigated. The printed films achieved flat uniformity over large area.

## REFERENCES

1. H. Burroughs, D. D. C. Bradley, A. R. Brown, R. N. Marks, K. Mackay, R. H. Friend, P. L. Burns, and A. B. Holmes, Nature (London) 347, 539 (1990).
2. T. Kololuoma, M. Tuomikoski, T. Mäkelä, J. Heilmann, T. Haring, J. Kallioinen, J. Hagberg, I. Kettunen, and H. Kopola, Proceedings of SPIE, 5363 Emerging Optoelectronic Applications, (2004) pp.77-85.
3. M. Tuomikoski, G. E. Jabbour, T. Kololuoma, and H. Kopola, Proceedings of Optics Days 2004, (2004), 67.

Markus Tuomikoski
*Markus.Tuomikoski@vtt.fi*

Arto Maaninen
*Arto.Maaninen@vtt.fi*

Kaisa-Leena Mäkelä
*Kaisa-Leena.Makela@vtt.fi*

Marja Välimäki
*Marja.Valimaki@vtt.fi*

# Biocompatible Materials

## 1. INTRODUCTION

BioOulu project enhances co-operation among biotechnology, information technology, electronics, physics and chemistry. The goal is to create new biomolecule detection systems. Our target is to generate biocompatible materials to be used as part of disposable biosensors. In the following summary some results of the foregoing material development are presented.

Mild, aqueous, room temperature reaction conditions during synthesis of sol-gel materials enable them to be used with different biomolecules. Sol-gel bioactive materials obtained by entrapment of proteins, including also whole-cell extracts and antibodies have attracted much attention.[1] The majority of the reported sol-gel –modified biosensors are based on enzymes trapped in silica matrix.[2] Numerous reports have established that, in the majority of cases, sol-gel entrapped biological molecules retain their characteristic biochemical functionality and remain stable over periods of months. However, low pH or high alcohol levels during the sol-gel synthesis can be harmful.[3] Positively charged $Al_2O_3$ sol-gel has been found to be a suitable matrix for improving the stability of immobilized enzymes.

Parameters of the sol-gel process influence structural characteristics of the product. For example molar ratio of precursor materials, reaction time and temperature, concentration of catalytic acid and the solvent used during the reaction affect the material composition.[4]

## 2. EXPERIMENTAL

Tetraethyl orthosilicate (TEOS), (3-glycidoxypropyl) trimethoxysilane (GPTS), hydrochloric acid (HCl) and 5 m% AlO(OH) in water were reacted to form the sol-gel matrix (see Figure 1). Propyltrimethoxysilane was used additionally in some reactions to enhance flexibility of the coating. Subsequently the formed alcohol and water were evaporated in some experiments followed by isopropanol alcohol dilution. Isopropanol which is a good solvent for sol-gel is not anyhow the best possible diluent for antibodies. If dilution is needed in further tests common, biocompatible solvent will be used.

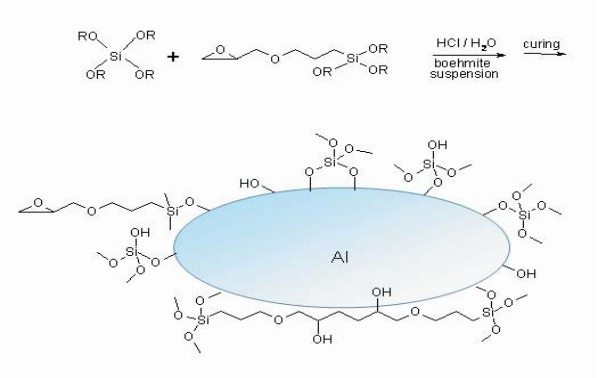


*Figure 1. Si-O-Si network formation on the surface of nanoparticle AlO(OH).*

Several sol-gel materials were synthesized using different reaction conditions and the biocompatibility of the formed materials was tested with fluorescence immunoassay. In "passive coating" sol-gel was spread on microtiter plate wells and layers were cured at 70˚C. Then antibody immunoglobulin G (IgG) was immobilized on top of cured sol-gel layers. "Doped IgG" was achieved by simply mixing the antibody with the sol-gel material before coating and curing. The mixture was spread on microtiter wells after which the layers were cured at 37˚C.

To evaluate the effect of acidic medium on the immobilization of IgG, both low pH sol-gel mixtures and nearly neutral mixtures were tested. pH of the sol-gel mixture was raised with a phosphate buffer before IgG doping or passive coating. In certain cases the buffer precipitated the sol-gel or a precipitate was generated after the addition of the diluted IgG.

The effect of the degree of crosslinking was examined by heating the sol-gel mixture in 70°C for two hours to enhance Si-O-Si crosslinking.

The immobilized IgG was detected in microtiter well plates with fluorescein (FITC) labelled antibodies. Non-specific binding was inhibited with BSA protein. Fluorescence was measured by Wallac Victor 2V with excitation / emission wavelengths 485 nm / 535 nm, respectively.

## 3. RESULTS

Fluorescence measurements showed that biomolecules can be immobilized effectively to the sol-gel material either by passive coating or doping. By changing starting materials, their molar ratios and reaction time, the amount of the immobilized IgG was affected.

In this evaluation GPTS/TEOS/AlO(OH)/HCl (and also GPTS/TEOS/PTMS/AlO(OH)/HCl) with certain molar ratios proved to be the best combination of materials to be used with IgG antibody. The amount of immobilized IgG was reduced without TEOS in the mixture. Same effect was detected when GPTS was not present (see Figure 2).

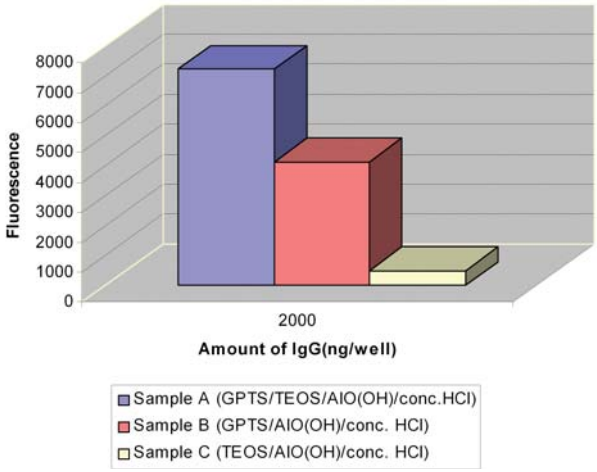


*Figure 2. Fluorescence of IgG doped sol-gel matrixes.*

According to our results the amount of immobilized IgG was highest with nearly neutral sol-gel matrix (Figure 3) which is supported by the fact that very often biomolecules are treated in physiological environment. Enhanced crosslinking of the sol-gel increased the doped IgG response (see Figure 4).

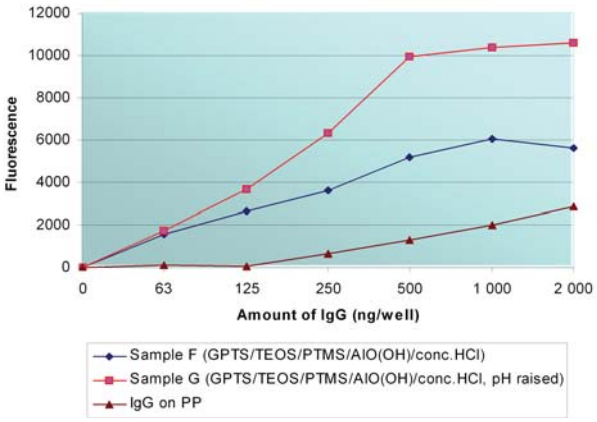


*Figure 3. Effect of pH on immobilized IgG.*

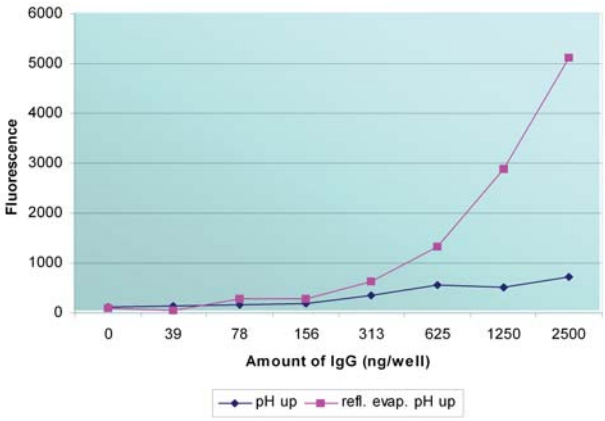


*Figure 4. Effect of crosslinking.*

Passive coating of IgG was increased when the matrix was highly crosslinked which was achieved with long reaction time (Figure 5). As shown in Figure 6 the amount of passive coated IgG antibody on the sol-gel was even higher than on plain polypropylene microtiter well plate.

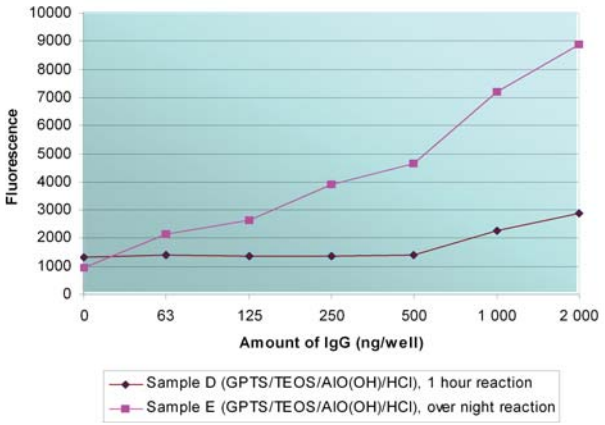


*Figure 5. Fluorescence of passive coated IgG.*

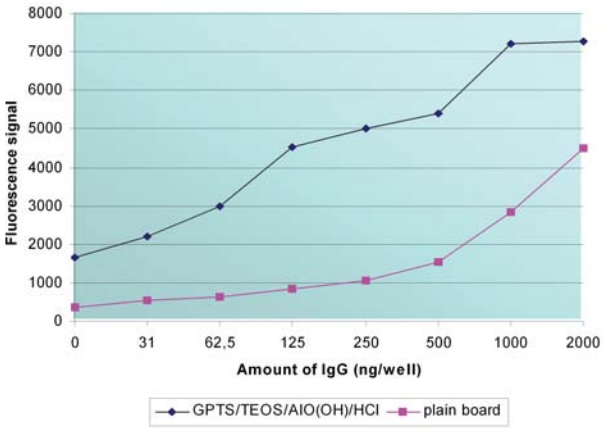


*Figure 6. Comparison of passive coating of IgG on sol-gel and on plain microtiter well (background is not subtracted).*

## 3. CONCLUSIONS

Sol-gel materials can be used successfully with biomolecules. Sol-gel material composition affects considerably the amount of immobilized antibody IgG as shown by fluorescence measurements. Reproducible results are achieved by optimized material synthesis which leads to certain material composition and enhances the immobilization of IgG in the sol-gel. According to our tests the passive coating of IgG is better when immobilized on a hydrophobic boehmite based sol-gel coating than on a plain polypropylene microtiter well.

Our next experiments will include other antibodies to verify their retaining activity under test conditions.

## REFERENCES

1. Shabat, D.; Grynszpan, F; Saphier, S.; Turniansky, A.; Avnir, D.; Keinan, E. Chem. Mater. 1997, 9, 2258-2260.
2. Liu, Z.; Deng, J.; Li, D Analytica Chimica Acta 407(2000)87-96.
3. Brennan, J.D.; Benjamin, D.; DiBattista, E.; Gulcev, M.D. Chem. Mater. 2003, 15, 737-745.
4. Brinker, C.J. and Scherer, G.,W., Sol-Gel Science, Academic Press, San Diego, 1990.



## ACKNOWLEDGEMENTS

The European Regional Development Fund, the Provincial State Office of Oulu and the city of Oulu are highly acknowledged for funding the project.



Liisa Kivimäki
*Liisa.Kivimaki@vtt.fi*



Markku Känsäkoski
*Markku.Kansakoski@vtt.fi*



Arto Maaninen
*Arto.Maaninen@vtt.fi*



Hanna Männikkö
*Hanna.Mannikko@vtt.fi*



Harri Kopola
*Harri.Kopola@vtt.fi*

Matti Höyhtyä
*Medix Biochemica, Matti.Hoyhtya@medixbiochemica.com*
Timo Pulli
*VTT Biotechnology, Timo.Pulli@vtt.fi*

# Gravure Printing of Biomolecules

## 1. INTRODUCTION

The need of rapid and reliable analyzing systems for welfare technology and medical care is apparent. Today the time from sampling to result can take hours or even several days. As a part of generating new biomolecule detection systems we have developed biocompatible materials to be used in disposable sensors in the future. Mass-productive printing technology can be used to achieve cheap disposable sensors. The development work has been done in BioOulu project which is a multidisciplinary project combining biotechnology, information technology, chemistry and electronics expertise.


*Figure 1. Material testing with gravure printing machine.*

## 2. EXPERIMENTAL

Tetraethyl orthosilicate, (3-glycidoxypropyl)trimethoxysilane, propyltrimethoxysilane, hydrochloric acid and 5 m% AlO(OH) in water were reacted to form the sol-gel matrix for antibody immunoglobulin IgG. Water and alcohol produced during the sol-gel reaction were evaporated and the mixture diluted with isopropanol alcohol. Occasionally pH of sol-gel was raised with a phosphate buffer and IgG was doped to the sol-gel. Obtained material was printed on polystyrene slides which were RF-plasma etched before use to achieve better adhesion of the material. Table top gravure printing machine (IGT) was used for printing tests (Figure 1).

The immobilized IgG in sol-gel was checked with fluorescence measurement using Alexa Fluor 546 labelled antibodies specific to the printed IgG-sol-gel –coating. To prevent non-specific binding the slides were treated with BSA protein (bovine serum albumin). Fluorescence was detected with Molecular Imager FX Pro equipment (Bio-Rad) using excitation/emission wavelengths 532/555 nm, respectively. In quantitative IgG measurements equal volumes of sol-gel and IgG dilution were mixed and a certain amount of it placed on the IGT blade for printing. Amounts of IgG on slides were calculated from these volumes which inevitably gives too large detected IgG values on whole slides.

## 3. RESULTS

Sol-gel material with doped antibody can be printed successfully with table top gravure printing machine. With optimization of machine parameters rather smooth sol-gel layers were obtained.

Immobilization of antibody IgG to sol-gel has been investigated during the biocompatible material development and the immobilization was found to be effective. With these printing tests we have shown that IgG stays immobilized in the sol-gel also after gravure printing process. IgG immobilized most effectively to nearly neutral sol-gel matrix but immobilization could be detected also at the acidic medium (Figure 2).

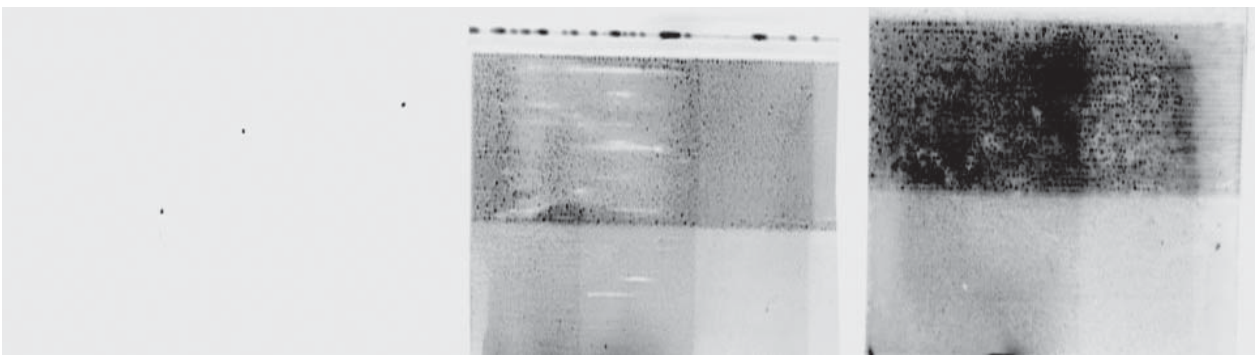

a) b) c)

*Figure 2. a) Plain printed sol-gel without immobilized IgG (negative control), b) sol-gel with low pH + IgG, and c) Neutral mixture of sol-gel + IgG. The highest fluorescence in c).*

The need for blocking the printed sol-gel with BSA to prevent non-specific binding of the label was tested with plain sol-gel surfaces (no IgG). According to these tests fluorescently labelled antibody does not bind non-specifically to the sol-gel. Thus BSA blocking can be left out, which reduces treatment steps (Figure 3). Different concentrations of immobilized IgG in sol-gel can be detected as presented in Figure 4. Dark, quite large dots in Figures 3 and 4 come from the glass substrate.

## 3. CONCLUSIONS

Our results prove that the developed material is biocompatible and can be printed also when an antibody is immobilized to the sol-gel. As our knowledge this is the first time sol-gel doped antibodies have been successfully gravure printed and detected with fluorescence measurement. According to our tests it is possible to differentiate IgG amounts from slides but the exact limit for detectable antibody is unknown. Our results suggest that the fluorescence label does not bind non-specifically to the sol-gel which simplifies sample treatment for fluorescence detection.

The next step in our investigation will be to verify the retaining activity of some other antibodies immobilized to the sol-gel mixture and gravure printed on plastic substrates. Labelled antigens will be used for fluorescence detection. Also the quality of printing process will be improved to attain still smoother coatings. The stability of antibodies in sol-gels after printing have to be evaluated.

## ACKNOWLEDGEMENTS

The European Regional Development Fund, the Provincial State Office of Oulu and the city of Oulu are highly acknowledged for funding the project.

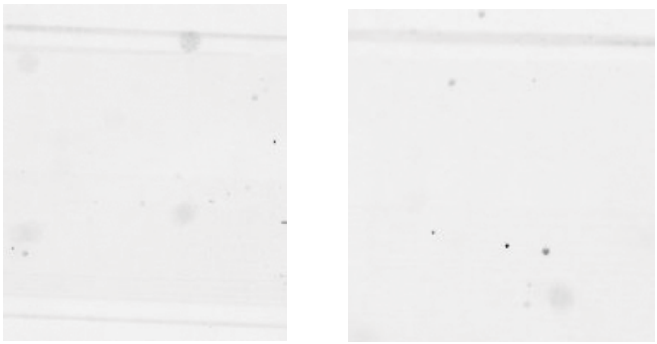

*Figure 3. Non-specific binding of the fluorescently labelled antibody was not detected. No BSA treatment in the left, BSA treatment done on the right.*

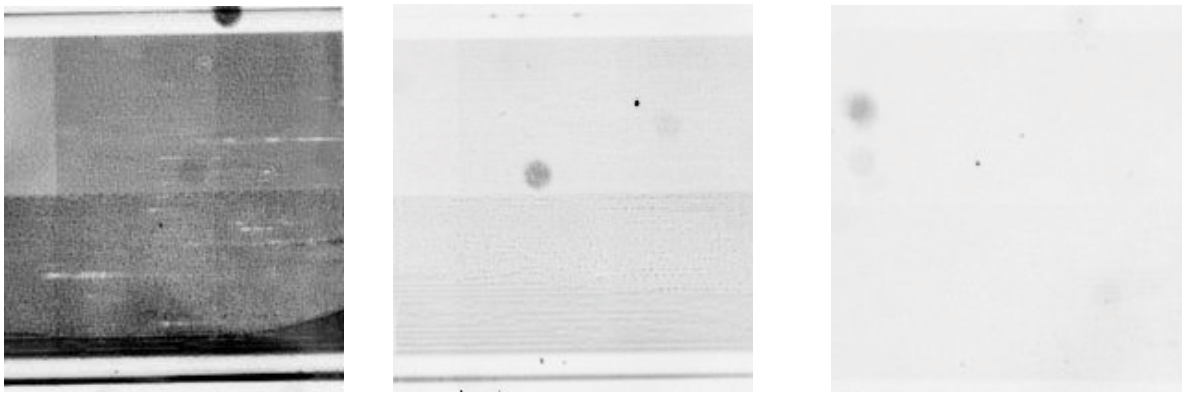

*a)* *b)* *c)*

*Figure 4. Different concentrations of IgG immobilized to the sol-gel mixture. a) 20 micrograms placed on the blade. b) 2,5 micrograms placed on the blade c) 300 nanograms placed on the blade. No detected IgG in c).*

Liisa Kivimäki
*Liisa.Kivimaki@vtt.fi*

Markku Känsäkoski
*Markku.Kansakoski@vtt.fi*

Marika Leinonen
*Marika.Leinonen@vtt.fi*

Hanna Männikkö
*Hanna.Mannikko@vtt.fi*

Arto Maaninen
*Arto.Maaninen@vtt.fi*

Harri Kopola
*Harri.Kopola@vtt.fi*

# Integrated Optical Biosensor

Most conventional analyses for biomolecules require a chemical laboratory with expensive equipment, transportation of samples, well-trained employees to perform the tests and a lot of time for the samples to be transported, reported, tested and the final results be interpreted. In the BIODET 2 project, the objective is to study and develop an integrated optical biosensor, which is smaller, quicker and simpler to use and cheaper to fabricate and use than conventional laboratory equipment. In practice, the biosensor should be constructed on one chip, maybe a disposable one, with dimensions less than a matchbox. With great probability this biosensor needs separate equipment for the interpretation of samples.

## 1.INTRODUCTION

Although a wide range of integrated optical biosensors have evolved for the measurement of biomolecules, these sensors are still quite rare in everyday life, because the price of the reading equipment and biosensor chips has to be noticeably lower compared to conventional analysis equipment. This has proved to be hard to obtain, because the fabrication methods of earlier chips have been too expensive and reading equipment has been quite complicated and thus pricey. Despite the troubles with the prototypes, the basic idea of an integrated biosensor is very alluring. With the help of the development in materials (e.g. thin films and Sol-Gel-materials) and in fabrication methods, the price of an integrated biosensor has been reduced and the aim of a low-cost biosensor is once again achievable.

The objective of our research is to analytically model an optical integrated biosensor, which would serve as a prototype for future product development at VTT Electronics. The major issue in this first configuration is the realisation of a single-mode Young interferometer structure, which possesses sensitivity high enough for biosensor applications (e.g. refractive index change of a magnitude $10^{-5}$).

## 2.INTEGRATED OPTICAL BIOSENSORS

Optical biosensors assort well for applications in different areas such as process control, health care, food industry and environmental control, because they can show a high resolution over a wide dynamic range. IO sensors are typically constructed as waveguide structures, where the incident light is reflected back and forth inside the layer with the highest refractive index. This enables the establishment of the sample solution or antibody-antigen binding process on top of the waveguide structure.

In Interferometric IO sensors, the sensing and reference arms are usually located very close to each another as in Figure 1. This prevents the effect of undesirable influences like temperature variations, because they are identical for both branches and do not affect the output signal. In the IO sensor, the incident wave is divided into two with an optical Y-junction. When the propagating light passes the sample surface, there will be a change in the phase due to the change in the refractive index of the cover. To measure this change, there is a reference branch. The reference branch is placed adjacent to the sensing branch, but it does not encounter a phase change induced by the sample. In the first stage of the experiments the sensitivity and functionality of an integrated biosensor is usually tested with glucose-water solutions. In that case, the reference arm is exposed to the solvent in order to remove the additional phase change induced by the solvent in the sensing arm. When the waves of both arms are combined, they interfere and create a sinusoidal variation, which is related to the change in the refractive index of the cover in the sensing arm. Depending on the sensor type, the divided waves can be combined after the sensing window, as in a Mach-Zender interferometer, or they can be brought out of the waveguide separately and joined e.g. on a CCD-array as in a Young interferometer.

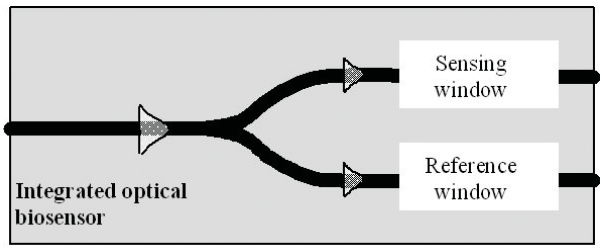


*Figure 1. Top-view of the integrated optical Y-junction channel waveguide.*

## 3.YOUNG INTERFEROMETER

A special problem in interferometry is the ambiguity of the measured signal. The reliability of the measurement is hard to confirm, because of the sinusoidal transmission curve. If the interferometer has been tuned close to one of the maxima or minima of the transmission curve, the signal will fade. Additionally, the periodicity of the transmission curve makes it hard to know whether the detected intensity value is from the positive or from the negative slope of the transmission function. Fluctuations in laser intensity or of the coupling efficiency might be seen as signal changes and thus might cause misinterpretations. The Young interferometer avoids these disadvantages, because the output of it consists of a whole inten-

sity pattern instead of a single intensity value. When the output beams interfere, they create an interference pattern of alternating dark and light fringes. When a phase change occurs, the interference pattern will shift. The shift in interference pattern generates a sinusoidal output as in Figure 2.

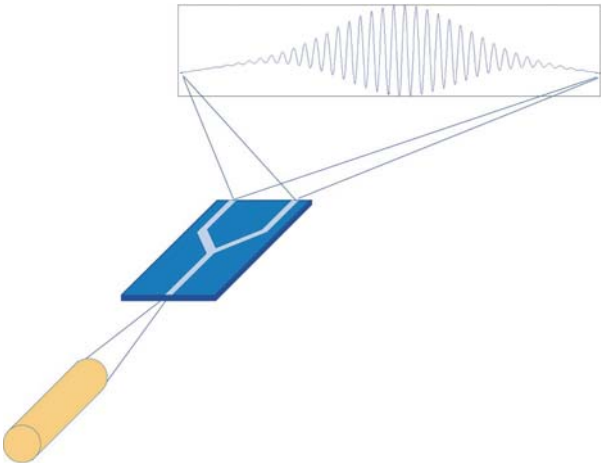

*Figure 2. A young interferometer with a sinusoidal output.*

## 4. EXPERIMENTS AND RESULTS

One Young interferometer structure, presented in table 1, was chosen for experimental studies. The sensitivity and functionality of the sensor was studied with two reference cases: first, both windows were exposed to air and then they were covered with deionised water. Two glucose-water solutions with concentrations 0.05% and 0.1% were used as samples. The measuring configuration is presented in Figure 3.

*Table 1. Young interferometer structure*

| | |
|---|---|
| Half height width of the film | 3.7µm |
| Height of the film | 2.8µm |
| Refractive index of the film | 1.49547 |
| Refractive index of the cover | 1.49233 |
| Refractive index of the substrate | 1.49233 |
| Distance between waveguide arms | 60µm |
| Theoretical optical sensitivity constant | $9.3566 \cdot 10^{-5}$/nm |

The light source used was a semiconductor laser with 676.7nm wavelength and 94mA threshold current. The CCD-camera distance from the focus point during the experiments was 2mm. The sample and reference solutions were applied to the measuring chip by dropping a 2.5µl solution drop approximately on top of the window areas.

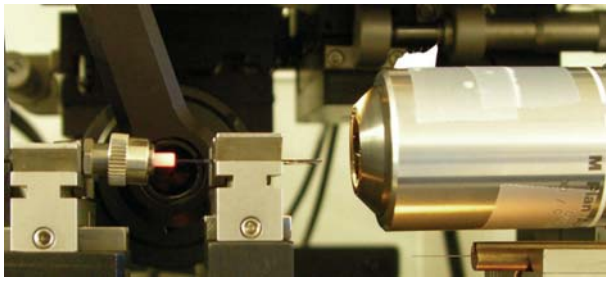

*Figure 3. Close-up picture of the set-up: Semiconductor laser on the left, biosensor-chip in the middle and a lens objective with sixtyfold magnification leading to a CCD-camera on the right.*

The solutions applied in the experiments could only affect the interferometer on top of the exposed window areas.

During the experiments, the effective area lengths varied as Table 2 shows and thus the measurements tell us more about the effect of the difference in effective area lengths than about the effect of the different refractive indexes of the sample solution.

*Table 2. Solution area lengths used in the experiments*

| M. nro | Reference window | Effective area length |
|---|---|---|
| 1 | air | 5mm |
| 2 | deionised H2O | 4.1844mm |
| 3 | deionised H2O | 3.9366mm |
| 4 | deionised H2O | 4.0858mm |
| **M. nro** | **Sample window** | **Effective area length** |
| 1 | air | 5mm |
| 2 | deionised H2O | 4.2177mm |
| 3 | 0.05% solution | 4.2638mm |
| 4 | 0.1% solution | 4.1791mm |

The main maximum line deflections in four cases, presented in Table 2, have been determined and can be seen in Figure 4 along with the theoretically modelled deflections.

When the theoretical and experimental transitions were compared, the theory seemed to resemble the experiments fairly well. However, when the average deviation of the theory was changed to the effective refractive index unit, the error was about 2%, when the effective refractive index change was compared to the theoretical sensitivity constant.

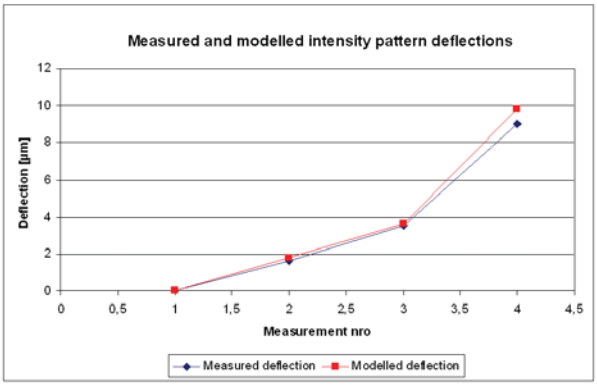


*Figure 4. Experimental and theoretical deflections.*

## 6. CONCLUSIONS

The experimental studies confirmed that the integrated optical biosensor does function as expected, but the sensitivity of the method did not seem to be as good as was assumed. However, a more detailed sensitivity analysis revealed that several uncertain parameters could have affected the measurements. The additional phase changes were affected so strongly by the effective area lengths that it is hardly possible to say anything about the sensitivity of the measurement method or about the equivalence of the theory to reality. For a more precise comparison between real phenomenon and the theoretical model we will need to have a more controlled measuring configuration. This could be achieved by a controlled sample and reference solution areas, realised by a flow through cuvette, and by calculating the change in the maximum line position with the weighted average method.

Sanna Ollitervo
*Sanna.Ollitervo@vtt.fi*

Markku Känsäkoski
*Markku.Kansakoski@vtt.fi*

Arto Maaninen
*Arto.Maaninen@vtt.fi*

Jukka Hast, Hanna Heikkinen
*University of Oulu, Optoelectronics and Measurement Laboratory*

Harri Kopola
*Harri.Kopola@vtt.fi*

# Developments in the Design and Prototyping of Injection Moulded Plastic Optics at VTT Electronics


## ABSTRACT

Demand for low-cost and easily manufacturable optical components is increasing. Two examples of VTT Electronics' activities in the field of injection moulded polymer optics are presented. The first example is a novel device that can be attached to a mobile camera phone, and the second is a low-cost illumination module based on an LED. The prototype imaging and illumination lenses utilised in the example systems were manufactured in Finland with low-cost prototype injection moulds.


Keywords: plastic optics, injection moulding

## 1. INTRODUCTION

One of the current trends in the field of optics is the move towards high volume and low cost systems based on plastic components. At VTT Electronics, this trend has become apparent by the increasing number of inquiries and actual customer projects concentrating on developing modules and systems based on plastic optics. The main benefits of using plastic components are light weight, low cost, mass-producability and the possibility to integrate complex mechanical features into optical parts.

Traditional glass lenses and metal mirrors can, in many cases, be replaced with plastic ones in order to achieve less expensive, easily manufacturable and simpler designs. The rapid development in optoelectronics and especially in LED-technology has also created some new market areas for optical components. Often the mandatory demand for mass-producability constrains the selection of manufacturing technology to injection moulding. A good example of a consumer electronics product is the mobile phone, in which injection moulded optical parts are used in illuminating the keyboard and display and as imaging components in the camera module. In conjunction with LEDs, plastic optics is also moving towards special illumination applications like car interior lighting and traffic lights. As the brightness of LEDs is rising and the prices dropping, they are also gaining ground from the incandescent bulb and fluorescent tube dominated general illumination market. Another potential application field for polymer optics in the future is in the low cost and disposable medical diagnostics device market. As bio-sciences progress, there will be an increasing need for more complicated, but still inexpensive, analysis systems to be used at doctor's offices or even at home by individual consumers. With these views in mind, it is clear that the demand for low cost and mass-producable optical components is increasing and injection moulded polymer optics is the obvious choice.

In this article, two examples of VTT Electronics' activities in plastic optics are presented. The first example is a novel add-on device to a camera phone involving laser and LED illumination as well as imaging optics. The second example is a demonstration module for low cost LED illumination. In both cases, the injection moulded optical components were manufactured in Finland via a network of mould manufacturers and injection moulders.

## 2. ADD-ON DEVICE FOR A CAMERA PHONE

Figure 1 shows the basic concept behind a novel optical device invented at VTT Electronics. The main idea is to have, on the side of a product package, a small printable diffractive ROM (Read Only Memory) element, which can be read by illuminating it with a laser-beam and photographing the resulting pixel matrix pattern with a camera phone. The element contains information in the same manner as a traditional bar-code, but due to the 2D-pattern and diffractive nature of the tag, a much larger amount of information can be packed into a smaller area. The actual reflective ROM elements have been developed previously by the University of Joensuu and VTT Electronics in the Tekes funded PRINTO-project.

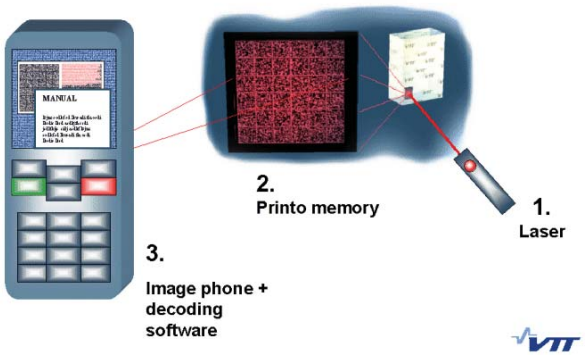


*Figure 1. Basic concept behind the diffractive ROM reading device.*

During 2004, the basic concept of the reading device was developed further as part of VTT Electronics' strategic MINARES-project. A system with illuminating laser and reading optics was designed as an add-on device to a camera phone (Nokia 6600). Figure 2 shows the optical concept of the device. The additional reading optics functions like a telescope as it images the far-field pattern produced by the illuminated ROM element into the aperture of the phone's camera. The phone's camera lens then images the pattern to the image sensor and a picture can be recorded with the phone's standard software. The illuminating laser beam is directed at the element from the same direction as the reading optics.

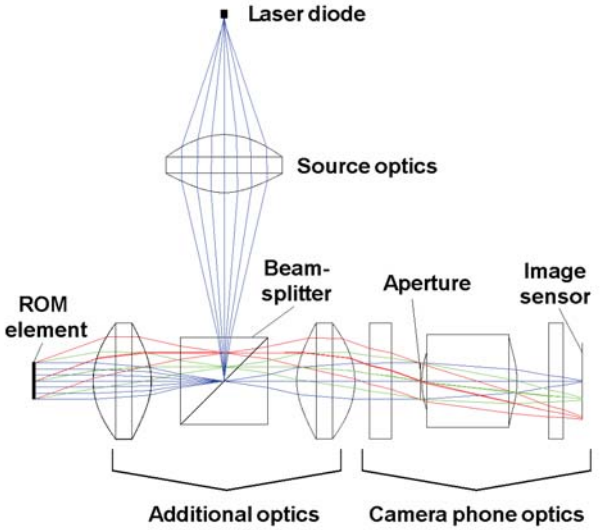


*Figure 2. Optical concept of the reading device.*

The mechanical design of the device was made in such a way that the system can be used in three different modes – in other words, the design was made to be modular. Figure 3 shows the mechanical sketches of the three-stage device. First lens of the additional optics forms an intermediate image, which is relayed into the camera optics by the second lens. By removing the first lens and adding an illuminating LED, a "microscope" can be created. With the first lens intact the optics functions as a telescope and it enlarges distant objects by a 2.3x magnification. The ROM reading device is created simply by adding laser illumination to the telescope optics.

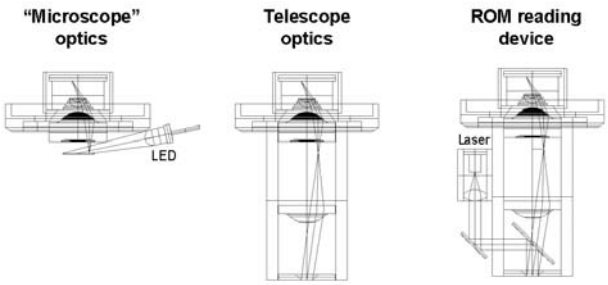


*Figure 3. Concept of the three-stage structure.*

Figure 4 shows the concept of the microscope optics. The approximately 4 mm diameter imaged area is illuminated from the side with an LED. A "microscope" lens is positioned in front of the phone's camera module. The image produced by the optics is magnified by 10x if the full picture is viewed with the phone's own display and can be as large as 30x if the image is viewed with a larger display e.g. PC screen.

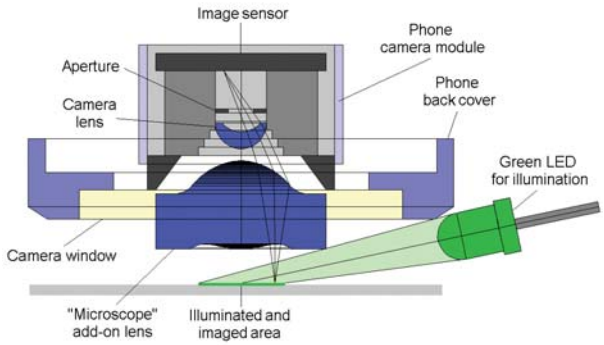


*Figure 4. Concept of the microscope lens.*

The "microscope" lens was manufactured as a pilot case in a Tekes-funded MITMM-project, which was carried out during 2003-2004. The double-aspheric lens was used as a test case for manufacturing injection moulded imaging lenses in Finland. Figure 5 shows two lenses manufactured with a two-cavity prototype mould. The lenses are still attached to the U-shaped sprue. Clear diameter of the optical surfaces is 5 mm and the components have flanges for mounting.

*Figure 5. Injection moulded, double-aspheric imaging lenses manufactured in Finland.*

Figure 6 shows mechanical design of the device, which is attached to the back of the phone in the place of battery cover. The shape of the device follows tightly the shape of the phone. The first module contains the microscope lens. All electrical components like switches, LED and laser were also assembled into the first module. The second module, which is attached partly on top of the first module, contains the first lens of the telescope and illumination beam steering optics with mirrors and a beam splitter. The mechanical parts were milled from black plastic at VTT's workshop. Some adjustments for the laser

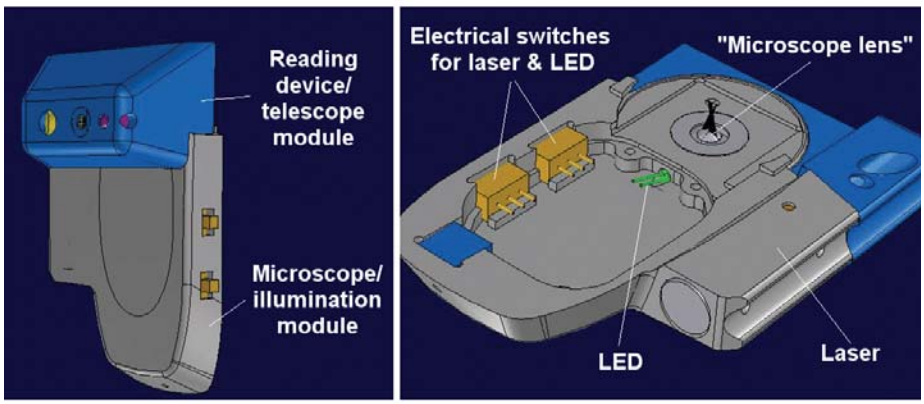


*Figure 6. Mechanical design of the add-on device.*

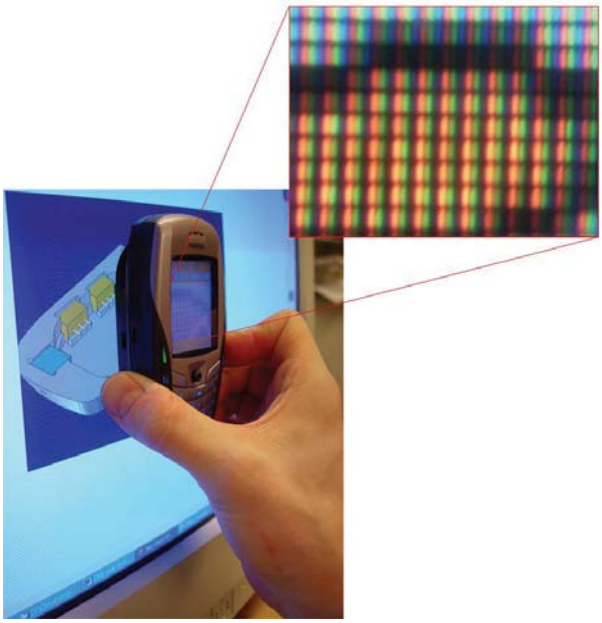

*Figure 7. Microscope lens reveals the sub-pixel (size 0.06 x 0.18 mm$^2$) structure of a display.*

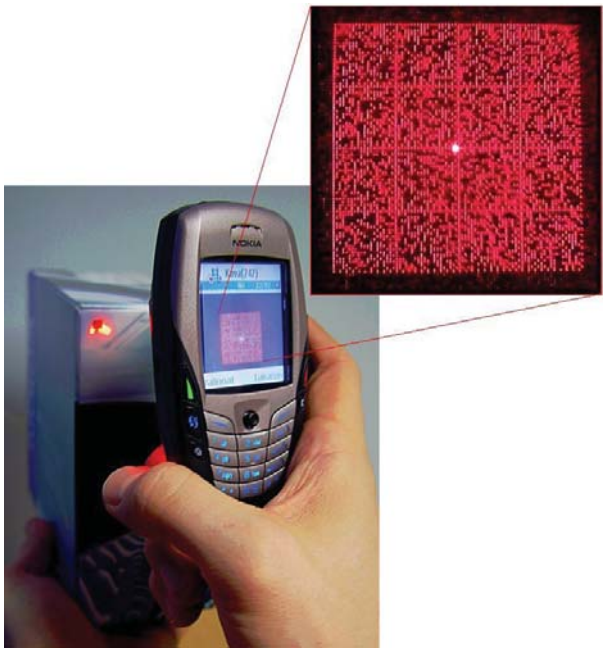

*Figure 8. The reading device brings out the 80 x 80 pixel datamatrix coded in the ROM-element.*

pointing direction were also added to the housing. Electric power for the laser and LED is taken directly from the phone's own battery.

Figure 7 shows an example picture taken with the "microscope" lens attached to the Nokia 6600 camera phone. The picture shows that the optics can easily determine the sub-pixel structure of a display. In this case, the size of the three coloured sub-pixels was 60 µm x 180 µm. The image was taken with the camera's standard software.

Figure 8 shows an example picture taken with the telescope optics attached to the phone. The 80 x 80 data matrix projected by the diffractive ROM element under laser illumination can be seen with a 0th diffraction order bright spot in the middle. The information contained in the matrix can be decoded with special software that can be programmed into the mobile phone.

### 3. LED ILLUMINATION DEMONSTRATION MODULE

Figure 9 shows the basic idea of an LED illumination demonstration module that was manufactured as VTT Electronics' own pilot case in a Tekes-funded INTOR-project. The purpose of the module was to test the possibility to design and manufacture mass-producable and low cost plastic components for controlled LED illumination.

In this case, the lens was designed to collimate the light emitted by a surface mountable LED. A simple lens holder was designed to lock to the lens with a friction bond. The holder is attached to the circuit board with small snap hooks that go through holes drilled into the circuit board around the LED soldering pads.

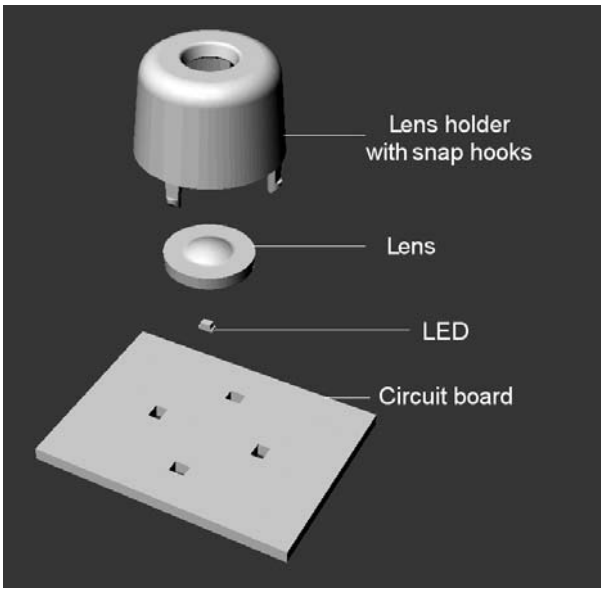


*Figure 9. Concept of the LED illumination module.*

A prototyping mould with inserts (see Figure 10) was used for making the two injection moulded parts. The mould inserts had three cavities – one for the holder parts and two cavities for lenses. The same mould can be used to produce both holders and lenses by changing the plastic material from opaque to transparent and rotating the injection nozzle by 180°. The total cost of the prototype mould design and insert manufacturing was only 5500 €.

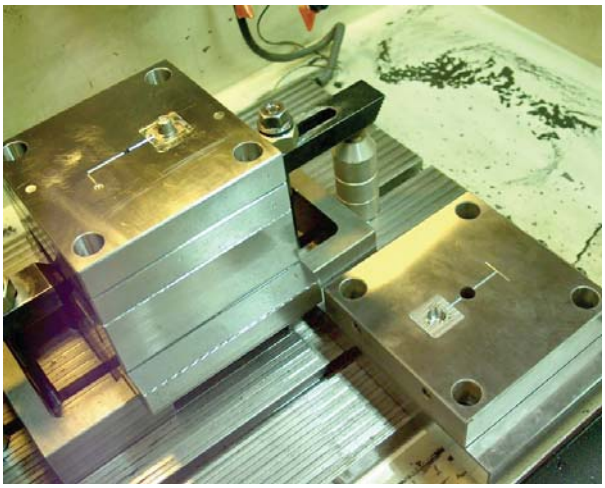

*Figure 10. Unfinished three-cavity prototyping mould inserts.*

Figure 11 shows a moulded 7 mm diameter clear lens part and a 12 mm high black holder part. The third part in the picture is a test piece, which shows one holder and one lens still attached to a common sprue. The lens had two aspheric optical surfaces with 5 mm clear aperture. The components shown in the picture were the results of the first test runs. The INTOR-project continues in 2005 and further test runs will be performed with the lenses. Further development includes the shape measurements of the mould and lenses and possible reshaping of the mould lens cavity based on the measurement results. The second lens cavity will also be equipped with a single point diamond turned optical inserts for very good optical surface quality and shape accuracy.

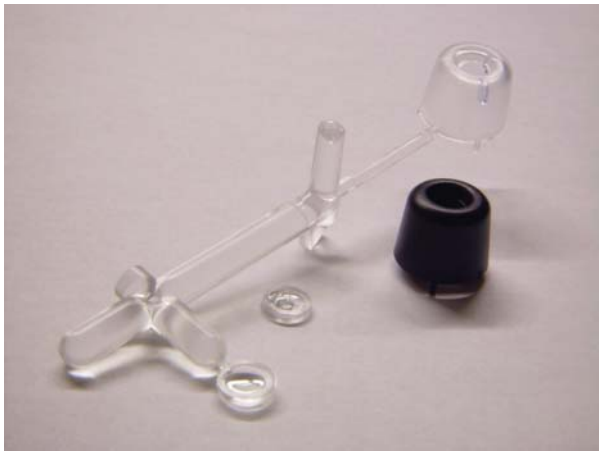

*Figure 11. Injection moulded parts: clear lens, black holder and a test piece with both components.*

In Figure 12, a whole assembled illumination demonstration module is shown. A battery holder, resistor, button switch and LED were soldered to a test board. Three holes were drilled around the LED pads for lens holder snap hooks. Optics assembly was very simple – the lens was pushed inside the holder and the holder hooks were slipped through the holes of the board.

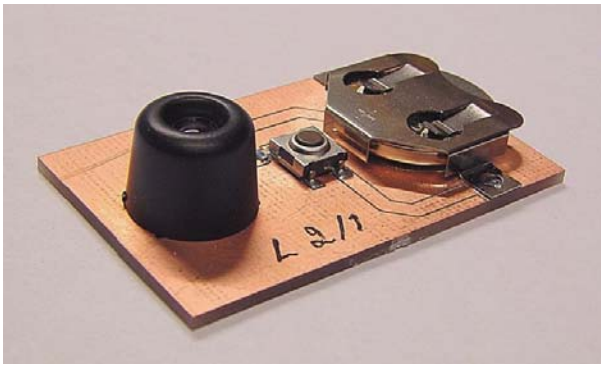


*Figure 12. An assembled demonstration module.*

The first assembled test modules functioned as expected. The lens actually imaged the top of the LED to a long distance. Divergence of the nearly collimated illumination beam was around 3 degrees. Figure 13 shows an illumination spot close to the module. The spot is circular and quite even.

*Figure 13. The module produces a round and nearly collimated illumination beam.*

## 4. DISCUSSION

Manufacturing plastic optics differs from standard injection moulding of mechanical parts mainly in the quality requirements set for the components. Typically, imaging optics have tighter tolerances than illumination optics, but in both cases they are on the limit of mould manufacturing and injection moulding capabilities. Geometrical shapes need to be controlled with considerably higher precision and surface quality, and material uniformity needs to be much better than what is considered standard in the mainstream injection moulding industry.

In standard production, injection moulded parts are generally inspected with an eye, with simple hand-held instruments like slide gages or by fitting the various mechanical parts together. The allowed surface roughness and shape deformations in optics, however, are typically too small to be seen with a naked eye and too complicated to be measured with a ruler. Proper functioning of separate optical parts is also very difficult to determine without special optical measurements. This means that a set of sophisticated characterisation equipment like an MTF device, interferometer and expensive coordinate measurement system are needed to determine if the parts meet the specifications or not. Optical part characterisation resources are a key factor that most injection moulders and mould manufacturers lack if they want to start optical parts production. There are currently only a handful of such firms in Finland that can manufacture optical injection moulded parts and none of them are making actual imaging optics. Large-scale illumination optics have generally less stringent quality requirements, but they too can benefit from proper characterisation measurements.

Designing, manufacturing and characterising optical parts requires a lot of special knowledge. DFM (Design For Manufacturing) ideology is a vital factor when mass-producable and low-cost parts are needed. By knowing the possibilities and limitations of the required manufacturing technology, the designers are able to make easily manufacturable quality designs. VTT Electronics has a long history in designing and prototyping optoelectronic systems especially for telecommunication, machine vision and optical analyser applications. During the last few years the injection moulded plastic optical components have become more and more important in the wake of some new “consumer electronics” type of applications. In these projects, the role of VTT Electronics can be to manage the whole concurrent development cycle of modules and systems. The optical and mechanical design, as well as the characterisation of components and prototypes, can all be performed under the same roof. In-house mechanical and optical workshops can also produce complicated optical first-round prototype parts. The two example cases presented in this article show that by networking with suitable partners, VTT Electronics is also able to manufacture prototypes that can verify the main production features of real products utilising plastic optics.

Jukka-Tapani Mäkinen
*Jukka-Tapani.Makinen@vtt.fi*

# Possibilities for Using Raman Spectroscopy to Determine the Homogeneity of Pharmaceutical Powder Blends and Dosage of Compressed Tablets

## INTRODUCTION

The homogeneous blending of active ingredients and excipients is an essential element in the manufacturing process of pharmaceutical tablets. Homogeneous mixing ensures good tablet-to-tablet reproducibility. The end-point of the blending operation is traditionally determined by the off-line HPLC analysis of replicated samples. Alternate blending and analysis steps are continued until the sample variations are below the acceptable limits. In addition, the determination of the total amount of active ingredient in compressed tablets, the dosage, is also based on HPLC analysis.

In recent years, optical spectroscopic methods, e.g. NIR, IR and Raman spectroscopy, were applied to determine blend homogeneity. Advantages of optical methods include short measurement time and the possibility to do the measurements in-situ, or at least without sample preparation. We have performed preliminary tests with Raman spectroscopy to determine the homogeneity of powder blends and dosage of compressed tablets. Raman spectroscopy has features that make it very potential in these applications. The spectra are most specific for the species and the spectra of many active ingredients are much stronger than those of common excipients.

A CCD Raman spectrometer developed by VTT Electronics was used in the tests. A 830 nm laser was focused on the sample through a fibre-optic probe and the scattered power was collected with the same probe. The Raman shift range of the spectrograph was 2000-200 $cm^{-1}$ and its resolution was 8 $cm^{-1}$. The size of the measurement spot was 0.5 mm (dia.) and laser power falling on the spot was 100 mW.

## BLEND CONTROL

Only two components, active ingredient (API 1) and lactose were used in a blending test with a turbular mill. Mixing periods of 15 s, 15 s, 30 s, 1 min and 3 min were executed one after another. Raman measurements were carried out between these periods as the mill was stopped and the spectra were measured at 20 different spots through the transparent wall of the mill.

API 1 and lactose have distinct bands close to each other, API 1 at 1100 $cm^{-1}$ and lactose at 1080 $cm^{-1}$. The ratio of the band areas at different spots and their mean values as a function of the cumulative mixing time are given in Fig. 1. At first, the measurement spots hit the area rich of API 1 and the variation was small. Variation then increased as blending proceeded and started to decrease

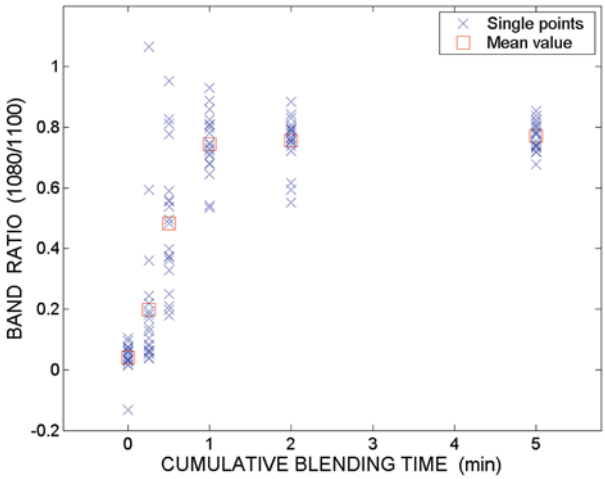


*Fig 1. Band ratio of lactose and API 1 as a function of blending time.*

as the average value approached the level of the homogeneous mixture.

The sample volume covered by a single measurement was small, representing only in the order of 0.1 mg, if we assume the effective sampling depth to be roughly 1 mm. This volume can be increased if the measurements are executed in-situ during blending, and the volume can be easily controlled by adjusting the measurement time, which was short (10 s) in our test. These results already show, however, the effectiveness of the blending process used.

## BLEND HOMOGENEITY

In the second tests, samples were taken from a production batch of a pharmaceutical formulation, which had already been blended and stored in a container. A sampling thief was used and the samples were taken from three different positions and four different depths within the container.

The formulation B composed of an active ingredient API 2 (16%) and five excipients, mannitol having the largest concentration (55%). API 2, and mannitol dominates the spectrum of this formulation (Fig. 2). We used the distinct bands at 1000 $cm^{-1}$ for API 2 and at 870 $cm^{-1}$ for mannitol, respectively, when assessing the local variations. Mannitol serves as a good estimate for the ingredients, representing 2/3 of their total concentration.

Each of the 12 samples were measured at 10 different points, and 6 acquisitions of 30 s (each) were collected and averaged in order to obtain a high-quality spectrum

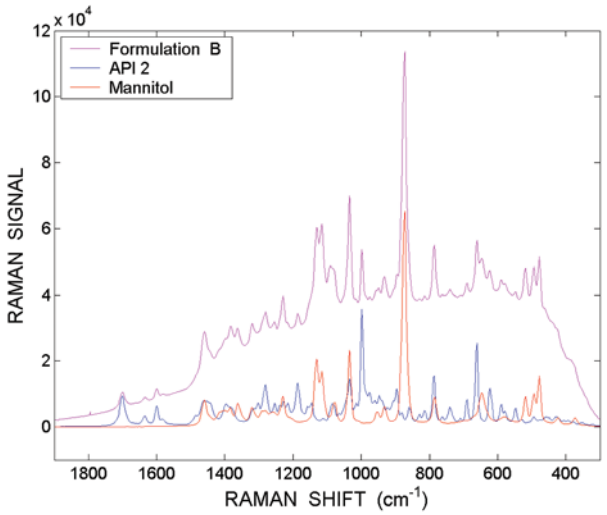


*Fig. 2. Spectra of the formulation B and its two main components.*

for each point. The band ratio of API 2 to mannitol was calculated and the variations between the samples and the mean variation between the single points are presented in Table 1.

*Table 1. Ratio of the band areas of API 2 (1000 $cm^{-1}$) and mannitol (870 $cm^{-1}$) and its variations for the blend of formulation B and for the tablets compressed from this blend.*

| API 2 / mannitol ratio | Powder blend | Tablets |
|---|---|---|
| Mean value | 0.0996 | 0.0996 |
| Variation between samples | 6.7% | 0.7% |
| Mean variation between single points | 3.6% | 4.2% |

Variation between the samples is high (6.7%) compared to the mean variations between single points (3.6%) and can be regarded as real variation in API 2 concentration. The sample volume is now increased to the order of 1 mg by averaging 10 measurement points, but it is still small compared to a normal tablet size 0.1-1 g. The sample volume can be easily increased by moving the sample e.g. with a motorised x-y table during the measurement. A larger sample volume could reduce the variations between the samples and give a more relevant estimate for the variation of tablet dosage.

The physical sampling with a thief can presumably be replaced by constructing a fibre-optic Raman probe inside the thief. The opening of a side-sampling thief can be equipped with a window and the measurement beam focused just outside the window. The whole analysis can be automated by using a robot to handle the thief-probe and the sample volume can be increased by rotating the probe around its axis at each sampling position during the measurement. This technique can give a better picture of the blend homogeneity throughout the whole blending volume.

## TABLET HOMOGENEITY

In the third test we used tablets compressed from formulation B with magnesium stearate as a lubricant. The tablets (10 pcs) were measured at 10 different points, and the band ratio of API 2 to mannitol was determined similarly as for the powder blend and the results are also presented in Table 1.

As the powder is compressed into tablets, penetration of the laser beam remains more limited and the effective sampling depth is considerably only in the order of 0.1 mm, which means that the sample volume obtained by averaging 10 spots is only 0.1 mg. In spite of that, the results are extraordinarily good; the mean value is exactly the same as with the powder blend, the variation between the samples is considerably smaller and the mean variation between the measurement spots is close to the value of the powder blend.

In any case, the measurement provides information only from the outer surface of the tablet and the number of samples is rather small. A possible explanation for the small variation between the tablets can be that the material comes from the same area of the container.

## TABLET DOSAGE

In the fourth test we used amphetamine tablets seized by the police. The main analytical demand for illicit drugs is similar to legal ones, to determine the exact amount of the active ingredient in the tablet. The analytical problem with illicit drugs is more complicated, because the concentration and composition of the excipients varies and are usually unknown to the laboratorian.

We used the approach familiar from HPLC analysis, and dissolved the tablets into a certain amount of solvent and measured the amphetamine concentration in the solvent. Dilute hydrochloric acid (HCl) was used as the solvent, together with an internal standard $NaH_2PO_4$, which gives a distinct band of phosphate (880 $cm^{-1}$) between the amphetamine bands (Fig. 3). The procedure was calibrated with samples of pure amphetamine by using the ratio of the band areas of amphetamine at 1000 $cm^{-1}$ and

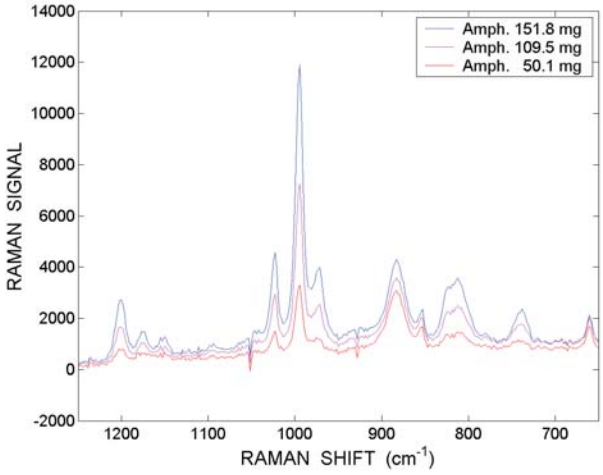


*Fig. 3. Different amounts of amphetamine in dilute HCl. The band of internal standard $NaH_2PO_4$ can be seen at 880 $cm^{-1}$.*

phosphate at 880 $cm^{-1}$, respectively. When analysing the seized tablets, insoluble components were first centrifuged out and an acquisition time of 1 min was used in Raman measurements.

Several batches of seized street samples were chosen and 5 tablets from each batch were analysed using the Raman method. The average value of 5 tablets was compared with the results obtained from the routine HPLC analysis (Table 2). The Raman results are mostly within the margin of error of the HPLC method.

| Seized street samples | Amphetamine (%) | |
|---|---|---|
| | HPLC | Raman |
| Huu4-01076 | 18 | 18,0 |
| Huu4-01075 | 24 | 25,6 |
| Huu4-01363 | 48 | 46,7 |
| Huu4-01377 | 27 | 27,4 |
| Huu4-01237 | 56 | 55,5 |
| Huu4-01324 | 58 | 58,9 |
| Huu4-01296 | 53 | 53,4 |
| Huu4-01376 | 27 | 25,2 |
| Huu4-01386 | 13 | 13,2 |
| Huu4-00833 | 69 | 69,7 |

*Table 2. Results of the HPLC and Raman methods for seized amphetamine samples.*

Compared to the routine HPLC method, the actual analysis time in the Raman method is much shorter. If the preparation of the samples is executed in series, e.g. by using a multi-well sample plate, the average turnaround time can be reduced by using several measurement probes in the Raman analyser. Technically, this can be realised by imaging the spectra from the probes at different heights on a large CCD detector and by using a separate laser for each probe. An adequate number of probes for one detector could be between 6 and 10, resulting in a corresponding decrease in the turnaround time.

## CONCLUSIONS

One of the advantages of Raman spectroscopy is that the instrument can be easily connected to the process and execute the measurements in-situ without any sample treatment. In determining the homogeneity of powder blends or dosage of compressed tablets, the measurement beam cannot penetrate the sample and traditional sampling and sample treatment methods are needed to enable analysis. Also, in these cases, the use of Raman techniques can make the analysis faster and more effective compared to the traditional procedures based on HPLC.

## ACKNOWLEDGEMENTS

This work was supported by the Technology Development Centre (TEKES), and Orion Pharma and KRP kindly provided the samples for our tests.

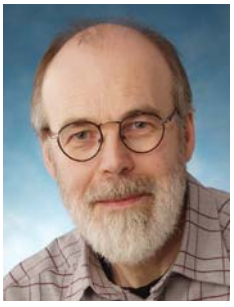

Pentti Niemelä
*Pentti.Niemela@vtt.fi*

Janne Suhonen
*Janne.Suhonen@vtt.fi*

Erja Katainen, Kristiina Järvinen
*Department of Pharmaceutics, University of Kuopio*

# New Multivariate Calibration Method Applied to PAT: API Content in Tablets Using NIR


## ABSTRACT

A new method for multivariate calibration was developed [1] that combines the best features of "classical" (also called "physical" or "K-matrix") calibration and "inverse" (or "statistical" or "P-matrix") calibration. By estimating the spectral signal in the physical way and the spectral noise in the statistical way, the prediction accuracy of the inverse model can be combined with the low cost and ease of interpretability of the classical model, including "built-in" proof of specificity of response. The method was demonstrated [2] on a data set of near-infrared spectra from pharmaceutical tablets, which is available on the web [3] (so-called *Chambersburg Shootout 2002* data set). It was proven that the cost of calibration can be significantly reduced compared to today's standard practice of statistical calibration using PLS or PCR, because the need for lab-reference values is virtually eliminated. Several other, significant advantages are realized as well, which all stem from the fact that the calibration becomes "science-based" and fully transparent to the user. In summary, these advantages mean that in a majority of spectrometric application cases, "cost of calibration" is no longer a roadblock to development and employment of new, application-specific, multivariate analyzers.


## INTRODUCTION

(This paper is basically an excerpt of [2], in which the *Shootout* example and the important implications for the FDA's PAT initiative are discussed in detail.) Standard practice for multivariate calibration today is the so-called "statistical modeling" approach, usually based on a PLS- or PCR-type algorithm. Disadvantages of "statistical modeling" include (i) the difficulty and expense to prepare "calibration standards" with reference concentration values that vary over a large range; (ii) the inability to prove specificity of response; and (iii) the high cost and risk for developing new, application-specific measurement instruments. The latter stems from the fact that hardware specifications can not be derived directly from the spectra, but that, instead, a full-scale statistical calibration is necessary for each "iteration" of the development process.

The proposed new method picks the cherries, so to speak, of the earlier "classical" and "inverse" approaches to multivariate calibration [1,2]. The end result is fully science-based and optimal in the mean-square error sense, i.e., measurement accuracy is as good as or better than the results from costly statistical calibration. All disadvantages mentioned above disappear.

## THEORY

The basic assumption behind spectrometry is that the measured spectrum contains a response from the analyte of interest:

$$\mathbf{x}^T = y \cdot \mathbf{g}^T + \mathbf{x}_n^T \qquad [\text{AU}] \qquad (1)$$

where vector $\mathbf{x}^T$ the measured spectrum (in e.g. absorbance "units," [AU]); scalar $y$ the true and sought-after concentration of the analyte of interest (in units of [mg] in the *Shoutout* example); $\mathbf{g}^T$ the response spectrum of the analyte of interest [AU/mg]; and $\mathbf{x}_n^T$ [AU] everything in the measured spectrum that is *not* from the analyte of interest, including instrumental noise *and* interfering spectra.

The shape of the response spectrum of the analyte of interest, $\mathbf{g}^T$, is determined not only by the chemical structure and state of the sample, but usually also by its physical properties (e.g. scattering) and the type of sampling optics. In other words, $\mathbf{g}^T$ is usually application-specific.

The spectral signal is described by a mean, $\bar{y} \cdot \mathbf{g}^T$, and a root-mean-square (RMS), $\sigma_y \cdot \mathbf{g}^T$, where $\sigma_y$ the standard deviation of $y$. Likewise, the spectral noise is described by a mean, $\bar{\mathbf{x}}_n^T$, and a covariance matrix, $\boldsymbol{\Sigma}$. The latter can be estimated as follows: assume for a moment that a large number, say 10,000, NIR spectra can be measured from tablets with *constant* concentration of Active, say, 200 mg. In other words, the differences between these spectra are solely due to variations in the other constituents and noise sources. Writing all these spectra into one matrix, $\mathbf{X}$,

$$\mathbf{X} = \begin{pmatrix} \mathbf{x}_1^T \\ \mathbf{x}_2^T \\ \vdots \\ \mathbf{x}_{10,000}^T \end{pmatrix} = \begin{pmatrix} 200mg \\ 200mg \\ \vdots \\ 200\ mg \end{pmatrix} \cdot \mathbf{g}^T + \begin{pmatrix} \mathbf{x}_{n,1}^T \\ \mathbf{x}_{n,2}^T \\ \vdots \\ \mathbf{x}_{n,10,000}^T \end{pmatrix} = \mathbf{y} \cdot \mathbf{g}^T + \mathbf{X}_n \qquad (2)$$

shows that after mean-centering, the measured spectra represent only spectral noise,

$$\tilde{\mathbf{X}} = \tilde{\mathbf{X}}_n \qquad (3)$$

where the "~" tilde means that the matrix is mean-centered (the average row is subtracted from all the rows). Thus, the covariance matrix of the spectral noise can be estimated as,

$$\boldsymbol{\Sigma} \cong \frac{\tilde{\mathbf{X}}^T \tilde{\mathbf{X}}}{10{,}000-1} \qquad [\text{AU}^2] \qquad (4)$$

If the NIR spectra contain, e.g., 128 spectral variables (wavelengths), then matrix $\tilde{\mathbf{X}}$ has dimension 10,000 rows x 128 columns, and matrix $\boldsymbol{\Sigma}$ has dimension 128 x 128.

It turns out that the optimum solution to the measurement problem, Eq.(1), is a function of the quantities introduced above. Without further mathematical derivation, the results are given. The optimum b-vector in the sense of minimum mean-square prediction error is [1],

$$\mathbf{b}_{opt} = \frac{\sigma_y^2 \boldsymbol{\Sigma}^{-}\mathbf{g}}{1+\sigma_y^2 \mathbf{g}^T \boldsymbol{\Sigma}^{-}\mathbf{g}} \qquad [\text{mg / AU}] \qquad (5)$$

where $\boldsymbol{\Sigma}^{-}$ the inverse of $\boldsymbol{\Sigma}$. The "*1*" in the denominator of Eq.(5) is responsible for the familiar effect that the slope in the prediction scatter plot turns down towards zero if the "range," $\sigma_y$, of the calibration signal is too small [1]. If the "range" is large ($\sigma_y^2 \to \infty$), then Eq.(5) turns towards the desired, unity-slope result:

$$\mathbf{b}_{opt(1)} = \frac{\boldsymbol{\Sigma}^{-}\mathbf{g}}{\mathbf{g}^T\boldsymbol{\Sigma}^{-}\mathbf{g}} \qquad (6)$$

When $\mathbf{b}_{opt(1)}$ is used to predict the concentration value of a new spectrum, $\mathbf{x}_{pred}^T$,

$$\mathbf{y}_{pred} = \bar{y} + (\mathbf{x}_{pred} - \bar{\mathbf{x}})^T \mathbf{b}_{opt(1)} \qquad [\text{mg}] \qquad (7)$$

(where $\bar{\mathbf{x}}^T = \bar{y} \cdot \mathbf{g}^T + \bar{\mathbf{x}}_n^T$ ) then the standard error of prediction *a.k.a.* standard deviation of ($y_{pred}$-$y$) is,

$$SEP_{opt} = \sqrt{\frac{1}{\mathbf{g}^T \cdot \boldsymbol{\Sigma}^{-} \cdot \mathbf{g}}} \qquad [\text{mg RMS}] \qquad (8)$$

Equation (8) is the spectroscopic, multivariate limit of detection of signal $\mathbf{g}$ in noise $\boldsymbol{\Sigma}$. The PRESS$^{1/2}$ result of a PLS or PCR calibration can be shown [1] to converge with increasing number of calibration standards towards the value of Eq.(8) *if* the error of the lab-reference method is zero and the prediction slope is one and the unspecific correlations (cmp. [2]) are zero. When validating the spectroscopic method against a lab-reference method, the RMS prediction "error" measured (e.g. in the PRESS$^{1/2}$) is Eq.(8) *plus* the inaccuracy of the lab method itself.

To summarize, the proposed method (in its basic form) involves the followings steps: (a) determine "manually" the response spectrum of the analyte of interest, $\mathbf{g}$, in units of, e.g., [AU/mg]; (b) collect a representative population of "noise" spectra and compute $\boldsymbol{\Sigma}$ using Eq.(4); (c) compute $\mathbf{b}_{opt(1)}$ using Eq.(6); and (d) predict new spectra using Eq.(7), where $\bar{y}$ and $\bar{\mathbf{x}}^T$ the mean analyte concentration and the mean spectrum of the "noise" spectra that were used for computing $\boldsymbol{\Sigma}$. (In cases where mean-centering is not desired, $\bar{y}$ and $\bar{\mathbf{x}}^T$ are effectively defined as zero, and Eq.(4) is computed using un-centered spectra.)

## EXAMPLE

Some readers may already be familiar with the *Chambersburg Shootout 2002* data set, which contains near-infrared (NIR) spectra of pharmaceutical tablets probed in "diffuse transmission" [3]. The data set was used at the *IDRC Chambersburg 2002* conference in a competition for designing the best calibration for content of the active pharmaceutical ingredient. (The nature of "Active" is un-disclosed.) When David Hopkins published a spectrum of Active [4], a unique opportunity opened up to demonstrate this new method on a publicly available data set.

Background information on the *Shout-out 2002* data set is available [3,4,5]. Shortly, the data is organized into subsets called *Calibration, Test*, and *Validation*, coming from two spectrometers (hereafter identified as, e.g., *Calibration1* and *Calibration2*). Figure 1 shows some exemplary "raw" spectra. No spectra were deleted as outlier and no spectral pre-processing was performed. Figure 2 shows the available lab-reference values.

Figure 2 shows that all of the *Calibration* tablets and most of the *Test* tablets are so-called "designer samples," i.e., samples that were specifically made for the purpose of calibration. The designer samples show much larger variation ("range") in the content of Active than do the "normal" production tablets, which were obviously used for the *Validation* set and also for parts of the *Test* set. One of the main goals here is to demonstrate that on-line optical

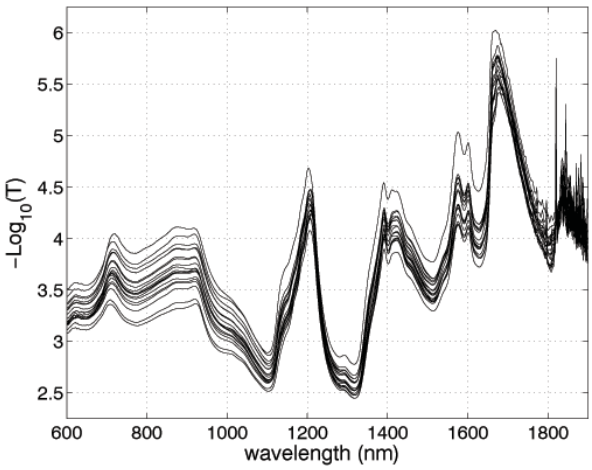


*Figure 1. Twenty randomly selected spectra from data set Calibration1.*

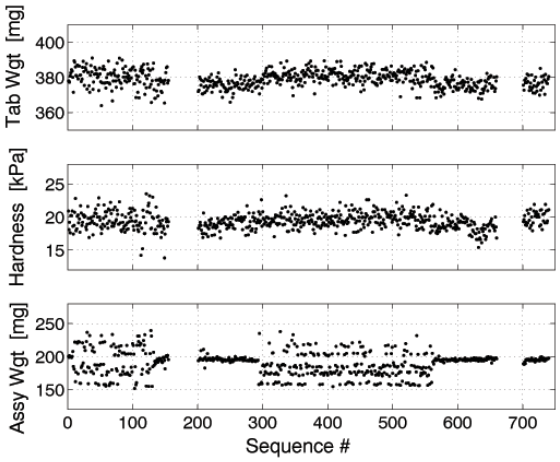


*Figure 2. Sequence of lab-reference values, arbitrarily arranged as follows: Calibration first (m=155); then Test (m=460), then Validation (m=40).*

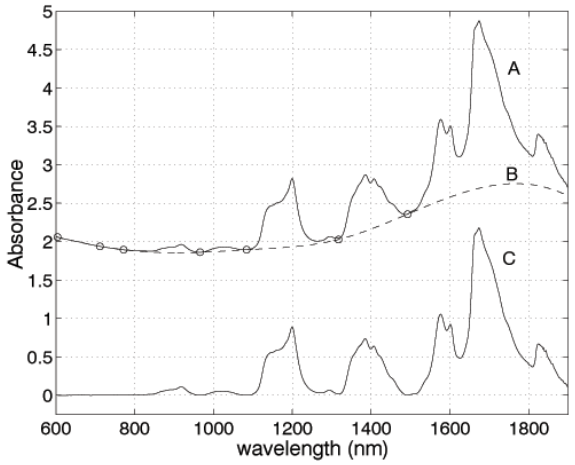


*Figure 3. Spectrum of the active ingredient as measured from pure powder (A); baseline fit (B); and result of baseline correction (C).*

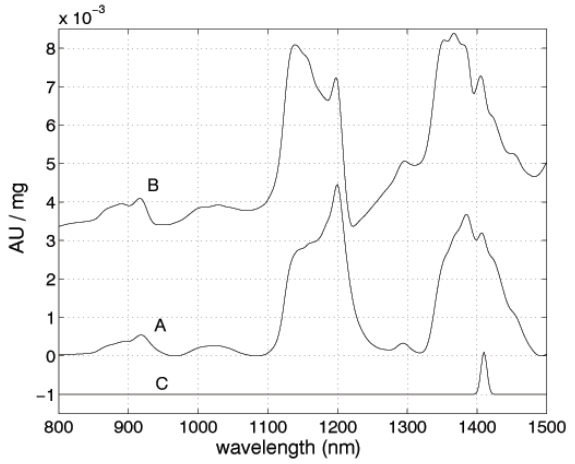


*Figure 4. g-vector estimates: (A) from the baseline-corrected spectrum of the active ingredient; (B) estimate used by PLS (offset +2·10$^{-3}$).*

analyzers can be calibrated not only with a significantly reduced number of lab-reference values, but also without the need to artificially "upset" a smoothly running process in order to produce "range." The first 93 and the last 99 of the *Test* samples (m=460) show low variation in the amount of Active, cmp. Fig. 2 bottom (standard deviation = 2.62 mg, around a mean of 195.4 mg). These samples were obviously made from "normal" production tablets, and we will therefore use these samples to estimate the spectral noise, Σ. By using spectra from both instruments, *Test1* and *Test2*, we can plug 2·(93+99)=384 spectra into Eq.(4), and the inclusion of instrument-to-instrument "noise" will ruggedize the calibration.

Trace A in Fig.3 (hereafter abbreviated as "trace 3A") shows the spectrum of the pure active ingredient as published by Dave Hopkins [4]. Traces 3B and 3C show the author's baseline correction, which produced reasonable results from about 800 - 1500 nm (the circles are the knots chosen for the spline). Trace 3C is in units of [AU] and needs to be scaled to become a g-vector estimate. By dividing by 200 mg, the scaling is set roughly right, say, to within a factor of about 2 (since the spectrum published by Dave Hopkins is representative of "some" average tablet). The result is shown in trace 4A and will be used as g-vector below.

Before demonstrating the new method, some PLS predictions are shown in Fig. 5 for comparison. Trace 4B shows the g-vector estimate that PLS derives from *Calibration1* (cmp. [2]). There is a negative-direction feature at 1220 nm, which is obviously an unspecific correlation (UC). Probably more important, the spectral baseline of trace 4B is offset from zero by about 1.5·10$^{-3}$ AU/mg. This leaves the PLS regression vector sensitive to future changes in the scattering characteristics of the tablets, at a rate of 2.8 mg per 100 milli-AU of flat-baseline shift, which is bad in a PAT application. (PAT being the name of the ongoing FDA initiative encouraging pharma industry to increase the use of on-line analysis methods.) Since pharmaceutical customers fear unspecific response to scatter changes, any g-vector used on tablets should be free from baseline offset.

Some example predictions using the new method are shown in Fig.6. Matrix inversion, $\Sigma^{-}$, was performed using the first 20 PCR factors, which is practically "full-rank." No further scale adjustment of trace 4A was performed (the rough scaling described above happened to be accurate, i.e., produced a near-unity prediction slope). Thus, the formula used for prediction was,

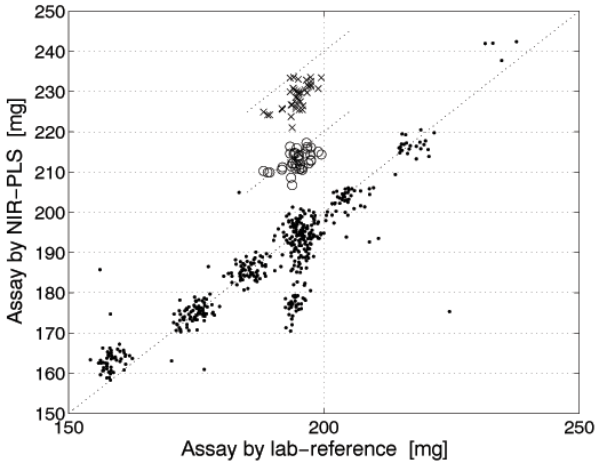


*Figure 5. PLS predictions calibrated from data set Calibration1 (m=155), 3 factors, wavelength range 800 - 1500 nm. Predicted are (•) Test1 (m=460); (o) Validation1 (m=40; y-axis offset 20 mg), and (x) Validation2 (m=40, y-axis offset 40 mg). The ideal prediction lines for each case (identity lines) are also shown.*

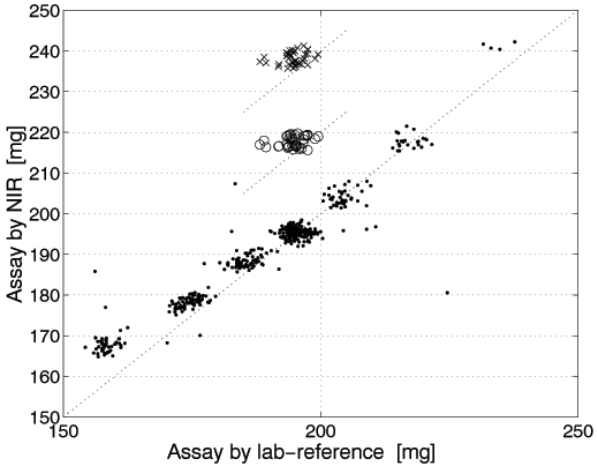


*Figure 6. Predictions using new method as described in the text, g-vector is trace A of Fig.4, wavelength range is 800 - 1500 nm. (•) Test1 (m=460); (o) Validation1 (m=40); and (x) Validation2 (m=40). Offsets like in Fig.5.*

$$y_{pred} = \bar{y}_{n=384} + (\mathbf{x}_{pred} - \bar{\mathbf{x}}_{n=384})^T \cdot \frac{\Sigma^-_{n=384}\mathbf{g}_{4A}}{\mathbf{g}_{4A}^T \Sigma^-_{n=384}\mathbf{g}_{4A}} \qquad (9)$$

where $\mathbf{g}_{4A}$ the g-vector estimate as plotted in trace 4A; and $\bar{y}_{n=384}$ = 195.4 *mg* the mean concentration, $\bar{\mathbf{x}}_{n=384}$ the mean spectrum, and $\Sigma_{n=384}$ the covariance matrix computed from the 384 spectra selected for estimating the spectral noise.

When comparing Fig. 6 with Fig. 5, remember: (a) The results shown in Fig.5 required 155 reference values, whereas only two were needed for Fig.6; (b) the results in Fig.5 required the preparation of "designer samples" with large concentration range, whereas Fig.6 did not require any designer samples; and (c) the predictions in Fig.5 are affected by UC whereas in Fig.6 we know exactly what is being measured, viz., the length of the active agent response spectrum plotted in trace 4A.

The most likely reason for the horizontal spread observed in Fig.6 is inaccuracy of the HPLC reference method, which was 1.3 mg RMS (oral information by Gary Ritchie).

## SUMMARY AND OUTLOOK

A new method of multivariate calibration is described that can provide significant practical benefits compared to the methods of the current practice. The new method combines the best features of the two currently existing approaches to multivariate calibration. Namely, it is proposed that, whenever possible, the user should define the response spectrum of the analyte of interest, **g**, in the "classical" (or "physical" or "K-matrix") way, i.e., by "manual" estimation based on spectroscopic expertise and application knowledge. The spectral noise, $\Sigma$, can then be defined in the "inverse" (or "statistical" or "P-matrix") way, i.e., by collecting a population of characteristic spectra, but *without* the need for lab-reference values. The b-vector solution of the proposed method is optimal in a mean-square prediction error sense, and can be directly computed from **g** and $\Sigma$ by using Eq.(6).

With **g** defined by *a-priori* knowledge, spectroscopy is no longer a "secondary" method that needs calibration against a "primary" reference method. Instead, it becomes a "primary" method, firmly routed on physics and chemistry. Significant practical benefits can be reaped from this change. Whereas "classical" calibration could not realize these benefits in many applications for the reason discussed in [1,2], the proposed method *can* make these benefits available to a majority of spectroscopic applications, including NIR applications. Whenever a responsible application scientist is able to define the shape of the response spectrum "manually," the following benefits apply:

- The need for lab-reference values is virtually eliminated from calibration because the calibration does no longer need to "learn" what the signal *a.k.a.* g-vector is. The cost of calibration can therefore be

significantly reduced compared to today's standard practice of statistical calibration based on PLS or PCR.

- Specificity of response can be proven to regulatory agencies and concerned end-users. (In fact, taking "manual" control over what is used as signal is the *only* way to guarantee specificity of response.)
- There is no need anymore to artificially upset an industrial process in order to collect on-line calibration standards that vary over a certain "range." Rather, a smoothly running process with a minimum of analyte variation is sufficient for measuring the "noise spectra" required for the new method. (If some unknown amount of variation is present, it doesn't hurt [2].)
- New possibilities become available to tackle calibration transfer.
- Spectrometer hardware performance can be directly translated into user-relevant output accuracy, cmp. Eq.(8), which greatly simplifies the setting of hardware specifications. This, in turn, often enables *significant reductions in R&D time and expense* required for the development of new, application-specific instruments.
- The calibration process itself becomes more transparent and "communicate-able," or in the words of the pharmaceutical industry, "science-based," which should create a multitude of opportunities for adapting calibrations to given measurement situations.

The process of "manually" defining the response vector, **g**, is not as daunting as many spectroscopists, and in particular, NIR spectroscopists, may think at first glance. Even in the NIR, it is estimated that the method is applicable in a majority of applications [2]. As demonstrated in the *Shout-out 2002* example, the method is also applicable in cases where the sample is optically scattering.

## REFERENCES


1. R. Marbach, On Wiener Filtering and the Physics Behind Statistical Modeling, J. Biomed. Optics 7, 130-147 (2002)
2. R. Marbach, New Method for Multivariate Calibration, submitted to Journal of Near Infrared Spectroscopy
3. Data can be downloaded from http://www.idrc-chambersburg.org/shootout_2002.htm; data provided courtesy of Purdue Pharma L.P. and Gary Ritchie.
4. D.W. Hopkins, Shout-out 2002: transfer of calibration for content of active in a pharmaceutical tablet, NIR News 14 (5), 10 - 13 (2003)
5. G.E. Ritchie; R.W. Roller; E.W. Ciurczak; H. Mark; C. Tso; S.A. MacDonald, Validation of a near-infrared transmission spectroscopic procedure - Part B: Application to alternate content uniformity and release assay methods for pharmaceutical solid dosage form, J. Pharm. Biomed. Anal. 29, 159-171 (2002)


Ralf Marbach
*Ralf.Marbach@vtt.fi*

# Accurate Colour Inspection System for Real Time Industrial Application

## INTRODUCTION

Colour gives the finishing touch for many products. In furniture, for example, parquet and coating steel production colour is a very important feature of the final product. Nowadays it is common to measure colour point-by-point. A major drawback with this is that the result is based on a more or less random set of samples and colour variation may pass undetected.

The main objective of this R&D project is to combine two different colour measurement techniques into a single method capable of measuring colour very quickly and accurately in wide areas. The method is targeted at online applications and the results can be reported in various formats including CIELAB values. The colour inspection system is based on a compact prism-grating-prism imaging spectrograph, PGP camera, and three channel colour technique, RGB camera. Due to the optical features of the spectrograph, it is possible to accurately measure the colour of a surface of a product completely during the manufacturing process. On the other hand, this three channel technique can be used for fast colour measuring, but the colour information acquired is less accurate than with full spectrum data. The performance of the method was evaluated and demonstrated under laboratory and industrial conditions. The results enable the participants to develop commercial colour measurement devices.

## PROJECT RESULTS

The objective of the project was to implement a colour inspection system in real time industrial applications. The system was composed of a PGP camera, an RGB camera, a user interface and an analysis program. The PGP camera is very accurate but its measurement rate is low, whereas the RGB camera provides continuous data at a high rate. In order to generate accurate colour data, high accuracy PGP data is combined with high-speed RGB data. The imaging and illumination part of the measurement is depicted in Figure 1.

The application platform was a dual processor PC running MS Windows 2000. The user-interface is shown in Figure 2a). Before measuring the colour, the inspection system is calibrated using a known target. The measurement area was up to 1000 mm in cross direction and the wavelength range was from 400 nm to 700 nm. The spectrographs optical resolution was 5 nm, which enables precise colour measurement. The colour values were calculated in relation to D65 illumination. Measurement results were reported in XYZ tristimulus values, CIELAB values and colour difference between two values. The XYZ tristimulus values are calculated from CIE standard observer functions, taking into account the type of illumination and reflectance of the sample. XYZ tristimulus values are often converted to L, a, b scale using equations. 'L' is for lightness, 'a' is for redness-greenness, and 'b' is for yellowish-bluish. Figure 2 b) shows Lab-values as a function of the position measured by the system. The repeatability of colour for white reference was $\Delta E=0.1$ for the PGP camera and $\Delta E=0.3$ for the RGB camera. An accurate colour inspection system was demonstrated on the production lines of the end user participants.

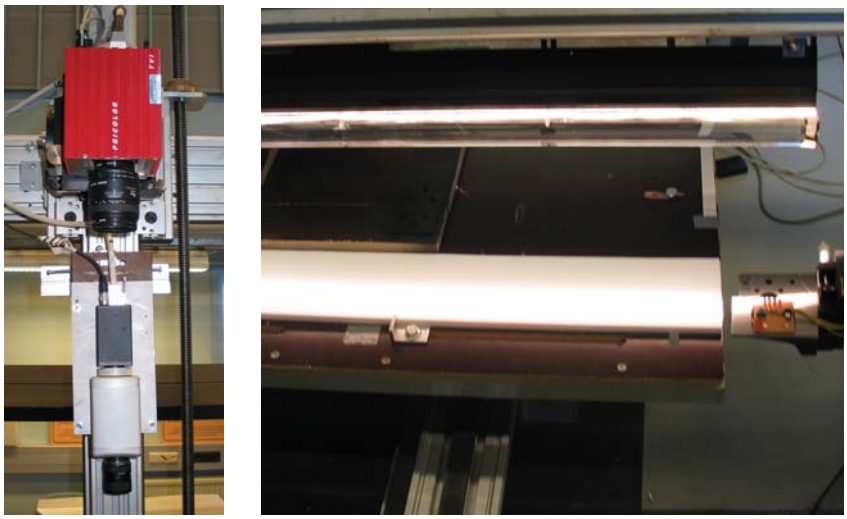

*Figure 1. The imaging and illumination part of the measurement.*

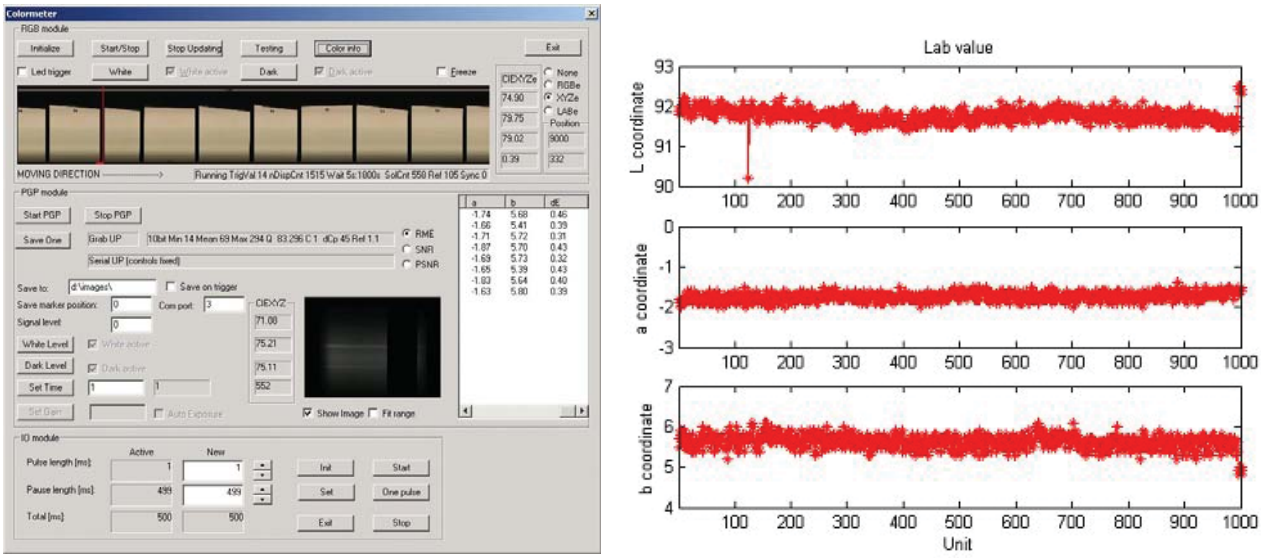


*a)* *b)*

*Figure 2. a) User interface, and b) Lab values measured by the colour inspection system.*

## CONCLUSIONS

In summary, an accurate colour inspection system has been developed for real time industrial applications. The benefits include a tested method combining speed, accuracy and total coverage. The project results give the project participants a chance to develop the colour inspection system.

Jari Miettinen
*Jari.Miettinen@vtt.fi*

Tapio Vaarala
*Tapio.Vaarala@vtt.fi*

# 3-D Measurement System for Steel Tube Production

## INTRODUCTION

VTT Electronics has developed real-time process 3-D measurement system, PROFMIT, for dimension measurement of steel products. Measurement device enables automation of steel tube and beam production. The system replaces current manual dimension measurement method. Dimension measurement device has been integrated to the production's control system and it reduces the amount of waste in production. Measurement system is based on the 3-D measurement method, in which semiconductor lasers, advanced machine vision and dedicated 3-D calibration algorithms are applied.

## INSTRUMENTATION

VTT and Ruukki have developed a new advanced 3-D measurement device tailored to Ruukki's steel production line. The development project was done in two phases. In the first phase VTT designed, realised and demonstrated the performance of the off-line measurement device. Based on the experience from this prototype instrument, the real-time production-integrated measurement system was developed in phase two. In the near future Ruukki is going to integrate this in-line dimension measurement system with their production's control system, developed by CapriCode Oy, in order to maximise speed and quality in production.

The developed 3-D measuring system is based on the optical triangulation measurement principle and employs line lasers for illuminating the target and matrix cameras. The dimension measurement is realised with a multi-camera machine vision system and accurate detection of the laser line position. The challenge in this measuring system was to construct well-stabilized high-precision optomechanics and intelligent calibration for a very demanding process application. The reflection properties of the surface of the steel tubes and pipes vary a lot and the system must be able to measure the dimensions reliably.


*Figure 1. Measuring Principle.*

## RESULTS

The need for a fast and reliable measurement tool mainly comes from the large product range offered by Ruukki. The short delivery times, small stocks and focus on demanding high-tolerance products has led Ruukki to renovate their production and develop state-of-the-art measuring and automation systems for their production lines. The developed measurement system will replace the manual measurement method in production, and the system offers fast feedback on tube dimensions for the automated control system. The 3-D dimension measurement will dramatically reduce the amount of waste because the adjustments to production can be done immediately based on reliable measuring data. The obvious benefit of the measuring system is the faster and easier product changing operation, which is essential in cost-effective production of Ruukki's tubular steel products.

## SUMMARY

VTT has developed a real-time dimension measuring system integrated with Ruukki's hollow section and tube production. Based on the measuring data, Ruukki has developed a state-of-the-art measuring and automation system for their control purposes. The measuring system enables continuous control and adjustment of the machine rolls and enables cost-effective, high-quality production for demanding tubular steel applications.


*Figure 2. PROFMIT-measuring system has been installed into steel production line.*

Jukka Eilola, Sakari Impola *Ruukki*

Tapio Vaarala
*Tapio.Vaarala@vtt.fi*

Janne Paaso
*Janne.Paaso@vtt.fi*

Jari Miettinen
*Jari.Miettinen@vtt.fi*

Janne Suhonen
*Janne.Suhonen@vtt.fi*

# Tunable Laser Module for Fibre Optic Communications

This thesis deals with the design, realisation, and testing of the wavelength tunable 1540-nm laser modules that are intended for fibre optic communications. The short external cavity laser uses an electrically controlled silicon micromachined Fabry-Perot interferometer (FPI) device as the tuning element.

First, the most common techniques for the diode laser wavelength tuning and applications for these devices are reviewed. Then the ways of coupling laser power into the single-mode (SM) optical fibre are considered and the characteristics of the fibre attachment methods are studied.

The design, assembly and testing of three prototypes is introduced. Their discontinuous tuning spans range between 8 and 13 nm and their output power between 100 and 570 µW. The modules produce multimode tuning having an rms spectral width of about 1 nm. In addition, one prototype is capable of single-mode tuning with a side mode suppression ratio of 26 dB. The measured wavelength span is threefold compared to our earlier work near 980 nm and the widest reported single-mode tuning range obtained from a short external cavity Fabry-Perot diode laser without temperature tuning. This is also the first directly modulated external cavity laser that has a 3dB bandwidth of over 600 MHz.

The study confirms that it is possible to realise the laser-to-SM-fibre coupling using adhesive bonding. Further studies are needed in order to improve the speed and repeatability of the assembly process together with the long-term reliability of the fibre attachment.

The prototype test results show that the FPI-tuned diode lasers have potential for applications where moderate performance suffices and low cost is mandatory. The hybrid arrangement uses standard laser components and therefore can provide a cost-effective and easily configurable solution for fibre optic communication and sensor applications. However, before the device characteristics can be optimised the theoretical understanding of the FPI-tuned laser operation must be enhanced. In addition, the packaging techniques of the modules need to be improved taking into account both the reliability requirements and the cost of production.

Doctoral Thesis, University of Oulu, Department of Electrical and Information Engineering. 2004.

Veli Heikkinen
*Veli.Heikkinen@vtt.fi*

# Extremely Short External Cavity (ESEC) Laser Devices. Wavelength Tuning and Related Optical Characteristics

In this work, we have developed ways to model and use extremely short external cavity (ESEC) semiconductor lasers. We have used modeling and experiments to analyze the wavelength tuning and other related optical characteristics of various ESEC laser devices. A brief overview is given on the physics related to semiconductor lasers. A simple phenomenological laser model is presented for the efficient calculation of the multi-mode output spectrum of a Fabry–Perot semiconductor laser. The effective reflectance model is used to simulate the influence of the ESEC on the laser operation. Several ways to calculate the effective reflectance from various kinds of ESEC structures are presented, including the Gaussian beam method, Fourier optics methods, and finite-difference time-domain (FDTD) method. We give an overview of the ESEC laser devices. The wavelength tuning and optical power characteristics of the planar-mirror (PM) ESEC laser are analyzed and compared to the measurements. The wavelength tuning of a laser using a micromachined tunable Fabry–Perot etalon in the ESEC configuration is analyzed. A method of wavelength tuning profilometry in the ESEC laser configuration is introduced, and the proof-of-principle experiments are presented and analyzed. The direct semiconductor laser readout systems for optical data storage are analyzed via modeling. Various types of playback signals are constructed, and a wavelength tuning enhanced readout method is introduced. The performance of a conventional Fabry–Perot laser and a very small aperture laser (VSAL) in the direct semiconductor laser readout system are modeled and compared using the novel FDTD laser-end model.

Doctoral Thesis, University of Oulu, Department of Physical Sciences. 2004.

Janne Aikio
*Janne.Aikio@vtt.fi*

# VCSEL Array Based Transmitter for Optical Interconnects

In this study, integration of high-speed optical interconnects into printed wiring boards is investigated. The performance of electrical interconnects has many physical limitations, for instance, due to dispersion, electromagnetic emission, and susceptibility against electromagnetic radiation. In contrast, optical interconnects offer very high bandwidth and are insensitive to EMI/EMC problems. Hybrid optical-electrical board including both electrical wiring and polymer waveguides, is an attractive concept, since it is a cost-effective solution if used processes are compatible with current mass production methods. In this work, transmitters using three different optical coupling schemes were designed, fabricated and tested. One of the coupling schemes was butt-coupling, and the others were based on microlens arrays and micro ball lenses. Optical front-end of the transmitter was located on LTCC substrate, which included VCSEL array and drivers and associated passive components for it, as well as micro-optical components. By the use of the transmitter, alignment tolerances and optical coupling efficiencies into polymer waveguides were characterized. Also characterized was the high-speed performance of the transmitter and signal propagation through a waveguide. Results indicate that alignment tolerances are challenging but probably achievable with modern surface-mounting assembly techniques. Coupling efficiencies can be improved by modifications in the design and by better and more integrated optical components. Due to deficient characterization equipment made it difficult to properly characterize high-speed performance of the VCSEL and driving circuitry, but fairly good operation was demonstrated. Better results can probably be obtained by the use of state-of-the-art integrated drivers, designed to control VCSEL arrays. Such devices were not yet available when components for the transmitter were chosen.

Diploma Thesis, University of Oulu, Department of Electrical and Information Engineering. 2004.

Teemu Alajoki
*Teemu.Alajoki@vtt.fi*

# Optical Biosensors

Optical integrated biosensors are an interesting alternative to conventional laboratory equipments in all areas concerned with biomolecule analyses. These biosensors are miniature optical configurations with a potential to be quick and simple to use, and in addition cheaper to fabricate than current laboratory devices.

Optical integrated biosensors can be either direct or indirect sensors. Indirect sensors require a label, which attaches to the measured molecule and prevents the defects rising from non-specific binding. Although this improves the sensitivity of the sensor, indirect sensor needs a more complicated measuring process, because of several washing steps to remove bound from unbound label. Thus the most straightforward way is to use the direct biosensor. There are several ways to realise a direct biosensor and one of the simplest ones is a Young interferometer.

We have modelled an integrated optical Young interferometer according to electromagnetic theory of propagation of light in waveguides and far fields. The designed interferometer structure should possess single mode behaviour and a sensitivity of a magnitude of $10^{-5}$. The structure is based on a 3.7µm wide and a 2.8µm thick channel waveguide with following refractive indexes $n_f$=1.49547, $n_c$=1.49233 and $n_s$=1.49233. The Young interferometer has a 60µm branch separation and 5mm long sensing and reference windows.

According to experiments the measured and the modelled transitions of the interference pattern were in the same order of magnitude. The theoretical sensitivity obtained for the interferometer structure was $9 \cdot 10^{-5}$ . Although the interferometer functioned as expected, the sensitivity analysis was affected by the measuring configurations in such extend that neither the real sensitivity nor the comparability of the theoretical model was possible to obtain with sufficient accuracy.

Master's Thesis, University of Oulu, Physics Department of Biophysics.

Sanna Ollitervo
*Sanna.Ollitervo@vtt.fi*

# Thermal Management and Thermomechanical Reliability of LTCC Package for 24 GHz band

This master's thesis studies thermal management and thermomechanical reliability of radar sensor demonstrator package for the 24 GHz band. The package consists of a RFIC flip chip bonded on a LTCC module attached to a printed circuit board. The work includes fabricating test structures and performing measurements and tests on them. Flotherm simulation software is used to assist in improving thermal management and thermomechanical reliability. The usability of the software in this kind of study is also evaluated.

Temperature measurements on test structures revealed that vias right under the flip chip bumps cool the chip most efficiently. The version in which signals and grounds were first distributed to the edge areas of the module and then connected through the LTCC layers with vias had higher chip temperature in both simulations and measurements. Underfill applied under the RFIC chip was also found to enhance the thermal management of the package.

Thermomechanical reliability tests revealed that to ensure reliability of demonstrator package the LTCC module should be as small as possible. The fatigue life predictions made with Flostress software were substantially longer than real test results because fatigue damage was not due to crack in a solder joint as the simulator assumed. Instead the damage was located on printed circuit board. The discovery demonstrated that joints are not the most susceptible to thermally induced stresses and strains after all, an assumption which was taken for granted in whole study.

Flotherm was concluded to be a useful tool for thermal management since it gave reasonable results and managed to imitate the thermal behaviour of the structure. In contrast thermomechanic simulations made with Flostress module gave over optimistic results. However when attributes were changed to investigate the effect of package dimensions and simulation circumstances, simulations followed real situation quite well. Thus it was concluded that even though Flostress was unable to predict fatigue life accurately it can be used for comparing different designs from thermomechanical reliability point of view.

Master's Thesis, University of Oulu, Department of Electrical and Information Engineering. 2004

Eveliina Juntunen
*Eveliina.Juntunen@vtt.fi*

# Device Management System of the Micro Module Center

This Bachelor's thesis involved the introduction of the device management system for the process devices of VTT Electronics' Micromodule Center process devices.

The system was implemented using the FacilityInfo maintenance manual software operated over an Internet browser. A device database, based on the process device locations and groups, was constructed into the software. The basic data of the device, such as name, type, serial number, manufacturer, device supplier, technical data and possible additional information of the device, was entered into the device database. Advance maintenance programmes were also created for part of the devices.

The device management system will be used for maintaining process device data, device maintenance, timing of regular maintenance and collecting maintenance history data.

Engineer's thesis, Oulu Polytechnic, Degree Programme in Information Technology and Telecommunications, Option of Measurement and Testing Systems, 2004.

Sami Karjalainen
*Sami.K.Karjalainen@vtt.fi*

# List of refereed papers

Extremely short external cavity (ESEC) laser devices. Wavelength tuning and related optical characteristics, Aikio, Janne K, 2004. VTT Electronics, Espoo. 162 p.,VTT Publications : 529, ISBN 951-38-6377-8; 951-38-6378-6

Characterization of an experimental ferrite LTCC tape system for microwave and millimeter-wave applications, Bray, J.; Kautio, Kari; Roy, L., IEEE Transactions on Advanced Packaging . IEEE. US. Vol. 27 (2004, No: 3, 558 – 565.

Non-Contact Critical Dimension Metrology Sensor for Chrome Photomasks Featuring a Low Temperature Co-Fired Ceramic Technology. N. Guillaume, R. Allen, M. Cresswell, M. Lahti, L. Linholm, M. Zaghloul. IEEE Transactions on Semiconductor Manufacturing, Vol. 17, Issue 1, 2004, pp. 25-34.

Tunable laser module for fibre optic communications, Heikkinen, Veli, 2004. VTT Electronics, Espoo. 171 p. + app. 11 p., VTT Publications : 528, ISBN 951-38-6375-1; 951-38-6376-X.

Single-mode tuning of a 1540-nm diode laser using a Fabry–Pérot I nterferometer, Heikkinen, Veli; Aikio, Janne; Alajoki, Teemu; Hiltunen, Jussi; Mattila, Antti-Jussi; Ollila, Jyrki; Karioja, Pentti, IEEE Photonics Technology Letters . Vol. 16 (2004) No: 4, 1164 – 1166.

600 MHz direct modulation of short external cavity wavelength-tunable diode laser, http://ieeexplore.ieee.org/servlets/opac?punumber=2220&isvol=40&isno=14, Heikkinen, Veli; Ollila, Jyrki; Rantanen, Timo; Vanhatalo, Karri; Karioja, Pentti, Electronics letters. Vol. 40 (2004) No: 14 , 871 – 872.

Photoinduced Ultrafast Dynamics of Ru(dcbpy)2(NCS)2-Sensitized Nanocrystalline TiO2 Films: The Influence of Sample Preparation and Experimental Conditions doi: 10.1021/jp037265v, Kallioinen, Jani; Benkö, Gabor; Myllyperkiö, Pasi; Khriachtchev, Leonid; Skårman, Björn; Wallenberg, Reine; Tuomikoski, Markus; Korppi-Tommola, Jouko; Sundström, Villy; Yartsev, Arkady P., Journal of physical chemistry B . Vol. 108 (2004) No: 20, 6365 – 6373.

Numerical study of the AgOx super resolution structure, http://jjap.ipap.jp/link?JJAP/43/160/, Kataja, Kari; Olkkonen, Juuso; Aikio, Janne; Howe, Dennis, Japanese Journal of Applied Physics, Part 1 (Regular Papers, Short Notes & Review Papers) . Vol. 43 (2004) No: 1, 160 – 167.

Readout modeling of super resolution disks, Kataja, Kari; Olkkonen, Juuso; Aikio, Janne; Howe, Dennis G., Japanese Journal of Applied Physics. Vol. 43 (2004) No: 7B , 4718 – 4723.

Synthesis and characterization of optical sol–gel adhesive for military protective polycarbonate resin, Kerä–nen, Mikko; Gnyba, Marcin; Raerinne, Paavo; Kololuoma, Terho; Maaninen, Arto; Rantala, Juha, Journal of Sol-Gel Science and Technology . Vol. 31 (2004), 369 – 372.

Multiplexed read out electronics implemented on LTCC substrate for PbS array, http://stacks.iop.org/0957-0233/15/2188, Moilanen, Ville; Kemppainen, Antti; Malinen, Jouko; Känsäkoski, Markku; Marbach, Ralf, Measurement Science and Technology. Vol. 15 ( 2004) No: 11, 2188 - 2192.

Process cure monitoring of unsaturated polyester resins, vinyl ester resins, and gel coats by Raman spectroscopy, doi: 10.1002/app.20584, Skrifvars, Mikael; Niemelä, Pentti; Koskinen, Rauli; Hormi, Osmo, Journal of Applied Polymer Science. Vol. 93 (2004) No: 3, 1285 - 1292.

# International Conference Papers

Design for photonics modules - combining optical geometrical and assembly process tolerance simulation in concept creation. Heilala, Juhani; Väätäinen, Otso; Keränen, Kimmo; Mäkinen, Jukka-Tapani; Kautio, Kari; Ollila, Jyrki; Petäjä, Jarno; Karppinen, Mikko; Heikkinen, Veli; Karioja, Pentti. IPAS 2004 International Precision Assembly Seminar, Bad Hofgastein, 11-13 Febr. 2004 (2004), 199 - 204

Optical interconnect on printed wiring board doi: 10.1117/12.530350. Karppinen, Mikko; Mäkinen, Jukka-Tapani; Kataja, Kari; Tanskanen, Antti; Alajoki, Teemu; Karioja, Pentti; Immonen, Marika; Kivilahti, Jorma. Proceedings of SPIE - The International Society for Optical Engineering. Photonics Packaging and Integration IV. San Jose, CA, US, 29 Jan. 2004. Vol. 5358. SPIE (2004), 135 - 145

Readout signal simulation as a function of readout power for super resolution optical disk. Kataja, Kari; Nakano, Takashi; Aikio, Janne; Tominaga, Junji. Proceedings of SPIE. ODS04, Optical Data Storage 2004. Monterey, 18 - 21 Apr. 2004 . SPIE. US (2004), 663 - 670

Precision alignment and cooling structures for photonic packaging on LTCC. Kautio, Kari; Keränen, Kimmo; Ollila, Jyrki; Mäkinen, Jukka-Tapani; Hiltunen, Jussi; Karioja, Pentti. Proceedings of 2004 IMAPS Conference on Ceramic Interconnect Technology. Denver, 26 -28 Apr. 2004 (2004), 71 - 76.

Cost-effective packaging of laser modules using LTCC substrates doi: 10.1117/12.528280. Keränen, Kimmo; Mäkinen, Jukka-Tapani; Heilala, Juhani; Väätäinen, Otso; Kautio, Kari; Ollila, Jyrki; Petäjä, Jarno; Karppinen, Mikko; Heikkinen, Veli; Karioja, Pentti. Proceedings of SPIE - The International Society for Optical Engineering. Photonics Packaging and Integration IV. San Jose, CA, US, 29 Jan. 2004. Vol. 5358. SPIE (2004), 111 – 121

Simulation of imaging system's performance. Kolehmainen, Timo T.; Aikio, Janne; Karppinen, Mikko; Mattila, Antti-Jussi; Mäkinen, Jukka-Tapani; Kataja, Kari; Tukkiniemi, Kari; Karioja, Pentti. Optical Science and Technology. San Diego, 3 - 8 Aug. 2003 2004. SPIE , Bellingham ; US Proceedings of SPIE : 5178

Directly UV-photopatternable PLZT thin films prepared with the Sol-Gel technique. Kololuoma, Terho; Hiltunen, Jussi; Tuomikoski, Markus; Lappalainen, Jyrki; Rantala, Juha. Proceedings of SPIE, 5355, Integrated Optics Devices, Materials, and Technologies VIII, Editor: Yakov Sidorin, Ari Tervonen, (2004), 33 - 39.

Towards roll-to-roll fabrication of electronics, optics and optoelectronics for smart and intelligent packaging. Kololuoma, Terho; Tuomikoski, Markus; Mäkelä, Tapio; Heilmann, Jali; Haring, Tomi; Kallioinen, Jani; Hagberg, Juha; Kettunen, Ilkka; Kopola, Harri. Proceedings of SPIE, 5363 Emerging Optoelectronic Applications, Editor: G. E. Jabbour and J. T. Rantala, (2004), 77 - 85. (Invited).

LTCC Band-Pass Filter for Transmitter / Receiver Modules. V. Kondratyev, M. Lahti, T. Jaakola. European Microwave Conference, October 11-15, 2004, Amsterdam, The Netherlands, pp. 401-404.

Technologies for hybrid integration of photonic and electronic micromodules. Kopola, Harri; Aikio, Janne; Aikio, Mauri; Karppinen, Mikko; Jaakola, Tuomo; Kololuoma, Terho. DVS/GMM Tagung, Aufbau und Fertigungstechnik, Fellbach, Germany. DE, 2004 (2004)

Photo-crosslinkable hybrid material with improved ageing stability for integrated optics. Kusevic, Maja; Maaninen, Arto; Hiltunen, Jussi; Hiltunen, Marianne; Tuominen, Jarkko; Karioja, Pentti. 2004. SPIE, US Proceedings of the SPIE : 5451, 487 - 494.

Integrated multichannel detector analysers at process control. Känsäkoski, Markku; Kemppainen, Antti; Suhonen, Janne; Malinen, Jouko; Rantanen, Jukka; Yliruusi, Jouko; Luostarinen, Kari; Nauha, Pentti. Near Infrared Spectroscopy. Proceedings of the 11th International Conference NIR 2003 Near Infrared Spectroscopy ; Proceedings of the 11th International Conference. Eds. Davies, A.M.C ; Garrido-Varo, A.. NIR Publications. UK (2004), 121 - 126, 1119

Monitoring the internal quality of potatoes by NIR transmission and reflection measurement. Känsäkoski, Markku, T.; Suopajärvi, Pekka; Heikkinen, Veli; Mitikka, Risto; Chalucova, Raina, P.; Krivoshiev, Georgi, P.; Vasama, Hannu. Near Infrared Spectroscopy. Proceedings of the 11th International Conference NIR 2003. Near Infrared Spectroscopy ; Proceedings of the 11th International Conference. Eds. Davies, A.M.C ; Garrido-Varo, A.. NIR Publications. UK (2004) , 127 - 132, 1119

Qualitative and quantitative determination of illicit drugs using raman spectroscopy. Laakkonen, Ulla-Maija; Sippola, Erkki; Katainen, Erja; Järvinen, Kristiina; Niemelä, Pentti; Suhonen, Janne. 10th ENFSI Drugs Working Group meeting, Riva del Garda, 30 - 31 May 2004 (2004), 13 p.

Integration of high-power devices into LTCC modules or packages Lahti, Markku; Kautio, Kari. 1st Annual Technical Conference. Edinburgh, 20 - 21 May 2004. GB (2004)

Prospects and limits of LTCC technology. Lenkkeri, Jaakko; Jaakola, Tuomo; Kautio, Kari; Lahti, Markku; Collander, Paul. IMAPS Nordic Annual Conference. Helsingör, 26 - 28 Sep. 2004 (2004), 108 - 114.

LTCC-teknologian haasteet ja mahdollisuudet. J. Lenkkeri, T. Jaakola, K. Kautio, M. Lahti. Proc. of Electronics Production and Packaging Technology Conference, 13-14.5.2004, Pori, Finland, pp. 225-230.

Performance evaluation of standard and extended InGaAs detector array spectrometers. Lindström, Hannu; Malinen, Jouko; Marbach, Ralf. Near Infrared Spectroscopy. Proceedings of the 11th International Conference NIR2003. Near Infrared Spectroscopy ; Proceedings of the 11th International Conference. Eds. Davies, A.M.C. ; Garrido-Varo, A.. NIR Publications. UK (2004) , 99 - 104, 1119

Development of an optoelectronic sensor for measuring varnish thickness on-line. Manero, Francisco; Anduaga, Javier; Mayora, Kepa; Garmendia, Izaskun; Niemelä, Pentti; Hietala, Eero; Tornberg, 11th International Conference on Near-Infrared Spectroscopy. Cordoba, Spain, 6 - 11 April 2003. NIR-2003 ; stretching the NIR spectrum to the limit. 11th International Conference on Near-Infrared Spectroscopy. Cordoba,6 - 11 Apr. 2003 . NIR Publications. Norwich (2004), 1105 - 1109

Integrate-it-yourself preamp and multiplexer on LTCC substrate, for PbS array. Moilanen, Ville; Kemppainen, Antti; Känsäkoski, Markku; Malinen, Jouko; Marbach, Ralf, Near Infrared Spectroscopy. Proceedings of the 11th International Conference NIR 2003. Near Infrared Spectroscopy ; Proceedings of the 11th International Conference. Eds. Davies, A.M.C ; Garrido-Varo, A. . NIR Publications. UK (2004), 139 - 141, 1119

Prototyping of miniature plastic imaging lens. Mäkinen, Jukka-Tapani; Aikio, Janne; Putila, Veli-Pekka; Keränen, Kimmo; Karioja, Pentti; Kolehmainen, Timo T.; Haavisto, Janne, Optical Science and Technology. San Diego, 3 - 8 Aug. 2003. 2004. SPIE, Bellingham ; US Proceedngs of SPIE : 5178 ISBN 0-8194-5051-0, 89 - 100.

Determnation of amorphous content of lactose using raman spectroscopy. Niemelä, Pentti; Päällysaho, Maarit;Harjunen, Päivi; Koivisto, Mikko; Lehto, Vesa-Pekka; Suhonen, Janne; Järvinen, Kristiina, 15th International Symposium on Pharmaceutical and Biomedical Analysis. Florence, 2 - 6 May 2004 (2004), 340

Imaging lens design using image quality metric. Olivès, Jean-Luc; Kolehmainen, Timo T.; Aikio, Janne; Kataja, Kari J.; Karioja, Pentti; Vuori, Tero; Mustonen, T. Optical Systems Design SPIE's International Symposium, St. Etienne, France, 30 Sept. - 3 Oct. 2003. Optical design and engineering, Mazuray, Laurent; Rogers, Philip J.; Wartmann, Rolf (Eds.), Proceedings of SPIE, vol. 5249 . SPIE. Bellingham (2004) , 616 - 623

On surface plasmon enhanced near-field transducers. Olkkonen, Juuso, T.; Kataja, Kari, J.; Aikio, Janne; Howe, Dennis G. Proc. SPIE Vol. 5380, p. 360 - 367, Optical Data Storage 2004; B. V. K. Vijaya Kumar, Hiromichi Kobori; Eds. Publication. 2004.

Analysis of sub-wavelength apertures via the extended FDTD SF technique. Olkkonen, Juuso T.; Kataja, Kari J.; Aikio, Janne; Howe, Dennis G.; Milster, Tom D. Proc. SPIE Vol. 5380, p. 653 - 662, Optical Data Storage 2004; B. V. K. Vijaya Kumar, Hiromichi Kobori; Eds. Publication. 2004.

Multi-Layer stubs in LTCC technology. Panther, A.; Stubbs, M.G.; Kautio, Kari, 2004 European Microwave Conference Digest. Amsterdam, 11 - 15 Oct. 2004 (2004), 617 - 620

Compact, low-cost 24 GHz modules using micromachined Si/SiGe HBT technology. Schumacher, Hermann; Abele, Peter; Berntgen, Jürgen; Grenier, Katia; Lenkkeri, Jaakko; Lindberg, Peter; Öjefors, Erik; Plana, Robert; Rabe, Winfried-Johann; Rydberg, Anders; Sönmez, Ertugrul; Wallin, Kjell. IST Mobile and Wireless Communications Summit. Lyon, 27 - 30 Jun. 2004 . EU / IST (2004), 5 p

High performances of shielded LTCC vertical transitions from DC up to 50 GHz. Valois, R.; Baillargeat, D.; Verdeyme, S.; Lahti, Markku; Jaakola, Tuomo. European Microwave Conference. Amsterdam, Oct. 2004 (2004), 537 - 540

# Other Publications

High-resolution imaging optics needing no assembly-phase optial adjustements. http://herkules.oulu.fi/isbn9514272870/isbn9514272870.pdf. Aikio, Janne; Edström, C; Suopajärvi, Pekka; Vasama, H.; Seppänen, Tomi; Tannemyr, M.; Aikio, Mauri. Proceedings of the XXXVIII Annual conference of the Finnish Physical Society (Report Series in Physical Sciences, University of Oulu, Report No. 25) Edited by R. Rasinkangas. University of Oulu. Oulu (2004), 296

Micro-optical system modelling using non-sequential ray tracing. Aikio, Sanna; Liang, C.; Mäkinen, Jukka-Tapani; Descour, M.R. BIO meets Nano and IT Technology Partnering Meeting and Scientific Seminar. Oulu, 1 - 3 Sep. 2004. Oulu ; FI (2004)

VCSEL array based transmittter for optical interconnects. Alajoki, Teemu. University of Oulu ; Department of Electrical and Information Engineering. FI (2004), 89 Opinnäyte: diplomityö

Compact wavelength-tunable laser modules. Heikkinen, Veli; Aikio, Janne; Alajoki, Teemu; Karioja, Pentti; Ollila, Jyrki; Rantanen, T.; Vanhatalo, K. Proceedings of Optics Days 2004, Turku, 6 - 7 May 2004. University of Turku. Turku (2004), 11

Thermal management and thermomechanical reliability of LTCC package for 24 GHz band. Juntunen, Eveliina. 2004. University of Oulu, Oulu ; FI. 87. University of Oulu ; Department of Electrical and Information Engineering ; Master's Thesis

Mikromoduulikeskuksen prosessilaitekannan liittäminen laitehallintajärjestelmään. Insinöörityö. Karjalainen, Sami. Oulun seudun ammattikorkeakoulu. Oulu ( 2004), 40. s. + liitt. 15 s.

Raman spectroscopy for determination of drug release from polymer film. Katainen, Erja; Niemelä, Pentti; Suhonen, Janne; Järvinen, Kristiina. Fysikaalisen farmasian XV vuosittainen symposium. Juhlasymposium, Helsinki, 21 - 22.1.2004. FI (2004), 35

Readout signal simulation of the 3rd generation super resolution optical disk. Kataja, Kari; Nakano, Takashi; Aikio, Janne; Tominaga, Junji. Optiikan Päivät. Turku, 6 - 7.5 2004. Suomen Optiikan Seura. FI (2004) , 30

FDTD simulations of super resolution optical data storage systems. http://herkules.oulu.fi/isbn9514272870/isbn9514272870.pdf. Kataja, Kari; Olkkonen, Juuso; Aikio, Janne; Howe, Dennis G. 2004. Oulu University Press, Oulu ; FI. Report Series in Physical Sciences ; University of Oulu, Report No. 25 : 25 ISBN 951-42-7129-7

Photonic modules based on 3D LTCC substrates. Keränen, Kimmo; Mäkinen, Jukka-Tapani; Kautio, Kari; Ollila, Jyrki; Heikkinen, Veli; Karioja, Pentti. Proceedings of Optics Days 2004, Turku, 6 - 7 May 2004. University of Turku. Turku (2004), 31

Biocompatible materials for disposable sensors. Kivimäki, Liisa; Höyhtyä, Matti; Känsäkoski, Markku; Maaninen, Arto. Optics Days - Optiikan päivät 2004, Turku, 6. - 7.5.2004 . Finnish Optical Society (FOS). Turku (2004) , 36

Biocompatible materials for disposable sensors. Kivimäki, Liisa; Höyhtyä, Matti; Känsäkoski, Markku; Maaninen, Arto; Kopola, Harri. BIO meets Nano and IT Technology Partnering Meeting and Scientific Seminar. Oulu, 1 - 3 Sep. 2004. Oulu ; FI (2004)

Synthesis and characterization of directly UV-photopatterned PLZT thin films. Kololuoma, Terho; Hiltunen, Jussi; Tuomikoski, Markus; Lappalainen, Jyrki; Rantala, Juha T. Proceedings of Optics Days 2004. Turku, 6 - 7 May 2004. . University of Turku. FI (2004), 37

Micro and nanotechnologies for photonic and electronic applications. Kopola, Harri; Kattelus, Hannu; Lammasniemi, Jorma. International Workshop on Micromechatronics and Micro and Nano Fabrication. Karlsruhe, 5 - 6 Oct. 2004. DE (2004), 10 p

Technologies for hybrid integration of biomicrosystems. Kopola, Harri; Känsäkoski, Markku; Maaninen, Arto; Kololuoma, Terho; Aikio, Sanna; Olkkonen, Juuso; Ollitervo, Sanna; Keränen, Kimmo; Heikkinen, Veli; Kivimäki, Liisa. BIO meets Nano and IT Technology Partnering Meeting and Scientific Seminar. Oulu, 1 - 3 Sep. 2004. Oulu ; FI (2004)

Advanced ceramic modules for RF- and microwave applications. Lahti, Markku; Kangasvieri, T.; Volotinen, J. RF and microwave micromodules. Part 4 Oulu, 3 - 4 Jun. 2004 (2004)

RF-piirejä LTCC-alustalle. Lahti, Markku; Kopola, Harri; Volotinen, J.; Kangasvieri, T.; Vähäkangas, Jouko. Prosessori. Elektroniikan suunnittelun erikoisnumero (2004) No: marraskuu, 66

Engineered antibodies suitable for property characterization by biosensors. Leinonen, Marika; Höyhtyä, Matti; Pirilä, Päivi; Hiltunen, Kalervo; Känsäkoski, Markku. BIO meets Nano and IT Technology Partnering Meeting and Scientific Seminar. Oulu, 1 - 3 Sep. 2004. Oulu ; FI (2004)

Elektroniikan tulevaisuuden haasteet. Lenkkeri, Jaakko. KOTEL-seminaari. Lyijytön liittäminen. Oulu, 20 Apr. 2004. FI (2004)

LTCC-teknologian haasteet ja mahdollisuudet. Lenkkeri, Jaakko; Jaakola, Tuomo; Kautio, Kari; Lahti, Markku. 2004. Tampereen teknillinen yliopisto ; Porin yksikkö ; Julkaisusarja A : A5/2004

Thermal simulation of lead-free wave soldering process. Lenkkeri, Jaakko; Lahti, Markku. Status in lead-free electronics assembly. Billingstad, 27 Jan. 2004. KOTEL-seminaari. Lyijytön liittäminen. Oulu, 20 Apr. 2004 (2004)

Towards low-cost biomicrosystems and disposable sensors. Maaninen, Arto; Känsäkoski, Markku; Kopola, Harri; Kololuoma, Terho; Aikio, Sanna; Olkkonen, Juuso; Ollitervo, Sanna; Kivimäki, Liisa. Plastic Electronics 2004, Eindhoven, 9 Sep. 2004 (2004)

Modelling of the local electric field of silver particles in surface-enhanced raman scattering by FDTD method. http://herkules.oulu.fi/isbn9514272870/isbn9514272870.pdf. Mattila, Antti-Jussi; Kataja, Kari J.; Alanko, Seppo; Känsäkoski, Markku; Niemelä, Pentti. Proceedings of the XXXVIII Annual conference of the Finnish Physical Society (Report Series in Physical Sciences, University of Oulu, Report No. 25) Edited by R. Rasinkangas. University of Oulu. Oulu (2004), 300

Surface plasmon enhanced light transmission through subwavelength apertures. Olkkonen, Juuso; Kataja, Kari; Aikio, Janne; Howe, Dennis G. Optics day 2004. Turku, 6 - 7 May 2004 . FI (2004), 47

Optical biosensors. Ollitervo, Sanna. University of Oulu ; department of physics ; biophysics. fi (2004), 69 + liitt. 6 Opinnäyte: pro gradu

Modeling of integrated waveguide young interferometer. Ollitervo, Sanna; Känsäkoski, Markku; Aikio, Janne; Alanko, Seppo; Hiltunen, Jussi; Kopola, Harri. BIO meets Nano and IT Technology Partnering Meeting and Scientific Seminar. Oulu, 1 - 3 Sep. 2004. Oulu ; FI (2004)

Gravure printing for the fabrication of organic light-emitting devices on flexible substrate. Tuomikoski, Markus; Jabbour, Ghassan E.; Kololuoma, Terho; Kopola, Harri. Proceedings of Optics Days 2004. Turku, 6 - 7 May 2004. . University of Turku. FI (2004), 67

# Patents

Menetelmä ja laitteisto paperin laatuominaisuuksien mittaamiseksi liikkuvasta paperiradasta paperikoneella. Hyvärinen, Timo; Känsäkoski, Markku; Mäntylä, Markku; Tenhunen, Jussi, Pat. FI 112975 B, julkaisupäivä 13.2.2004

Method and apparatus for measuring coating. Känsäkoski, Markku; Mäntylä, Markku; Tenhunen, Jussi. Pat. US 6717148 B2, publication date 6 April 2004,

A method and a measuring system for determining and monitoring exhaust gas emissions from a vehicle. Känsäkoski, Markku; Niemelä, Pentti. Pat. application number US2004/0104345 A1, application date 9 Oct. 2003, publication date 3 Jun. 2004 (2004), 18 p.

Menetelmä ja mittausjärjestelmä ajoneuvon pakokaasupäästöjen määrittämiseksi ja valvomiseksi. Känsäkoski, Markku; Niemelä, Pentti. Pat. FI 114572, julkaisupäivä 15.11.2004

Spectrometer. Malinen, Jouko. Pat hakemus. 97930542.2/ 17.7.1997. Pat. EP 1 019 685 B1/27 Oct. 2004 (2004)

**VTT TECHNICAL RESEARCH CENTRE OF FINLAND**
VTT ELECTRONICS
P.O.Box 1100, (Kaitoväylä 1)
FI-90571 OULU, FINLAND
Tel. + 358 20 722 111
Fax + 358 20 722 2320
e-mail: ele.info@vtt.fi
www.vtt.fi/ele